The Dissertation Committee for Kelin Chen Certifies that this is the approved version of the following Dissertation:

The Effect of Anisotropy on the Localization and Failure of Aluminum Alloys under Biaxial Loads

Committee:

Stelios Kyriakides, Supervisor

Edmundo Corona

Kenneth M. Liechti

Krishnaswamy Ravi-Chandar

Chad M. Landis

The Effect of Anisotropy on the Localization and Failure of Aluminum Alloys under Biaxial Loads

by

Kelin Chen

Dissertation

Presented to the Faculty of the Graduate School of

The University of Texas at Austin

in Partial Fulfillment

of the Requirements

for the Degree of

Doctor of Philosophy

The University of Texas at Austin

August 2019

Dedication

To my parents.

Acknowledgements

First I'd like to express my gratitude to my advisor Professor Stelios Kyriakides, whose academic and personal guidance has shaped who I am today. His keen physical insights and peerless expertise have impressed me through countless times of discussions we had. His research and teaching philosophies will always be invaluable to me throughout my career. His guidance and help on writing this dissertation are also acknowledged with thanks.

I'd like to thank the other members of my dissertation committee: Dr. Edmundo Corona, Professors Kenneth Liechti, Krishnaswamy Ravi-Chandar and Chad Landis for reviewing my dissertation and offering me constructive comments. I am grateful to every professor from whom I have taken a course. The coursework constituted a significant part of my study in UT as it not only improved my understanding of solid mechanics but also brought inspirations to my research in many ways.

Financial supports from Ford Motor Company, Sandia National Laboratories, National Science Foundation through the GOALI grant CMMI-1663269 and the Max L. Williams Endowed Graduate Fellowship in the Center for Mechanics of Solids, Structures, and Materials to my research are gratefully acknowledged with thanks.

It's been a pleasure to interact with so many brilliant fellow graduate students over the years (to list a few): Lin Yuan, Yafei Liu, Dongjie Jiang, Chenglin Yang, Karlos Kazinakis, Jake Haley, Solon Tsimpoukis and Weihan Zhang. Special thanks go to Nicolas Tardif for introducing me to the numerical analysis of my research and Martin Scales, an excellent experimentalist, with whom I had the pleasure to closely collaborate.

Last, I would like to express my deepest gratitude to my parents and grandparents. All my achievements wouldn't have been possible without their unconditional love and support.

Abstract

The Effect of Anisotropy on the Localization and Failure of Aluminum Alloys under Biaxial Loads

Kelin Chen, Ph.D.

The University of Texas at Austin, 2019

Supervisor: Stelios Kyriakides

Development of a robust finite element model capable of simulating ductile failure of thin-walled Al-alloy structures under complex loading conditions requires: (a) A suitably calibrated constitutive model of the material that includes the prevailing plastic anisotropy, and (b) an appropriately extracted material hardening response to large enough strains. This work addresses these two issues through the analysis of the response up to failure of thin sheets in hydraulic bulge tests, and the large deformation response of tubes under combined shear and tension.

Hydraulic bulge tests have been used to extract the material hardening response of sheet metals to large strains. The extraction requires proper knowledge of the plastic anisotropy in the sheets. To this end, the non-quadratic anisotropic yield function of Barlat et al. [2005] was calibrated using a series of uniaxial and biaxial tests and two data from the bulge test. The calibration uses an iterative scheme for evaluating the stress state at the apex. The calibrated yield function is then used to extract the material hardening. The veracity of the scheme is demonstrated by using the calibrated yield function and hardening response in a 3-D finite element model to successfully simulate the bulge test up to failure.

The second part of the project simulates the response of Al-alloy tubes under combined tension and torsion. Experiments conducted in parallel with this study have shown that following initial plastic deformation, strain localizes in a narrow zone and grows significantly before rupture. Here, the non-quadratic anisotropy yield function is calibrated using the set of tension-torsion experiments conducted, supplemented by a set of pressure-tension experiments. The constitutive model is then used to extract the material hardening response from a simple shear test accounting for the rotation of the material frame. The two constitutive components are then implemented in a 3-D finite element model to simulate a set of tension-torsion experiments. It is demonstrated that the constitutive model and hardening material response can reproduce the experimental structural responses, the onset of localization and its evolution to strains that correspond to the measured failure strains. This is achieved without the artificial introduction of material softening.

Table of Contents

Chapter 1: Introduction

1.1 MOTIVATION

With increasing demands for higher energy efficiency and reduced impact to the environment, the automotive industry is continuously developing new technologies and looking for alternate solutions. One of the strategies followed is reduction of the weight of automotive structures by using lighter materials such as Aluminum alloys (Cole and Sherman, 1995; Saito et al., 2001; Benedyk, 2010). During the last decade the use of Al-alloys in the automotive industry has been growing at an ever increasing rate as it offers significant reductions in weight with corresponding reductions in fuel consumption and obvious environmental benefits. Consequently, mechanical properties of Al-alloys, such as strength, stiffness and ductility, have been receiving increasing interest from the research community. Aluminum alloys generally have lower ductility and in sheet form can be more anisotropic than traditional steels.

During manufacturing processes, such as stamping and deep drawing Al-alloy sheets can suffer several different failure modes. Figure 1.1 shows a cup drawing experiment of Al-6016-T4 sheet in which the specimen develops a crack at the rim due to severe bending and tension. Figure 1.2 shows two failure modes experienced during hot stamping of Al6082 sheet. For a fast forming rate (0.64±0.01 m/s), failure initiates from the central hole along a meridian causing tearing. However, for a slow forming rate (0.166±0.01 m/s) the specimen develops circumferential tearing at mid-height. For even more extreme loading cases such as axial crushing of tubular specimens, experienced in energy absorption applications complex multi-lobe folding leads to fracture. Figure 1.3 shows an example of such failure suffered in an Al6063-T6 tube rail (See Kohar et al., 2017).

Thus, understanding the inelastic behavior and establishing the factors that govern ductile failure of these alloys is crucial to the development of alloys suitable for automotive applications. However, the complicated localized deformation that precedes failure and the underlying damage mechanisms have posed challenges to the experimental, numerical and theoretical investigation of Al alloys and further complicates the development of ductile failure criteria.

1.2 BACKGROUND

1.2.1 Effect of Triaxiality on Ductile Failure

The establishment of failure of a solid without initial visible cracks has a long history. The first generation of failure criteria for ductile metals involved extension of simple brittle failure criteria such as the maximum shear stress or constant equivalent strain criteria. These criteria did not account for the difference in the damage mechanisms between brittle and ductile materials and thus they were very limited.

Micromechanically based models such as cylindrical or spherical voids embedded in a matrix (McClintock, 1968; Rice and Tracey, 1969) have shown voids to grow exponentially with triaxiality. These pioneering works have pointed to the crucial role of triaxiality on ductile failure and the importance of incorporation of mircomechanisms in ductile failure analysis. Inspired by these works, a constitutive model that incorporates the effect of void volume fraction was proposed by Gurson [1977], which led to the fast-growing development of porous plasticity and continuum damage models. Enriched micromechanical models, which incorporate void nucleation, growth and coalescence, have been proposed (e.g., Chu and Needleman, 1980; Tvergaard and Needleman, 1984; Tvergaard, 1990; Benzerga and Lebond, 2010). Using unit cell analysis, issues such as void shape (Pardoen and Hutchinson, 2000), void interaction (Tvergaard, 1998), anisotropy of

matrix materials (Benzerga and Besson, 2001), decohesion from hard particles (Needleman, 1987), Lode angle (Gologanu et al., 2001; Barsoum and Faleskog, 2007b) have been intensively studied.

Continuum damage-based models without referring to the effect of voids explicitly have been developed to address brittle or ductile failure (Lemaitre, 1985; Lemaitre and Chaboche, 1990; Brunig et al., 2008). The important effect of triaxiality on ductile failure has also been highlighted from a different perspective.

Experimental investigations on the effect of hydrostatic pressure on the failure of a variety of alloys were also conducted date back to Bridgeman [1947, 1952] but also later works (e.g., Lewandowski and Lowhaphandu, 1998; Hancock and Mckenzie, 1976; Johnson and Cook, 1985). The failure criterion proposed by Johnson and Cook [1985] that features the exponential decay of failure strain with stress triaxiality has been widely adopted in simulation software packages (e.g., ABAQUS, ANSYS, LS-DYNA) for ductile failure predictions.

In summary, this body of theoretical, numerical and experimental works conducted during the past few decades, the notion that failure strain monotonically decreases with increasing triaxiality has been widely accepted.

1.2.2 Introduction of the Effect of Lode Angle to Ductile Failure

Inspired by the experimental results of Bao and Wierzbicki [2004] for Al 2024-T351, where the failure strain develops a local minimum near the pure shear state of stress, the effect of Lode angle (Lode, 1926) on ductile failure has come to the fore. Thus Lode angle dependent damage mechanisms were proposed to explain the low ductility in the shear-dominant regime (Xue, 2007; Nashon and Hutchinson, 2008); and were followed by a number of new phenomenological ductile failure criteria that involve both triaxiality and

Lode angle proposed to capture the experimental data. Lou and co-workers proposed several phenomenological criteria with increasing complexity and number of parameters to account for cut-off triaxiality value and Lode angle asymmetry (Lou et al., 2012, 2014, 2017). Bai and Wierzbicki [2010] extended the classical Mohr-Coulomb failure criterion for granular material to model ductile failure. Based on the onset of localization in a unit cell analysis, Mohr and Marcadet [2015] proposed an alternate failure criterion based on the Hosford yield function in combination with Coulomb failure concept. Additional failure criteria that involve invariants of stress tensor have also been proposed, such as the maximum stress vector criterion (Khan and Liu, 2012) and pressure-dependent Drucker yield function type failure criterion (Lou and Yoon, 2018). To incorporate the effect of anisotropy in sheet metals, anisotropic ductile failure criteria have also been proposed through linear transformation of stress or strain (Luo et al., 2012; Gu and Mohr, 2015; Lou and Yoon, 2017, 2019).

1.2.3 Recent Experimental Efforts on Ductile Failure

The experimental results of Bao and Wierzbicki [2004] prompted also new experimental investigations on several metal alloys using different test setups and specimen geometries. Beese et al. [2010] reported similar failure locus for Al-6061-T6 sheet through combined experimental and numerical analysis. Barsoum and Faleskog [2007a] conducted combined tension-torsion experiments on double notched tubular specimens of a mild-strength steel and a high strength steel, similar trends were found as those reported in Bao and Wierzbicki [2004]. However, in a more comprehensive experimental work of Faleskog and Barsoum [2013] where the range of triaxiality was extended to the range of 0 to 1.6, significantly high failure strains for low triaxialities were reported.

Mohr and co-workers designed butterfly flat specimens subjected to combined tension and shear loading (Mohr and Henn, 2007; Dunand and Mohr, 2011), notched tension of flat specimen (Dunand and Mohr, 2010, 2011), and notched thin-walled tubular specimens under tension-torsion (Papasidero et al., 2014, 2015) to investigate the ductile failure behavior of different types of Al alloys and steels. Hybrid experimental-numerical approaches were proposed to characterize material failure due to the complexity of stress and strain states in the test section. Other experimental results using similar specimens have also been reported (Brunig et al., 2008; Gao et al. 2009; Ghahremaninezhed and Ravi-Chandar, 2012, 2013; Graham et al., 2012; Lou and Yoon, 2017; Ha et al., 2018).

Scales et al. [2016] pointed out that the seemingly conflicting messages that come from experiments are mainly caused by practical limitations of testing materials, especially in sheet form, under combined shear and axial loads. Most experimental setups used are characterized by non-uniform stress and strain fields that can only be extracted by numerical modeling that often is tied to an assumed constitutive model. Furthermore, many specimen geometries used constrain the development of localization that precedes failure, which often is triggered from stress concentrations at the edges.

In an effort to add some clarity to the state of affairs, Kyriakides and co-workers used a custom designed test specimen and high resolution digital image correlation to establish the failure of Al-6061-T6 tubes under combined tension and torsion (Haltom et al., 2013; Scales et al., 2016, 2019). A test section is machined into a thicker tube that is mounted to a servo-hydraulic tension-torsion testing machine via well-aligned grips. The test section is wide and thin enough to permit a uniform plane stress state to develop to large deformations, and also allows the ensuing localization that precedes rupture to develop freely. The evolution of localization up to failure was captured using high-resolution 3D digital image correlation (DIC). The experiments covered triaxialities in the

range of 0 to 0.577 and provided reliable data with small uncertainties and limited reference to constitutive models.

In these experiments the failure strains were found to monotonically decrease with increasing triaxiality, in concert with the decades old conventional claim. Furthermore, the failure strains for Al-6061-T6 were significantly greater than previously reported values for this alloy, with strain levels exceeding 100% for low triaxialities. Moreover X-ray tomography and microscale observations showed that void nucleation and growth for the alloy tested is limited until the very end of failure. Similar observations have also been reported by Ghahremaninezhed and Ravi-Chandar [2012, 2013]. One of the aims of this thesis is to simulate these experiments numerically using suitable constitutive models and explore the extent to which the large localized deformations can be reproduced without the introduction of damage mechanisms.

1.2.4 Numerical Modeling of Ductile Failure

Development of a reliable numerical analysis requires an appropriate and robust constitutive model that is able to characterize the mechanical behavior of the material under different loading conditions. For conventional plasticity, the adoptions of the yield function and hardening law are essential to the performance of the constitutive model. Isotropic yield functions have been widely used in the numerical analysis of ductile failure due to their simplicity (e.g., von Mises: Bao and Wierzbicki, 2004; Barsoum and Faleskog, 2007a; Mohr and Henn, 2007; Papasidero et al., 2014. Hosford: Papasidero et al., 2015). However, a number of recent works have shown that anisotropy of Al-alloys due to the manufacturing process can have a significant influence on the constitutive behavior and structural response of Al alloy thin-walled components (e.g., Korkolis and Kyriakides, 2008, 2009; Giagmouris et al., 2010; Tian et al., 2017; Kohar et al., 2017). The Hill48 quadratic yield

function has been adopted in several studies due to its simplicity (e.g., Dunand and Mohr, 2010; Beese et al., 2010; Gross and Ravi-Chandar, 2014). The more advanced non-quadratic yield functions of Barlat and co-workers Yld2000-2D, Yld2000-3D and Yld04-3D have been shown in several studies to capture the anisotropy of Al-alloys most effectively (Yld2000-2D: Korkolis and Kyriakides, 2008, 2009; Pack et al. 2018. Yld2000-3D: Dunand et al., 2012; Gorji and Mohr, 2018. Yld04-3D: Giagmouris et al., 2010; Tardif and Kyriakides, 2012; Kohar et al., 2017; Dick and Yoon, 2018; Ha et al., 2018). Consequently, the Yld04-3D model is adopted in this dissertation.

Another essential component in large deformation and failure prediction analyses is an accurate representation of material hardening to large strains. The uniaxial tension test is commonly used to obtain the material response of sheet metal. The deformation in such tests stops being uniform at strains of the order of 10% due to necking. In sheet metal manufacturing practice, but also for some researches, the stress-strain response from a uniaxial test is often extrapolated to large deformations using one of the traditional fits such as the power-law hardening of Swift [1952] (e.g., Barsoum and Faleskog, 2007a; Bai and Wierzbicki, 2008; Dick and Yoon, 2018), the exponential hardening of Voce [1948] (e.g., Tian et al., 2017), or a combination of the two (Papasidero et al., 2014; Mohr and Marcadet, 2015; Ha et al., 2018). The extrapolated stress-strain curves are usually verified by numerically reproducing structural responses of one or a set of experiments. However, verification through comparison to local deformations is often neglected, which makes such extrapolations questionable. Bridgeman [1944] proposed an approximate analytical method to extract the stress-strain response of a round specimen based on measurements of the diameter and profile radius of the neck, which however can not be applied to sheet metals directly. Tardif and Kyriakides [2012] extracted stress-strain curves from uniaxial tension tests of Al-6061-T6 sheets through an inverse method and the stress-strain curves

were shown to depend on the yield function adopted. The study also pointed out the importance of incorporating anisotropy in the extraction of material hardening responses (see also Gross and Ravi-Chandar, 2015).

The hydraulic bulge test (e.g., Mellor, 1956; Young et al., 1981; Reis et al., 2017) is another commonly used test for establishing the material hardening of thin sheets. The metal is subjected to nearly equibiaxial tension at the bulge apex which enables extraction of the material hardening to much larger strain than the uniaxial tension test. However, the stress and strain at the bulge apex may deviate from equibiaxial state due to material anisotropy, which may also be unknown before calibration. Moreover, it is not clear how the material anisotropy affects the hardening extraction process.

Several simple shear tests are also used to extract the material hardening (e.g., Miyauchi, 1984; Kang et al. 2008; Yin et al., 2014; ASTM B831, 2014). For tubular specimen, pure torsion provides uniform shear deformation to quite large strains before failure (e.g., Chen et al., 2018; Scales et al., 2019). Again, the material anisotropy induced to the tubes due to the extrusion process must be appropriately incorporated in the hardening extraction.

1.3: OUTLINE

In summary, modeling ductile failure in thin walled structures such as sheets and tubes requires an accurate representation of anisotropy and a reliable stress-strain curve. While the hydraulic bulge test has been commonly used to establish the forming limit of sheet metals under equibiaxial loading condition (e.g., Yousif et al., 1970; Rees, 1995; Lazarescu et al., 2012), it also provides important data for anisotropy calibration (Barlat et al., 2003, 2005; Dick and Yoon, 2018), and is a powerful tool to extract sheet metal hardening response to large strains. In an attempt to facilitate a better understanding of the

role of material anisotropy in the constitutive modeling of thin-walled structures, the first part of this work investigates the effects of anisotropy on the hardening extraction, and on structural responses of hydraulic bulge tests. The second part of this work aims to establish a numerical scheme that can reproduce the results of a set of combined tension-torsion experiments conducted in parallel. The effects of anisotropy on the hardening extraction, instability and structural responses of tubular specimens under tension-torsion are addressed. The dissertation is organized as follows:

- Chapter 2 presents an iterative scheme to extract the material hardening responses of two anisotropic Al-alloys, Al-2024-T3 and Al-6022-T43, from bulge tests while simultaneously calibrating the material anisotropy.
- In Chapter 3, the calibrated constitutive models are implemented in 3-D finite element models, and used to simulate the bulge tests. Details such as structural responses and localization are presented.
- Chapter 4 presents calibration of anisotropy of Al-6061-T6 thin-walled tubes with data from tension-torsion and pressure-tension experiments. The material hardening response is extracted from a pure torsion test that accounts for the effects of material frame rotation.
- In Chapter 5, the calibrated constitutive model is implemented in a 3-D finite element model to simulate the tension-torsion experiments. The effect of anisotropy and hardening models on the structural responses and the evolution of localized deformation are presented.
- Finally, Chapter 6 summarizes the main conclusions from previous chapters and remarks on related future works.

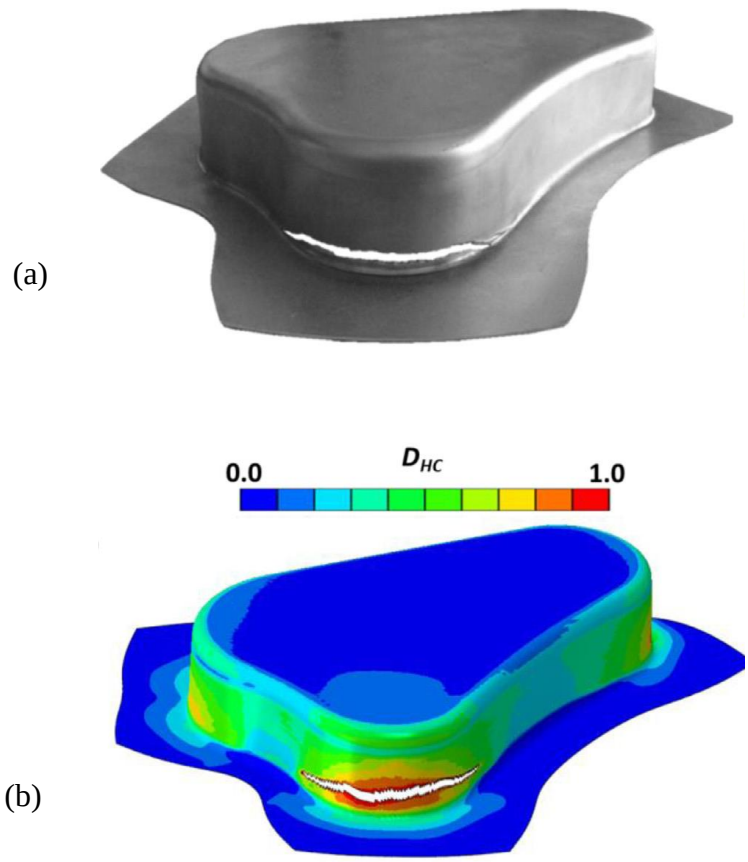

Fig 1.1 Triangular cup drawing of Al-6016-T4 sheet: (a) failed specimen and (b) numerical simulation (contour of Hosford-Coulomb fracture indicator superposed) (Pack et al., 2018).

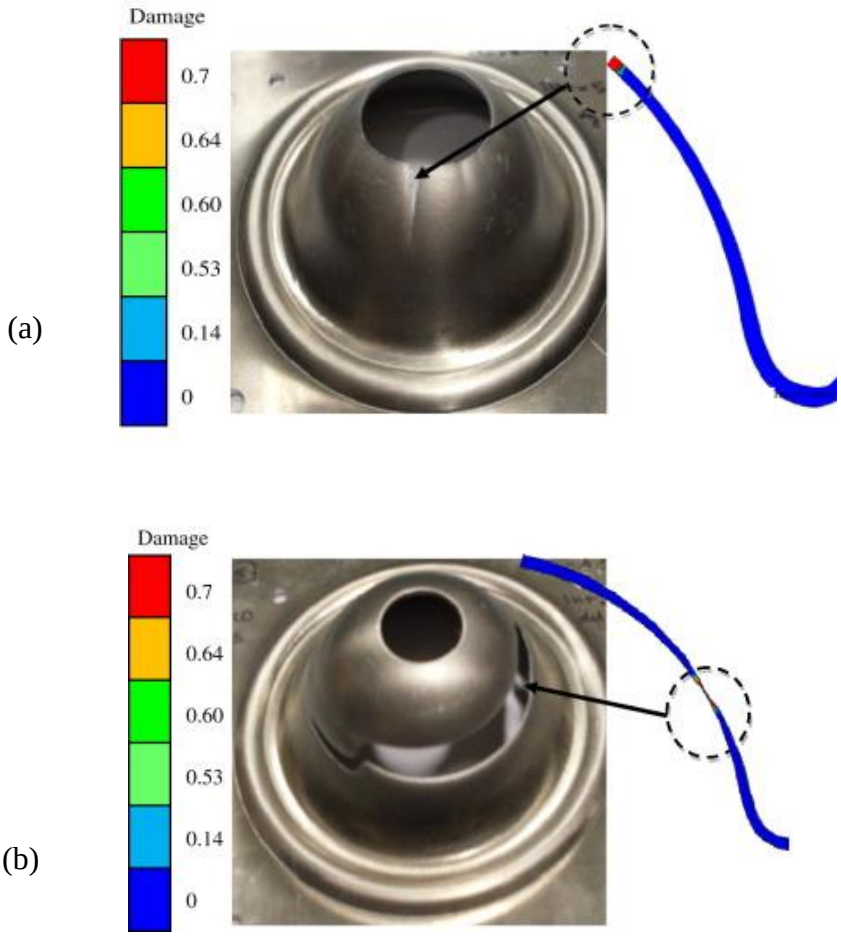

Fig 1.2 Two failure modes in the hot stamping of AA6082 sheet: (a) fast forming rate (0.64±0.01 m/s) failure due to radial tearing from the central hole and (b) slow forming rate (0.166±0.01 m/s) failure due to circumferential tearing at a mid-height location (Mohamed et al., 2012).

Fig 1.3 Failure of Al6063-T6 tube after axial crushing (courtesy of Dr. Kaan Inal).

Chapter 2: Constitutive Modeling of Hydraulic Bulge Tests[1] [2]

2.1 INTRODUCTION

The hydraulic bulge test has long been viewed as an essential complement to standard uniaxial tension tests in the material characterization of sheet metal. In its simplest form the test involves a circular disc clamped at the edge that is inflated with hydraulic pressure. The nearly equibiaxial stress state at the apex, and the continuous reduction in local radius as the bulge height increases, delay wall thinning and the limit pressure instability. Therefore, the material response extends to strain levels that are significantly larger than those of uniaxial tension tests. Extraction of the material response from this test requires first measurement of the local radius and strain at the apex, and second a flow rule appropriate for the material.

Early measurements of the radius and strain at the bulge apex were manual and cumbersome (Mellor, 1956), and often required interrupting the test (e.g., Ranta-Eskola, 1979). Measurements became automated and continuous by the introduction of a spherometer to measure the radius of the apex of the bulge combined with an extensometer mounted in the same device (Young et al., 1981). These innovations enabled the wider use of the bulge test in sheet metal material characterization (e.g., Santos et al., 2010). The test is also used to establish failure under equibiaxial stress states (e.g., Swift, 1952). Furthermore bulge tests employing elliptical shapes are used to develop forming limit

[1] Chen, K., Scales, M., Kyriakides, S., Corona, E. (2016). Effects of anisotropy on material hardening and burst in the bulge test. *Int'l J. Solids Struct*. **82**, 70-84. (Chen conducted the analysis, numerical simulations and helped write the paper)

[2] Chen, K., Scales, M., Kyriakides, S. (2018a). Material hardening of a high ductility aluminum alloy from a bulge test. *Int'l J. Mech*. Sci. **138-139**, 476-488. (Chen conducted the analysis, numerical simulations and helped write the paper)

diagrams for various biaxial stress states (e.g., Yousif et al., 1970; Rees, 1995; Banabic, et al., 2001).

The recent advent of more-advanced deformation diagnostic techniques has further simplified the acquisition of these measurements (e.g., Dziallach et al., 2007; Rana et al. 2010; Koc et al., 2011). The development of digital image correlation (DIC) has provided perhaps the most direct technique for continuous monitoring of the surface strains and shape of the apex (e.g., Vucetic et al., 2011; Friebe et al., 2013—see also Lazarescu et al., 2013; Mulder et al., 2015).

Analytical considerations of the bulge test have an equally long history, beginning with Gleyzal [1948] and Hill's [1950] extension of an approximated but insightful analysis of the problem. The approximate solution of an axisymmetric membrane bulge relating the height of the bulge to the induced strain was for a long time the standard tool for extracting the material response from the bulge test. Chakrabarty and Alexander [1970] pushed Hill's analysis forward by considering the effects of material hardening. However, the influence of factors such as the bulge radius-to-thickness ratio and through thickness effects (e.g., Lemoine et al., 2011; Friebe et al., 2013; Mulder et al., 2015), and effects of different hardening behavior and anisotropy (e.g., Bramley and Mellor, 1966; Rees, 1995; Aretz and Keller, 2011; Reis et al., 2017) have remained issues of concern until today.

In this chapter we take what we consider a holistic approach to the analysis of the bulge test. The anisotropy of the sheet is established through a separate set of experiments that are used to calibrate the Barlat et al. [2005] non-quadratic anisotropic yield function. The stress-strain response of the material is extracted from the measurements of the bulge test using the measured strains and radii of curvature at the apex. The stress state at the apex is not assumed to be equibiaxial a priori and consequently the extraction process involves an iterative solution of the relevant field equations. In keeping with the thesis that

extracted material responses are influenced by the constitutive model adopted (Tardif and Kyriakides, 2012), stress-strain responses are also extracted for the isotropic yield functions of von Mises and Hosford with an exponent of 8 (Hosford, 1972).

2.2 Establishment of the Stress State at the Apex

Extraction of the material stress-strain response from such bulge test results requires establishment of the induced stresses, at least at the apex. In the literature, the stress state at the bulge apex is commonly assumed to be equibiaxial (see Atkinson, 1997; Gutscher et al., 2004; Yanaga et al., 2012; Marandi et al., 2017), which is typically true for isotropic materials. The results of the bulge test presented in Section 2.2 of Chen et al. [2016] indicate that our sheet metal exhibits some anisotropy as the measured strains and radii of curvature at the apex in the x' (rolling) and y' (transverse) directions were somewhat different. In addition, a small amount of in-plane shear strain developed. We assume that a membrane state of stress exists so that the out-of-plane equilibrium at the apex is given by

$$\frac{t_{x'}}{r_{x'}} + \frac{t_{y'}}{r_{y'}} = \frac{P}{t}, \tag{2.1}$$

where $(t_{x'}, t_{y'})$ are the unknown true stresses in the two material directions, $(r_{x'}, r_{y'})$ are the measured local radii of curvature and t is the current apex thickness that is evaluated from incompressibility. A small amount of shear strain was measured due to both anisotropy and non-uniformities in clamping, and correspondingly a small amount of in-plane shear stress, $t_{x'y'}$, exists at the apex. It is convenient to form the following stress ratios:

$$t_{y'} = a t_{x'} \text{ and } t_{x'y'} = b t_{x'}, \tag{2.2a}$$

then

$$\tau_{x'} = \frac{P}{t}\left(\frac{1}{\rho_{x'}} + \frac{\alpha}{\rho_{y'}}\right)^{-1},\ \tau_{y'} = \frac{\alpha P}{t}\left(\frac{1}{\rho_{x'}} + \frac{\alpha}{\rho_{y'}}\right)^{-1} \text{ and } \tau_{x'y'} = \frac{\beta P}{t}\left(\frac{1}{\rho_{x'}} + \frac{\alpha}{\rho_{y'}}\right)^{-1} \qquad (2.2b)$$

Using the flow rule the stress ratios are related to the plastic instantaneous strain ratios as follows:

$$\frac{de^p_{y'}}{de^p_{x'}} = \frac{\partial \Phi / \partial \tau_{y'}}{\partial \Phi / \partial \tau_{x'}} = r_1(\alpha, \beta), \qquad (2.3a)$$

and

$$\frac{de^p_{x'y'}}{de^p_{x'}} = \frac{\partial \Phi / \partial \tau_{x'y'}}{\partial \Phi / \partial \tau_{x'}} = r_2(\alpha, \beta), \qquad (2.3b)$$

where F is an anisotropic yield function. Assuming elastic deformations to be negligibly small, the two strain ratios are evaluated directly from the measured strains. The nonlinear Eqs. (2.3) are solved numerically for α and β for each strain increment and the corresponding stresses are then evaluated from (2.2).

It should be noted the above formulation is necessary when the shear deformation cannot be neglected at the apex. For example, in the cases of elliptical bulge tests where the material axes are not aligned with the principal axes of the elliptical dies, a significant amount of shear strain is expected to develop in the material frame of an anisotropic material. However, for circular bulge tests of orthotropic materials, the shear strain developed at the apex is usually negligible compared with the normal strains in the material frame. Thus the formulation above reduces to the single stress ratio

$$t_{y'} = a t_{x'}, \qquad (2.4a)$$

and using Eq. (2.1)

$$\tau_{x'} = \frac{P}{t}\left(\frac{1}{\rho_{x'}} + \frac{\alpha}{\rho_{y'}}\right)^{-1} \text{ and } \tau_{y'} = \frac{\alpha P}{t}\left(\frac{1}{\rho_{x'}} + \frac{\alpha}{\rho_{y'}}\right)^{-1} \qquad (2.4b)$$

Similarly, using an anisotropic yield function, F, in the flow rule the instantaneous strain ratio is related to the stress ratio through

$$\frac{de^p_{y'}}{de^p_{x'}} = \frac{\partial \Phi / \partial \tau_{y'}}{\partial \Phi / \partial \tau_{x'}} = r(\alpha)\,. \tag{2.5}$$

The instantaneous strain ratio is evaluated from the measured strains by assuming the elastic deformations to be negligibly small. Equation (2.5) is solved numerically for each strain increment and the corresponding stresses follow from (2.4). The calculated stresses are used in the yield function to form the equivalent stress, t_e, while the plastic equivalent strain increment is given by:

$$de^p_e = \frac{t_{x'} de^p_{x'} + t_{y'} de^p_{y'} + 2t_{x'y'} de^p_{xy'}}{t_e}. \tag{2.6}$$

If the shear strain is small enough to be neglected, Eq. (2.6) reduces to

$$de^p_e = \frac{t_{x'} de^p_{x'} + t_{y'} de^p_{y'}}{t_e}. \tag{2.7}$$

Using this procedure the plastic equivalent stress-strain response of the material is generated incrementally. For comparison, material responses will also be generated for the isotropic yield functions of von Mises and the non-quadratic one due to Hosford [1972] (see Section 2.3). The apex in these cases is assumed to form a spherical cap with a radius ρ, which is calculated from the DIC data by fitting a sphere to the coordinates of all points within a 0.6-in (15.2 mm) radius of the apex. Thus the stresses are given by

$$t_1 = t_2 = \frac{Pr}{2t} = t_e. \tag{2.8a}$$

The measured logarithmic strains $(e_{x'}, e_{y'})$ are averaged and thus

$$de_1 = de_2 \text{ and } de^p_e = 2de^p_1. \tag{2.8b}$$

2.3 CONSTITUTIVE MODELS AND CALIBRATION

In past works it was demonstrated that the constitutive model used in the modeling of forming and other large deformation processes can influence the prediction of localization that precedes failure in thin-walled structures (Korkolis and Kyriakides, 2008a, 2008b, 2009; Korkolis et al. 2010; Giagmouris et al., 2010). Furthermore, Tardif and Kyriakides [2012] showed that the material response, which by necessity is usually extracted from inhomogeneous stress and strain states using inverse analysis, depends also on the constitutive model. Consequently three different constitutive models are adopted in the extraction of the stress-strain response. Non-quadratic yield functions are adopted in the modeling of the plastic behavior of the present Al-2024-T3 alloy, and anisotropy will be modeled through the 3-D yield function of Barlat and coworkers, Yld04-3D (Barlat et al., 2005).

In the modeling that follows, isotropic plasticity is modeled through Hosford's [1972] yield function, which in terms of the principal values of the stress deviator is given by:

$$|s_1 - s_2|^k + |s_2 - s_3|^k + |s_3 - s_1|^k = 2s_o^k \tag{2.9}$$

($k = 2$ represents the von Mises yield function). The exponent k is assigned the value of 8 as is typical for FCC alloys (Logan and Hosford, 1980).

Anisotropy is introduced using the yield function proposed in Barlat et al. [2005]. The model introduces anisotropy through two linear transformations to construct the tensors $\boldsymbol{S}'$, $\boldsymbol{S}''$ from the Cauchy stress tensor $\boldsymbol{\sigma}$ as follows:

$$\boldsymbol{S}' = \boldsymbol{C}'\boldsymbol{s} = \boldsymbol{C}'\boldsymbol{T}\boldsymbol{\sigma} = \boldsymbol{L}'\boldsymbol{\sigma} \text{ and } \quad \boldsymbol{S}'' = \boldsymbol{C}''\boldsymbol{s} = \boldsymbol{C}''\boldsymbol{T}\boldsymbol{\sigma} = \boldsymbol{L}''\boldsymbol{\sigma} \tag{2.10}$$

where $\boldsymbol{C}'$, $\boldsymbol{C}''$, $\boldsymbol{T}$, $\boldsymbol{L}'$ and $\boldsymbol{L}''$ are transformation matrices through which anisotropy is introduced. $\boldsymbol{T}$ is the standard linear transformation of $\boldsymbol{\sigma}$ to its deviator $\boldsymbol{s}$, while the $\boldsymbol{C}'$ and $\boldsymbol{C}''$ contain 18 anisotropy parameters as follows:

$$\boldsymbol{C}'=\begin{bmatrix} 0 & -c'_{12} & -c'_{13} & 0 & 0 & 0 \\ -c'_{21} & 0 & -c'_{23} & 0 & 0 & 0 \\ -c'_{31} & -c'_{32} & 0 & 0 & 0 & 0 \\ 0 & 0 & 0 & c'_{44} & 0 & 0 \\ 0 & 0 & 0 & 0 & c'_{55} & 0 \\ 0 & 0 & 0 & 0 & 0 & c'_{66} \end{bmatrix} \tag{2.11a}$$

and

$$\boldsymbol{C}''=\begin{bmatrix} 0 & -c''_{12} & -c''_{13} & 0 & 0 & 0 \\ -c''_{21} & 0 & -c''_{23} & 0 & 0 & 0 \\ -c''_{31} & -c''_{32} & 0 & 0 & 0 & 0 \\ 0 & 0 & 0 & c''_{44} & 0 & 0 \\ 0 & 0 & 0 & 0 & c''_{55} & 0 \\ 0 & 0 & 0 & 0 & 0 & c''_{66} \end{bmatrix} \tag{2.11b}$$

The principal values of the linearly transformed stress tensors $\boldsymbol{S}'$ and $\boldsymbol{S}''$, respectively (S'_1, S'_2, S'_3) and (S''_1, S''_2, S''_3), are evaluated analytically using Cardan's method. The solutions as well as the first and second derivatives of the yield function with respect to the stress components, which are required for the flow rule and a consistent tangent modulus, are given in Barlat et al. [2005] and Yoon et al. [2006]. The Yld04-3D yield function is then written as:

$$\begin{aligned} \Phi = [(&|S'_1 - S''_1|^k + |S'_1 - S''_2|^k + |S'_1 - S''_3|^k + |S'_2 - S''_1|^k + \\ &|S'_2 - S''_2|^k + |S'_2 - S''_3|^k + |S'_3 - S''_1|^k + |S'_3 - S''_2|^k + |S'_3 - S''_3|^k)/4]^{1/k} \end{aligned} \tag{2.12}$$

with $k = 8$.

2.3.1 Characterization of Anisotropy

The model is calibrated using the series of tests on specimens extracted from Al-2024-T3 sheet metal as recommended in Barlat et al. [2005] (see Chen et al. [2016]). Included are seven tensile stress-strain responses from specimens extracted at 15° intervals

between the rolling and transverse directions (Fig. 2.1a), and results from three plane strain tests on specimens extracted as shown in Fig. 2.1b. Since the main objective of the present study is the simulation and failure in bulge tests, we include in the calibration a set of data from the bulge test itself (Fig. 2.1c).

Figure 2.2a shows truncated the true stress-logarithmic strain responses from the seven tensile tests and Fig. 2.2b the axial vs. transverse strain plots.

The purpose of the plane strain tests is to provide additional results under biaxial stress states. Finite element analysis was used to design the specimen geometry to ensure nearly zero transverse strain at the center of the test section (see Fig. 2.3a). The in-plane strains in the test section were monitored with DIC. The axial strain was also monitored with a strain gage installed at the center of the backside of the specimen (provides an independent check of the DIC results). The results showed the transverse strain in the center of the specimen to be very small. The axial true stress (t_x) is evaluated from the recorded force by dividing by the current cross sectional area at mid-span as follows: $A_o/(1+e_x)=A$, where e_x is the axial strain in the center of the specimen and A_o is the initial cross sectional area ($w_o \times t_o$). Figure 2.3b shows the true stress-logarithmic strain responses recorded in the three directions. The small differences between them are caused by anisotropy.

a. Calibration of Al-2024-T3

The calibration of the anisotropic yield function (2.12) follows the procedure in Tardif and Kyriakides [2012] (similar to Appendix B of Barlat et al. [2005]), where the bulge test data were not available in their calibration. In the absence of through thickness shear measurements $\{c'_{44}, c'_{55}, c''_{44}, c''_{55}\}$ are assigned the value 1.0. The rest of the coefficients were determined by minimizing an error function that is developed as follows.

(i) *Uniaxial Tension Tests*

The plastic work is determined from the measured responses as follows:

$$W^p = \int_0^{e_{x1}} t_x de_x^p \quad \rightarrow \quad t_{xq}(W^p) \tag{2.13}$$

The stresses in the material frame $(x¢y¢)$ are given by

$$\boldsymbol{\tau}' = \{\tau_{x'}, \tau_{y'}, \tau_{x'y'}\}^T = \tau_{x\theta}(W^p)\{\cos^2\theta, \sin^2\theta, \sin\theta\cos\theta\}^T \tag{2.14}$$

Designating F as the yield function associated with (2.12),

$$\tau_{e\theta} = \Phi(\boldsymbol{\tau}') \tag{2.15}$$

and the following error function is established

$$\varepsilon_{\theta a} = \left(\frac{\tau_{e\theta}}{\tau_{x'0}(W^p)} - 1 \right)^2 \tag{2.16}$$

where $t_{x'0}(W^p)$ is the stress in the rolling direction stress-strain response at the chosen value of W^p (= 3000 psi—20.7 MPa) from (2.13).

The R_q values are determined by linearly fitting the measured e_x^p - e_y^p, which yields

$$r_{xy} = - \frac{de_y^p}{de_x^p}, \quad \text{and then} \quad R_{qex} = \frac{de_y^p}{de_z^p} = \frac{r_{xy}}{1 - r_{xy}}. \tag{2.17}$$

Using the flow rule evaluate

$$de_{ij}'^p = d\Lambda \frac{\partial \Phi}{\partial \tau_{ij}'} \text{ at } t¢_{ij}. \tag{2.18}$$

Transform $de_{ij}'^p \rightarrow de_{ij}^p$ and evaluate $\dfrac{de_y^p}{de_z^p} = R_{qf}$ and form the error function

$$\varepsilon_{\theta R} = \left(\frac{R_{\theta\phi}}{R_{\theta ex}} - 1 \right)^2. \tag{2.19}$$

(ii) *Plane Strain Tests*

W^p is defined again as in (2.13). t_y was assumed to be $t_x/2$ (introduces a small error). Then

$$\{t_{x¢}\, t_{y¢}\, t_{x¢¢}\} = \{t_x, t_y, 0\}\big|_{W^p}\, T_1(q), \tag{2.20}$$

where $T_1(q)$ is the usual transformation matrix for 2-D stress states. The equivalent stress t_{eq} at the same W^p based on $\{t_{x¢}\, t_{y¢}\, t_{x¢¢}\}$ is evaluated from (2.15) and is compared to $t_{x'0}(W^p)$ in an error function like the one in (2.16).

(iii) *Bulge Test*

The measured plastic strains $\{e^p_{x¢}\, e^p_{y¢}\, e^p_{x'y'}\}$ at the apex and estimates of the stresses $\{t_{x'}, t_{y'}, t_{x'y'}\}$ are used to evaluate t_e at the chosen value of W^p. This is then compared to $t_{x'0}(W^p)$ in an error function like the one in (2.16). The flow rule (2.18) is then used to evaluate the strains $de^p_{ij¢}$ at the chosen values of $(t_{x¢}\, t_{y¢}\, t_{x¢¢})$ forming the ratio $r_b = \dfrac{de^p_{y¢}}{de^p_{x¢}}$. This is compared with the constant experimental value $r_{b\,\mathrm{ex}}$ in Fig. 2.4a in the following error function:

$$\varepsilon_{rb} = \left(\frac{r_b}{r_{bex}} - 1\right)^2 \tag{2.21}$$

The optimal values of the anisotropy coefficients (c'_{ij}, c''_{ij}) are then chosen by minimizing the following weighted sum of these error functions:

$$\varepsilon(c'_{ij}, c''_{ij}) = \sum_m \omega_m \left(\frac{\tau_{e\phi}}{\tau_{x'0}} - 1\right)^2_m + \sum_n \omega_n \left(\frac{R_\phi}{R_{ex}} - 1\right)^2_n, \tag{2.22}$$

where the first series represents the errors from the m flow stresses, the second the errors from the n r-values established, and (w_m, w_n) are weight functions that represent the confidence level assigned to each particular experiment. In particular, larger weight functions are assigned to the bulge test to better capture the anisotropy near equibiaxial stress state. The minimization was performed using the routine *NMinimize* of Mathematica.

Note that the flow stresses $\{t_{x'}, t_{y'}, t_{x'y'}\}$ corresponding to the measured strains at the apex of the bulge test must be established. Since the extraction of the stresses depends on the yield function adopted as described in Section 2.2, the calibration becomes somewhat more complicated and requires an iterative process. In each iteration, the uniaxial and plane-strain test data used in the error function (2.22) is not changed, while data from the bulge test is updated from one iteration to the next.

(i) The initial values of the stresses and strain ratio at the apex are set at

$$\tau_{x'} = \tau_{y'} = P\rho / 2t\,,\ \tau_{x'y'} = 0 \text{ and } de^p_{y'} = de^p_{x'} = 1 (\equiv r_b)$$

The error function (2.22) is minimized yielding a first guess for $\{c_{ij}, c'_{ij}\}$.

(ii) The stress history at the apex is recalculated using the newly-calibrated yield function and flow rule as outlined in Section 2.2. The new values of the stresses and plastic strains are used to establish new values of $\{t_{x'}, t_{y'}, t_{x'y'}\}$ and r_b at the chosen value of W^p (= 3000 psi—20.7 MPa).

(iii) The new values of $\{t_{x'}, t_{y'}, t_{x'y'}\}$ and r_b are compared with the corresponding values in the previous iteration. If they do not agree, the new values are used to re-calibrate the yield function. The process is repeated until the results converge. The converged values of the anisotropy parameters are listed in Table 2.1.

Table 2.1 Yld04-3D anisotropy parameters for Al-2024-T3

c'_{12}	c'_{13}	c'_{21}	c'_{23}	c'_{31}	c'_{32}	c'_{44}	c'_{55}	c'_{66}
1.1733	1.0323	1.0437	0.9667	0.5371	0.9256	1.0	1.0	1.1697
c_{12}	c_{13}	c_{21}	c_{23}	c_{31}	c_{32}	c_{44}	c_{55}	c_{66}
0.5210	1.1038	0.9028	1.0024	1.1343	1.1124	1.0	1.0	0.8924

Figure 2.4a shows a plot of measured values of $e_{x'}$ vs. $e_{y'}$ at the apex forming a ratio of 1.044. The value calculated forms essentially the same ratio and is not included in

the figure. Figure 2.4b shows plots of the calculated stress-logarithmic plastic strains at the apex in the rolling and transverse directions. They follow essentially identical trajectories, which is a reflection of the near unity of the measured r_b.

In general the results of such calibration processes are not unique. In the way of evaluating the performance of the calibration process, the calibrated yield function and some of the corresponding experimental points are compared in Fig. 2.5 (T≡ tension, PS≡ plane strain, Bu≡ bulge test). Plotted are the stresses $t_{x'}/t_{x'0}$ vs. $t_{y'}/t_{x'0}$ for different values of normalized shear stress ($t_{x'y'}/t_{x'0}$) where $t_{x'0}$ is the measured stress in the x' direction at the chosen value of W^p (as in Barlat et al., 2005). The comparison of measurements and the calibrated yield contours is quite favorable.

It is interesting to perform a similar comparison of the experimental stresses with predicted work contours using the Hosford yield function (2.9) with exponent 8. The comparison is performed in Fig. 2.6. Differences between the calculated work contours and all but two experimental points are observed. Clearly these differences are mainly caused by anisotropy.

b. Calibration of Al-6022-T43

To test the robustness of the extraction scheme, a bulge test was conducted on a more ductile aluminum alloy Al-6022-T43 (see Chen et al., 2018a). In this case the shear strain at the apex is negligibly small which simplifies the calibration process. Figure 2.7a shows a plot of measured values of $e_{x'}$ vs. $e_{y'}$ at the apex forming a ratio of 1.18, which is a manifestation of the more significant anisotropy than that of Al-2024-T3. Following the similar iteration procedure to that outlined above, the stress state at the apex is established. It is plotted against the measured logarithmic plastic strains in the rolling and

transverse directions in Fig. 2.7b. It can be seen that the stresses in the two directions are significantly different due to the pronounced anisotropy of the material.

The bulge test data are again used in combination with seven uniaxial tension tests and three plane strain tension tests (see Chen et al., 2018a) to calibrate the Yld04-3D model through a similar process but at relatively lower plastic work $\bar{W}^p = 10.3$ MPa (1500 psi). The values of the anisotropy parameters determined from this calibration process are listed in Table 2.2.

The calibrated yield contours and some of the corresponding experimental points are compared in Fig. 2.8 at $\bar{W}^p = 10.3$ MPa (1500 psi) for different values of normalized shear stress $(t_{x'y'} / t_{x'0})$. The comparison of experimental data and the calibrated work contours is quite favorable. Figure 2.9 shows a similar comparison of the work contours corresponding to the isotopic version of the yield function in Eq. (2.9) (H8) with the same experimental data. Significant differences between the calculated work contours and all but two experimental points are observed, which must be the result of the anisotropy in the sheets. The results in Figs. 2.8 and 2.9 provide further support for the validity of the results of the anisotropy calibration procedure.

Table 2.2 Yld04-3D anisotropy parameters for Al-6022-T43

c'_{12}	c'_{13}	c'_{21}	c'_{23}	c'_{31}	c'_{32}	c'_{44}	c'_{55}	c'_{66}
1.0140	0.5047	0.7951	0.6976	0.5089	0.4509	1.0	1.0	1.1980
c''_{12}	c''_{13}	c''_{21}	c''_{23}	c''_{31}	c''_{32}	c''_{44}	c''_{55}	c''_{66}
1.0217	1.4496	0.8892	1.1418	1.3136	1.5447	1.0	1.0	0.5664

In closing this section, it is worth pointing out that the performed calibration of the Yld04-3D is influenced by the weights adopted in the optimization function (2.22). These are based on the degree of confidence placed on each measurement. In the present iterative

scheme used, the results can also be influenced to some degree by the initial guess in the bulge apex stress values (step (i) above).

2.3.2 Extraction of the Stress-Strain Response from the Bulge Test

Once the in-plane stresses at the bulge apex are evaluated, the equivalent stress can be established using the yield function (2.12). The corresponding equivalent plastic strain is then established for each value of stress using (2.6) or (2.7). The resultant equivalent stress-plastic strain response is shown in Fig. 2.10 (Yld04-3D). Included are the measured tensile responses in the rolling and transverse directions, which terminate at strains of about 12% because of localized necking. As expected, the bulge test response extends to about 27.5% plastic strain. Its trajectory has a similar shape as those of the uniaxial responses and falls closer to the x' response. At higher strain values the plastic modulus continues its gradual reduction, a clear indication that linear extrapolation of uniaxial tensile stress-strain data beyond the values at the load maximum is not prudent.

Included for comparison is the material response extracted from the bulge test using the Hosford yield function (H8) assuming isotropic yielding and fitting the apex with a best-fit sphere. Under these conditions the von Mises yield function yields the same results (vM). The calculated response has a similar shape to that yielded by Yld04-3D but traces a somewhat lower stress.

Finally, it is worth pointing out that because the anisotropy of the Al-2024-T3 sheet analyzed is relatively modest, the contribution of the shear stress-strain response at the apex, $(t - e^p)_{x'y'}$ is quite small. Consequently, neglecting the shear strain at the apex does not alter either the anisotropy parameters or the extracted stress-strain response in any significant manner.

In a similar fashion, the equivalent stress-strain response for Al-6022-T43 is also extracted from bulge test data, as shown in Fig, 2.11. The response has a yield stress of about 138 MPa (20 ksi) and rises to 379 MPa (55 ksi) at the terminal strain of just over 0.60. Included in the figure are the measured uniaxial responses in the rolling, x', and transverse, y', directions. The two responses exhibit a similar hardening, with the rolling direction uniaxial response tracing a slightly higher stress trajectory, and the transverse direction slightly lower. Both terminate at strains of about 0.20, which demonstrates the advantages of using the bulge test to establish the material response of sheet metal.

Also included in Fig. 2.11 is the stress- strain response extracted from the bulge test results using the von Mises (vM) and Hosford yield functions (H8). The response follows a similar trajectory, tracing slightly lower stress levels than the Yld04-3D results. This can be explained by comparing the work contours corresponding to $t_{x'y'} = 0$ of the three models in Fig. 2.9. In the neighborhood of equibiaxial stress the three contours are very similar which leads to similar equivalent stress for the extracted response. The implications of this similarity on the numerical simulation of the bulge test will be discussed in Chapter 3.

2.3.3 Comparison with Swift and Voce Extrapolations

In the sheet metal manufacturing practice the bulge test is often avoided. The alternative method of extracting the material response from the necked regime of a uniaxial test using inverse analysis (e.g., Tardif and Kyriakides, 2012) is even more challenging and less common. Instead, the stress-strain response from a uniaxial test is often extrapolated using one of the traditional fits such as that of Swift [1952] or Voce [1948]. The first, $t = k(A + e^p)^N$, assumes powerlaw hardening and in the second, $t = a + (t_o - a)\exp(-be^p)$, the hardening decays exponentially at higher strains. In the way of evaluating their performance against the stress-strain response extracted from the bulge

test, the two expressions are fitted to the uniaxial responses measured in the rolling direction. The fitting parameters are listed in Table 2.3 for Al-2024-T3 and Table 2.4 for Al-6022-T43, respectively. The resultant stress-plastic strain responses are plotted in Figs. 2.12a and 2.12b together with the responses extracted from the bulge tests.

Table 2.3 Parameters of the uniaxial stress-strain response fitting for Al-2024-T3

Swift			Voce		
k MPa (ksi)	A	N	a MPa (ksi)	t_o MPa (ksi)	b
800.5 (116.10)	0.0091	0.1922	598.8 (86.85)	240.7 (34.91)	11.61

Table 2.4 Parameters of the uniaxial stress-strain response fitting for Al-6022-T43

Swift			Voce		
k MPa (ksi)	A	N	a MPa (ksi)	t_o MPa (ksi)	b
483.4 (70.09)	0.0051	0.2512	347.3 (50.36)	163.0 (23.78)	9.459

It can be seen from Fig. 2.12a that for Al-2024-T3 that beyond plastic strain of about 0.15 the Swift fit overestimates the hardening responses while the Voce underestimates it. However, the difference between the two fits and the bulge test response is not very significant since the maximum strain extracted from bulge test is not sufficiently large.

For Al-6022-T43 the bulge response extends to a strain of 0.60, and the results of the two fits appear in Fig. 2.11b. The two expressions fit the bulge response well up to a plastic strain of about 0.20. But at higher strains the Swift extrapolation again overestimates the bulge response and the Voce extrapolation underestimates it. The deviations from the bulge response increase with strain and become unacceptably large at the highest strain values (see also Suttner and Merkelein, 2016; Reis, et al., 2017). Differences of this

magnitude in plastic modulus can lead to significant errors in the prediction of instabilities such as localization and wrinkling that are common in sheet metal forming.

2.4 SUMMARY AND CONCLUSIONS

The hydraulic bulge test enables direct measurement of the material stress-strain response of sheet metal to strains far larger than other tests. The nearly equibiaxial stress state and continuous reduction of the local radius at the apex delay wall thinning and the associated limit pressure instability.

A methodology has been developed for incorporating anisotropy in the extraction of the material stress-strain response from a bulge test. It requires accurate measurement of the deformation at the apex and a flow rule based on a yield function that captures the prevalent material anisotropy.

Because of the relatively large radius-to-thickness ratio of our bugle test, the usual assumption of a membrane state of stress at the apex is maintained but without assuming an equibiaxial state of stress or strain. Instead, the analysis uses the two measured radii of curvature and strains at the apex. The stresses are then evaluated through an iterative procedure that incorporates equilibrium and the flow rule based on the anisotropic yield function. Although the anisotropy in the sheet metals analyzed was relatively small, the extracted stress-strain response differs from the one produced by the isotropic yield functions.

Extrapolations of the uniaxial stress-strain response based on the commonly used Voce and Swift fits respectively underestimated and overestimated the actual response significantly.

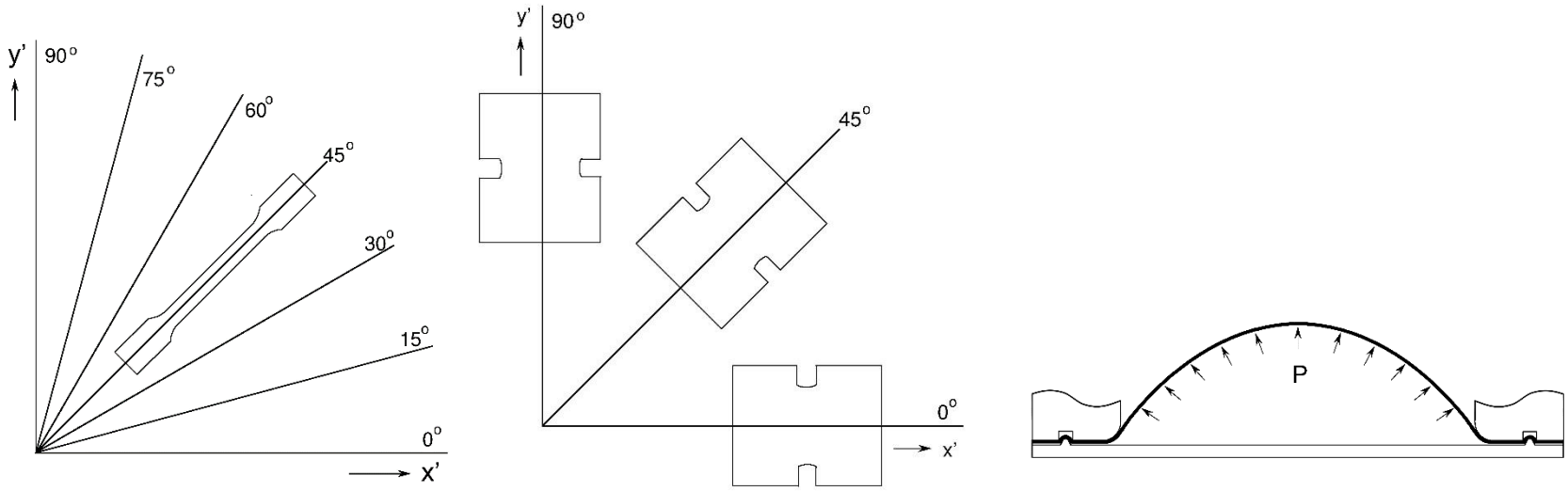

Fig. 2.1 Tests used to calibrate the Yld04-3D yield function. (a) Seven tension specimens extracted at 15° intervals. (b) Three plane-strain tension specimens extracted at 45° intervals. (c) Bulge test (Chen et al. [2016]).

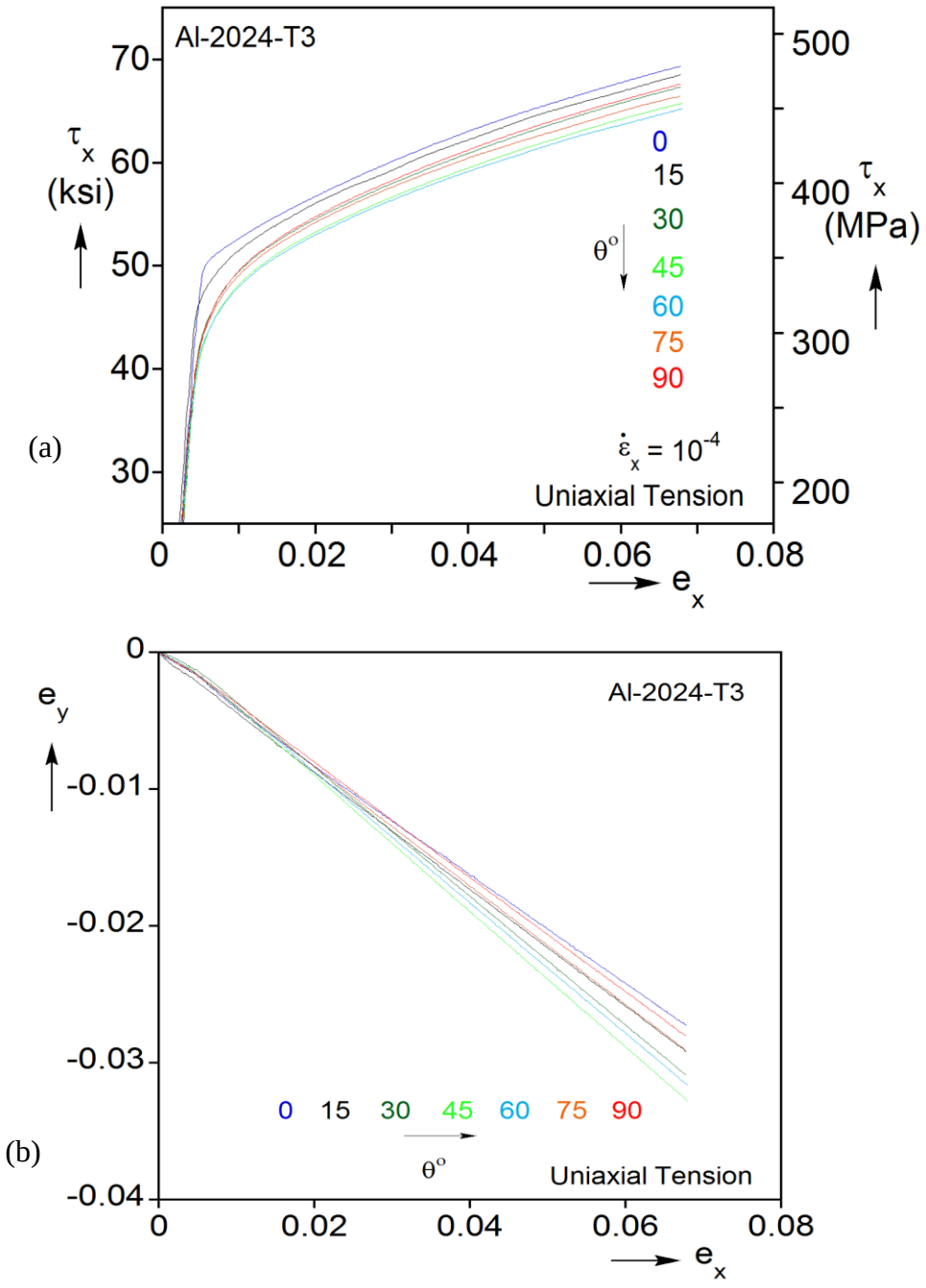

Fig. 2.2 (a) True stress-logarithmic strain responses for the seven uniaxial tension tests and (b) corresponding transverse strain vs. axial strain.

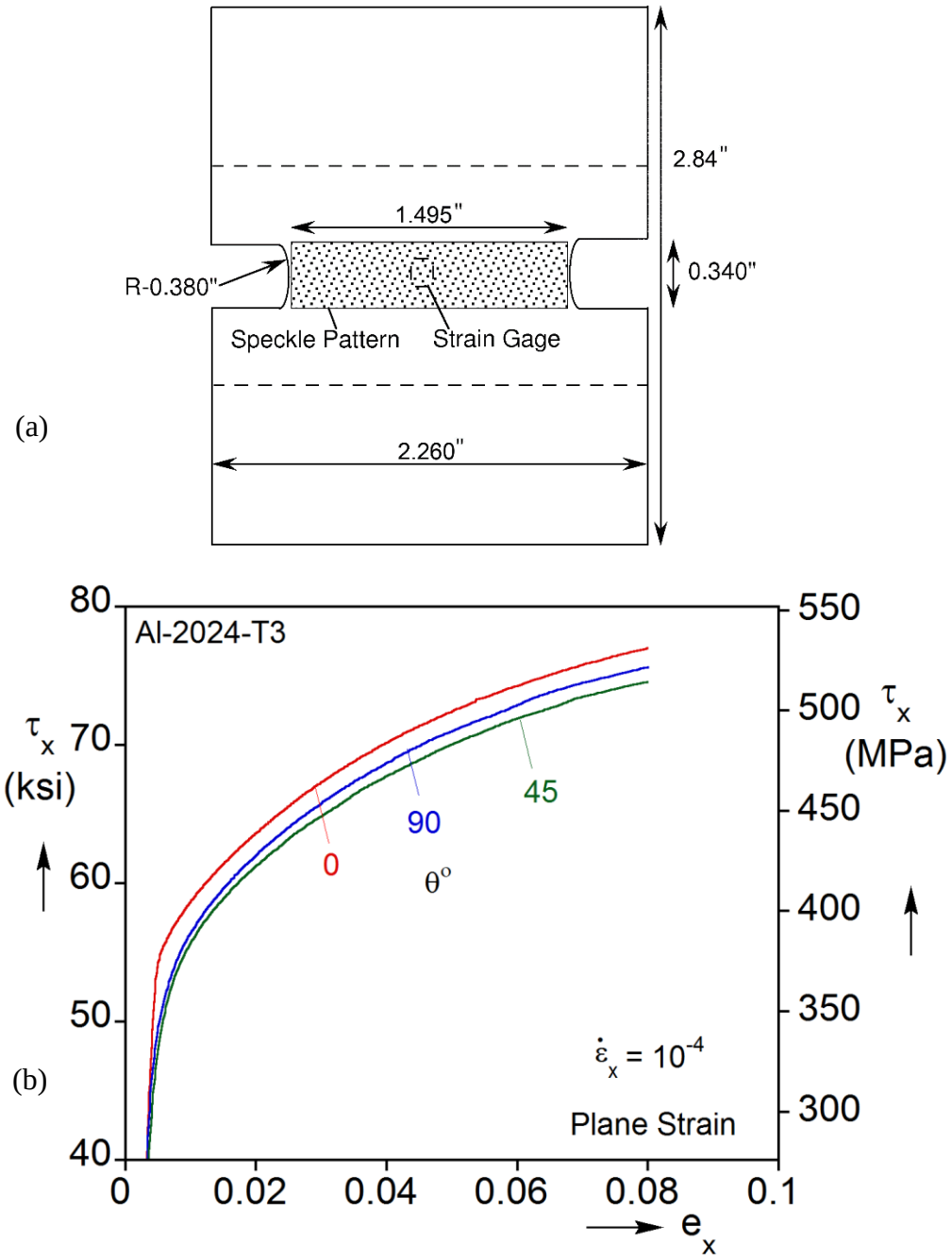

Fig. 2.3 (a) Plane-strain tension specimen and (b) axial stress-strain responses for the three tests.

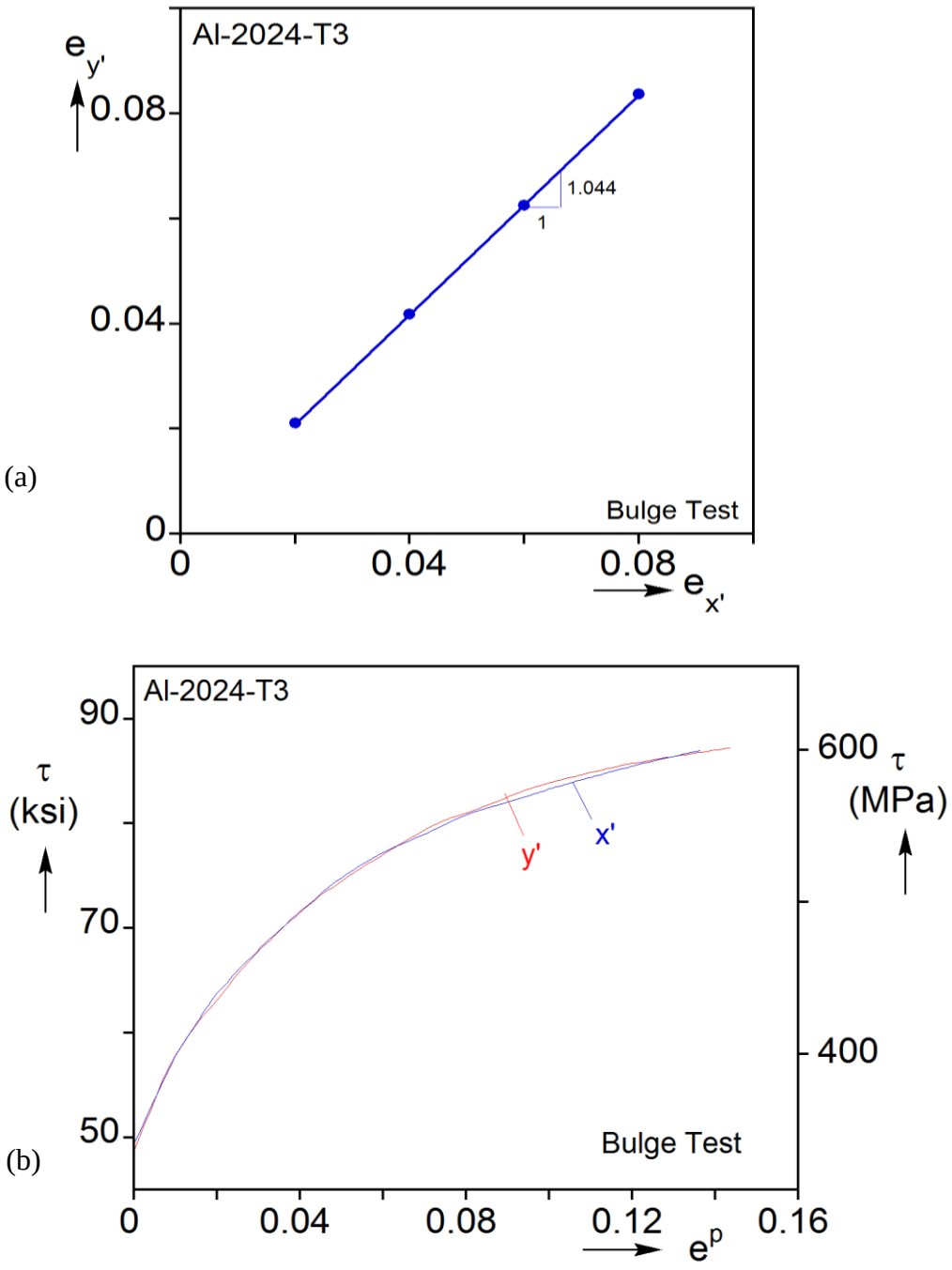

Fig. 2.4 (a) Transverse direction strain vs. rolling direction strain extracted from the bulge test of Al-2024-T3. (b) Calculated stress-plastic strain responses for the rolling and transverse directions of Al-2024-T3.

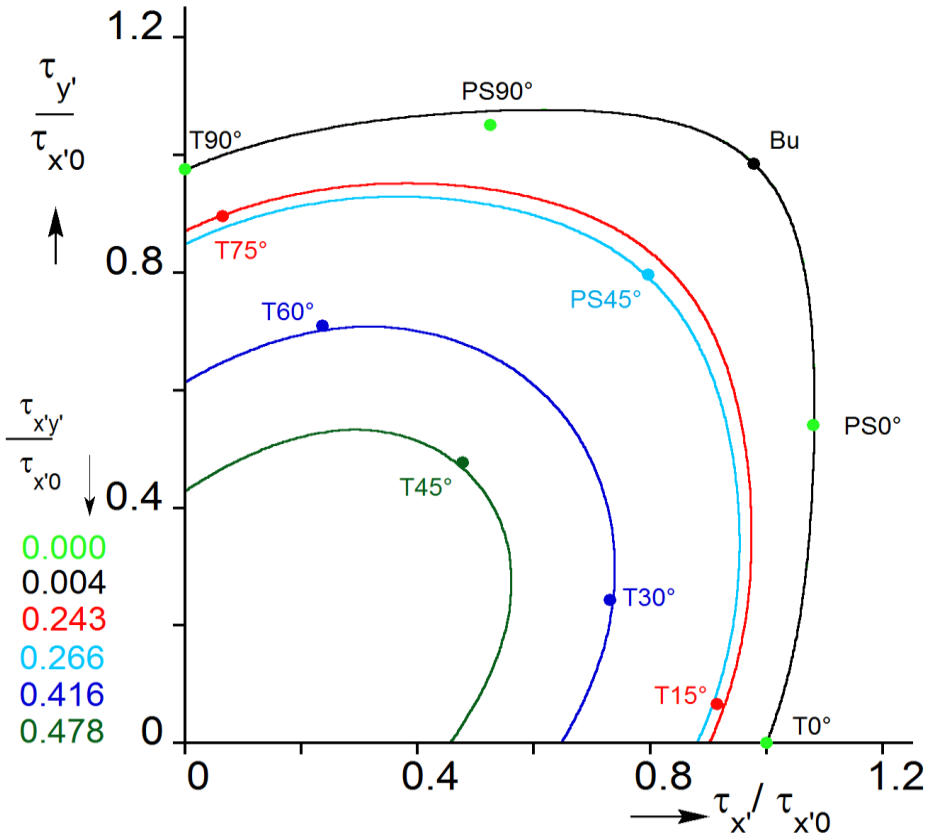

Fig. 2.5 Calibrated Yld04-3D yield surfaces for Al-2024-T3 for different values of normalized shear and experimental data points (solid bullets—T≡ tension, PS≡ plane strain, Bu≡ bulge test).

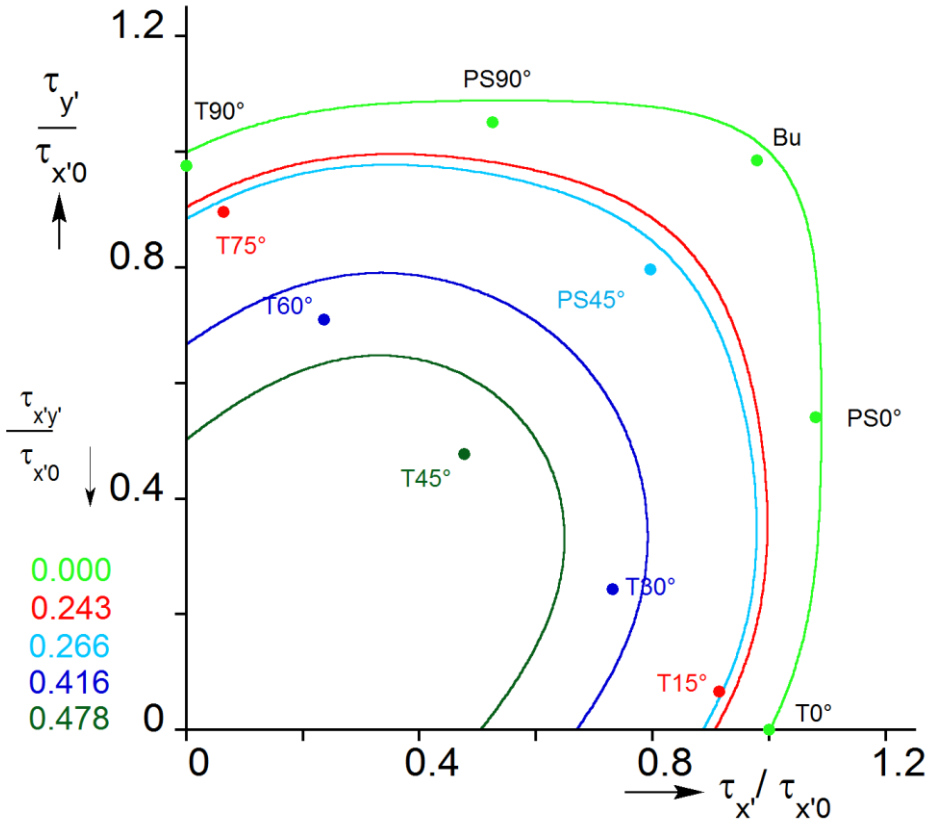

Fig. 2.6 H8 yield surfaces for different values of normalized shear compared with experimental data points (solid bullets) of Al-2024-T3.

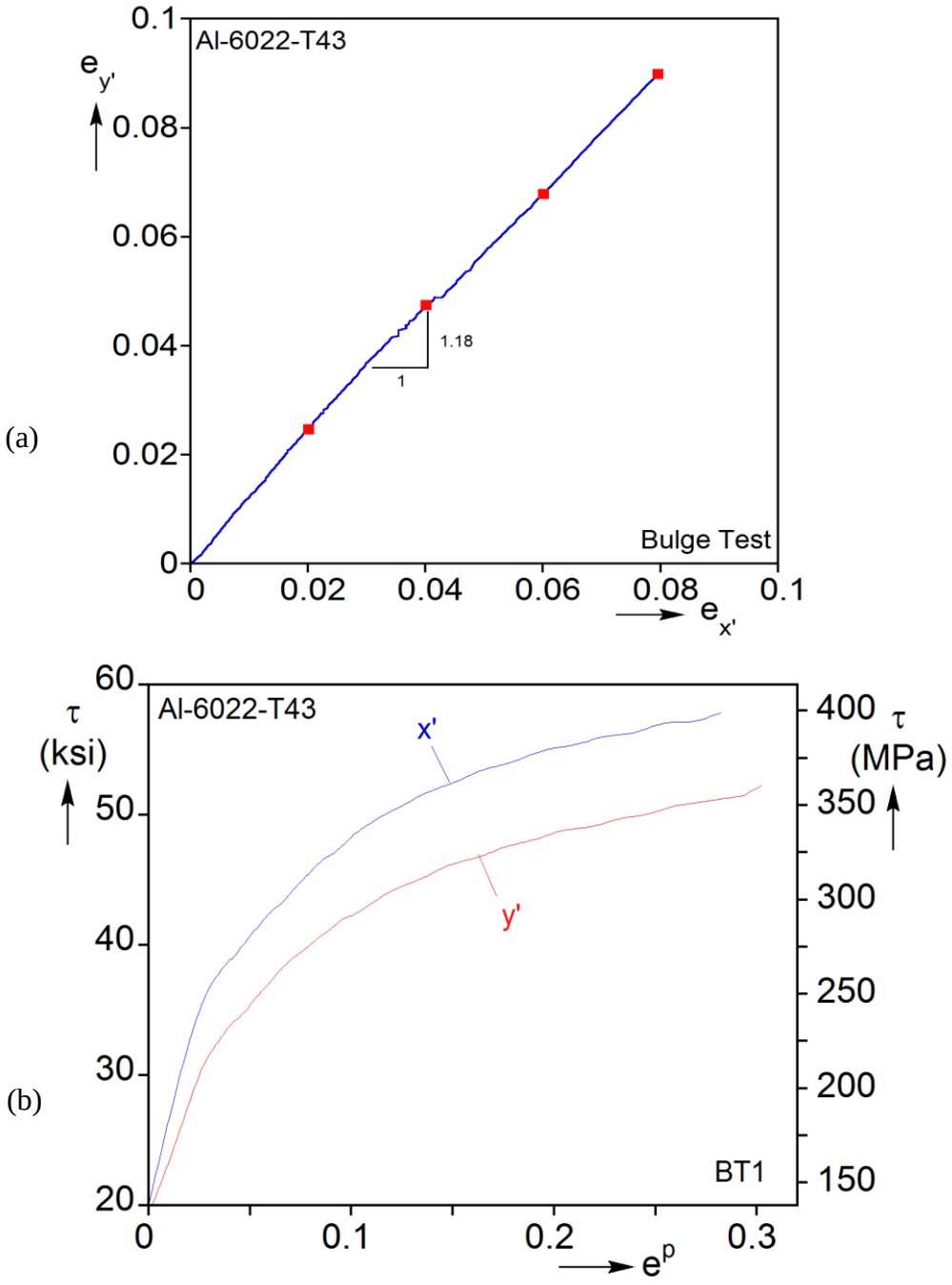

Fig. 2.7 (a) Transverse direction strain vs. rolling direction strain extracted from the bulge test of Al-6022-T43. (b) Calculated stress-plastic strain responses for the rolling and transverse directions of Al-6022-T43.

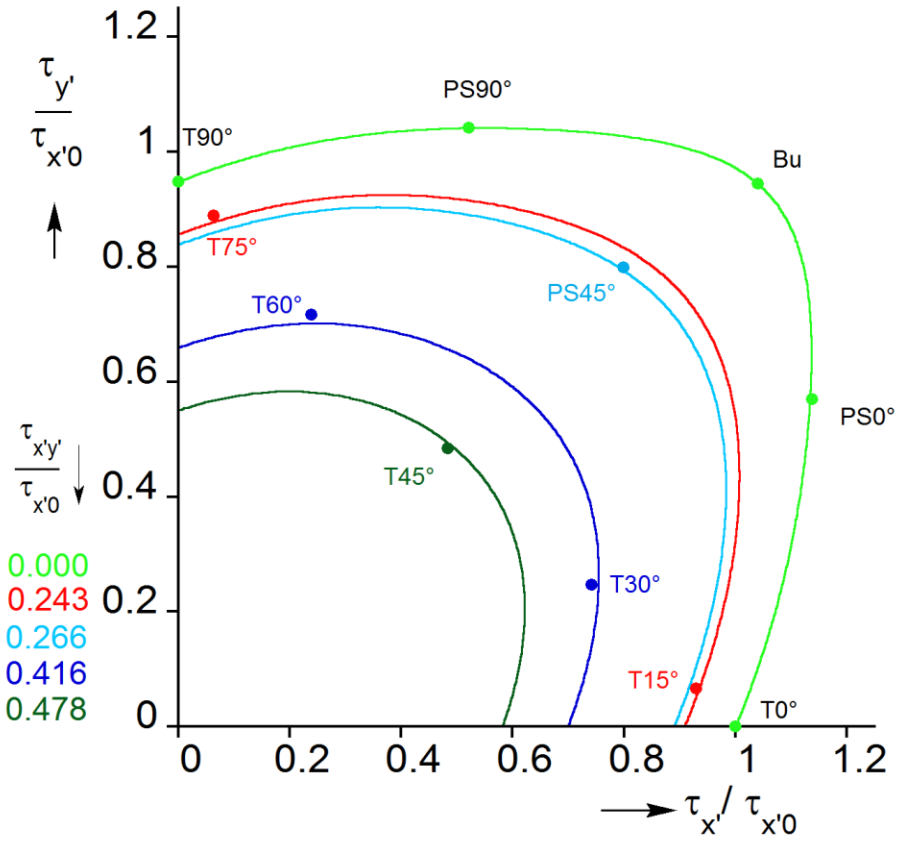

Fig. 2.8 Calibrated Yld04-3D yield surfaces for Al-6022-T43 for different values of normalized shear and experimental data points (solid bullets—T≡ tension, PS≡ plane strain, Bu≡ bulge test).

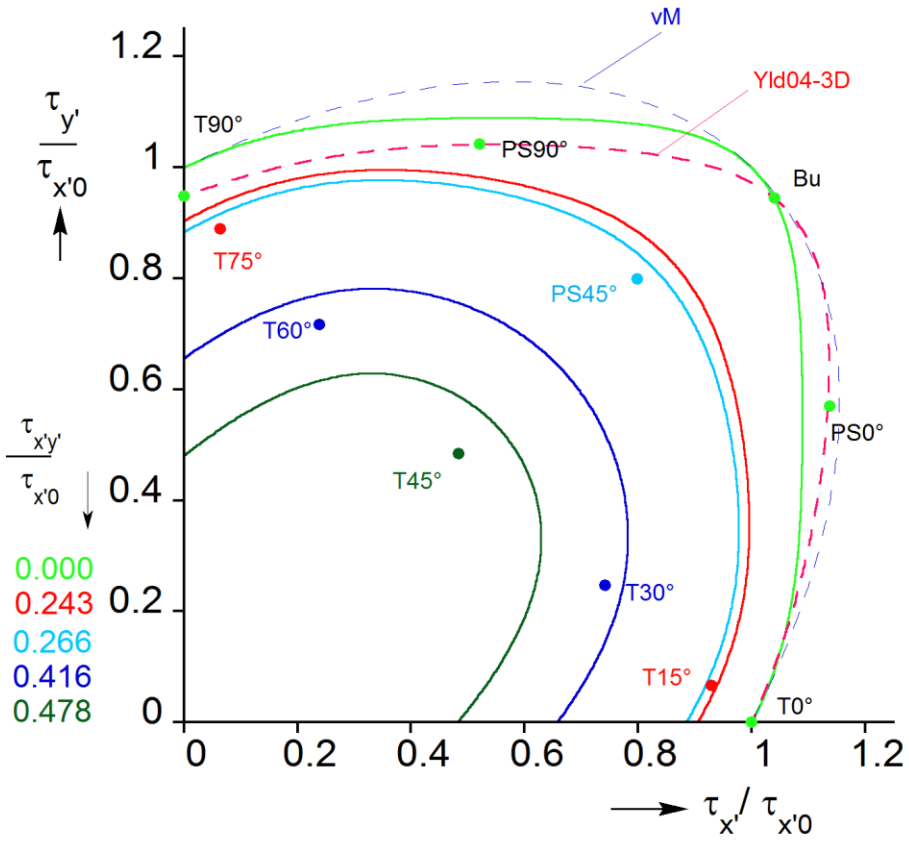

Fig. 2.9 H8 yield surfaces for different values of normalized shear compared with experimental data points (solid bullets) of Al-6022-T43.Included are vM and Yld04-3D yield surfaces for zero normalized shear stress.

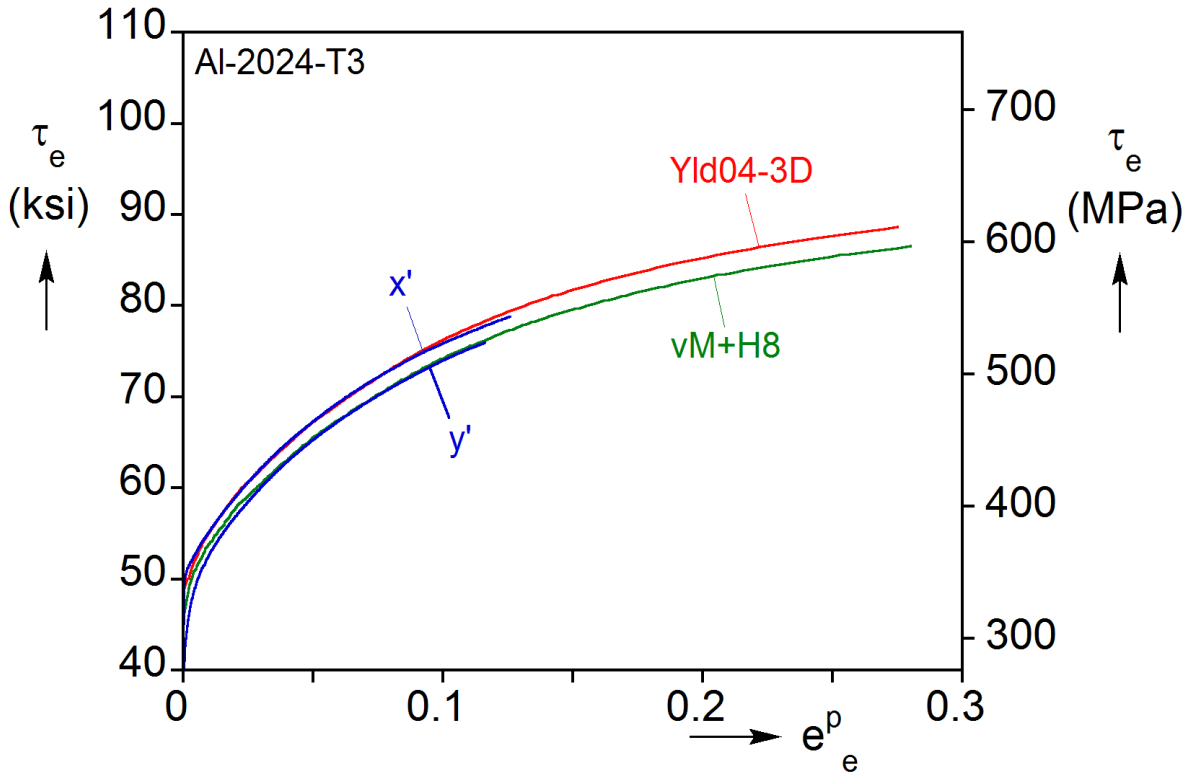

Fig. 2.10 Extracted equivalent stress-plastic strain responses for Al-2024-T3 using Yld04-3D, H8 and vM yield functions. Included are the stress-plastic strain responses from uniaxial tension tests in the rolling and transverse directions.

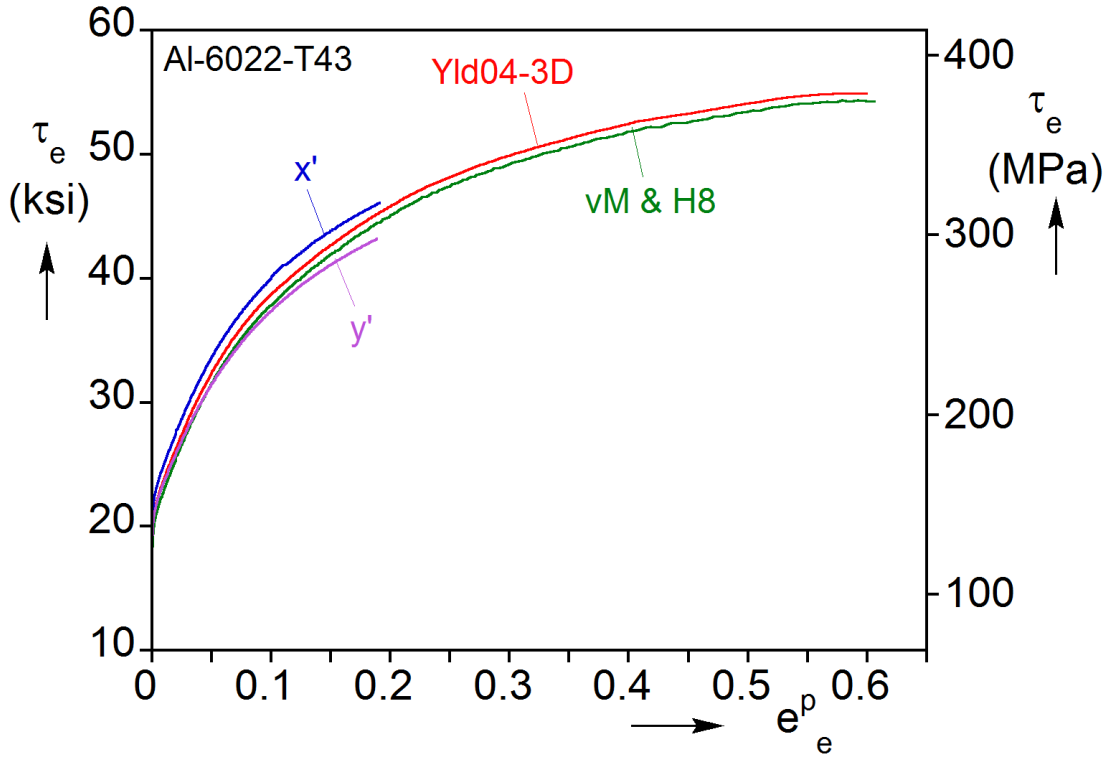

Fig. 2.11 Extracted equivalent stress-plastic strain responses for Al-6022-T43 using Yld04-3D, H8 and vM yield functions. Included are the stress-plastic strain responses from uniaxial tension tests in the rolling and transverse directions.

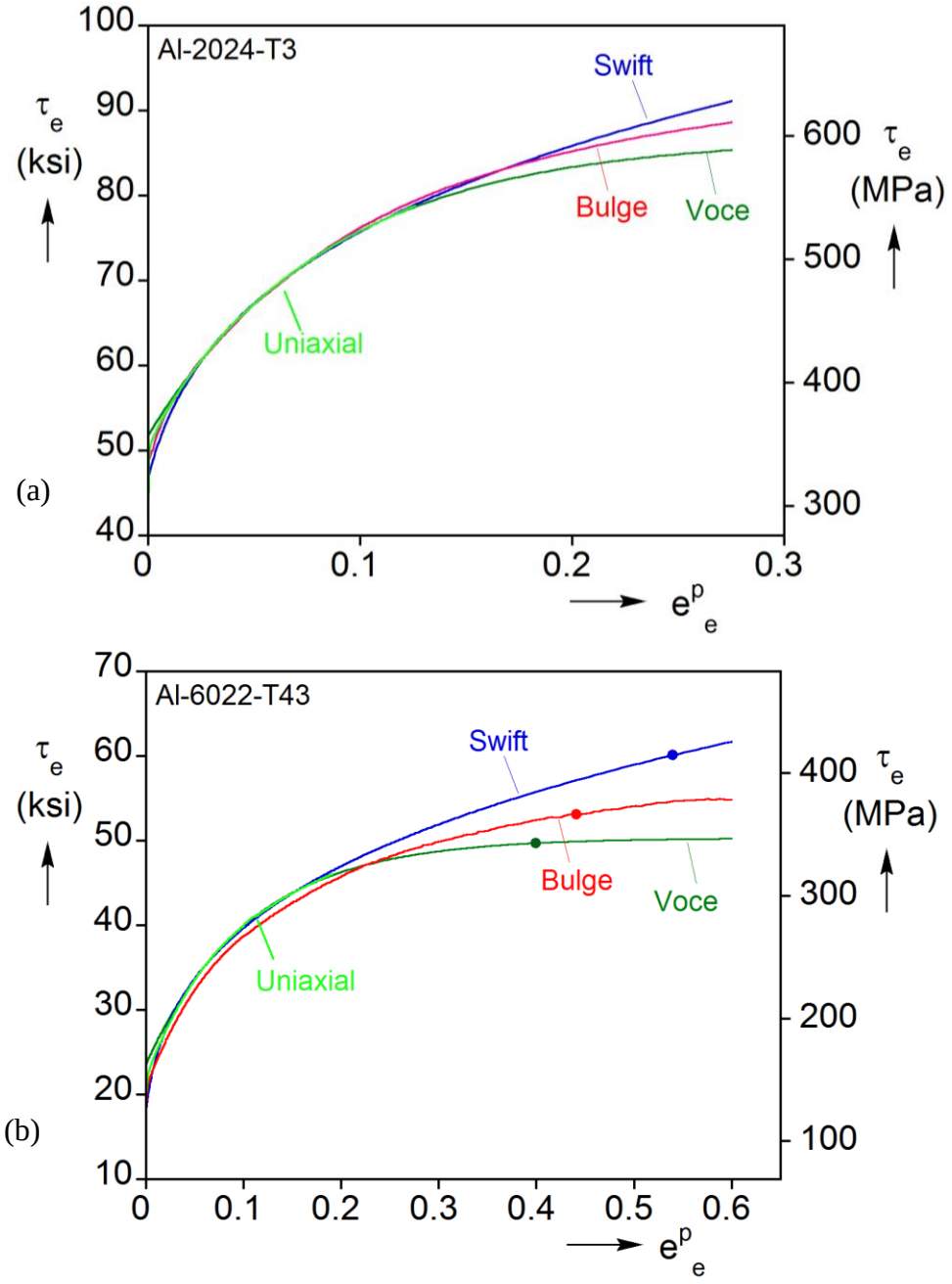

Fig. 2.12 Comparison of the equivalent stress-plastic strain response evaluated from the bulge test, and extrapolations of the uniaxial tension response of Swift and Voce for (a) Al-2024-T3 and (b) Al-6022-T43. The solid bullets in (b) identify the values of equivalent stress and strain at the pressure maximum predicted by Hill's approximate analysis of the bulge (see Appendix A).

Chapter 3: Numerical Simulation of Hydraulic Bulge Tests[3] [4]

Bulge tests performed on Al-alloy sheet metal using the testing facility in Chen et al., [2016] are simulated using 3-D finite element models developed in ABAQUS [2010]. The anisotropic yield function calibrated in Chapter 2 is incorporated via a UMAT (Yoon [2009, 2011]) together with the extracted hardening response of the material. Of particular interest is the effect of the constitutive model on the ensuing instability.

3.1 Idealized Finite Element Model

The test facility used to perform the bulge tests is shown schematically in Fig. 3.1. We start with an idealized model of the test set up that can be used for parametric studies of bulging. A model that more closely resembles the experimental setup will be discussed in Section 3.3. The idealized model consists of a complete disc and the contacting part of the clamping ring (see Fig. 3.2). The disc has a radius R_o =3.85 in (97.8 mm) and a wall thickness t_o = 0.040 in (1.02 mm). Its outer edge is at the location of the draw bead in the physical bulge tester so that its outer annulus is in contact with the clamping ring as shown in Fig. 3.2b. This leaves an open section of radius R = 3.00 in (76.2 mm).

The disc is discretized with eight-node, reduced integration, linear solid elements (C3D8R). For better visualization Fig. 3.2a depicts only a quarter of the actual disc mesh. Discretization details follow:

a. Five elements are used through the thickness.

---

[3] Chen, K., Scales, M., Kyriakides, S., Corona, E. (2016). Effects of anisotropy on material hardening and burst in the bulge test. *Int'l J. Solids Struct.* **82**, 70-84. (Chen conducted the analysis, numerical simulations and helped write the paper)

[4] Chen, K., Scales, M., Kyriakides, S. (2018a). Material hardening of a high ductility aluminum alloy from a bulge test. *Int'l J. Mech. Sci.* **138-139**, 476-488. (Chen conducted the analysis, numerical simulations and helped write the paper)

b. In order to facilitate the anticipated localization, a one-inch square section in the center of the disc is assigned a refined nearly-isotropic mesh with 42×40 elements. A narrow linear ($2w \times 2L_1$) thickness imperfection with thickness (t_o - D) is introduced at the center of this section to trigger localization as shown in the figure.

c. The mesh of the outer part of the model has a nearly-uniform angular distribution of elements of 2.195° and the following radial distribution of elements:

- For $2.85" \le r \le 3.85"$ ($72.4 \le r \le 97.8$ mm) there are 14 elements of the same width
- For $1.215" \le r \le 2.85"$ ($30.9 \le r \le 72.4$ mm) there are 20 elements with a bias ratio of 1.2
- The circular zone ($r \le 1.215"$—$r \le 30.9$ mm) that surrounds the fine square mesh has 16 elements with a bias ratio of 2.
- The nodes at the outer edge of the model are fixed.

d. The surface of the clamping ring is modeled as an analytical rigid surface that is fixed in space. It has a flat outer section and ends in a radius of 0.315 in (8.0 mm). Contact between the disc and the rigid surface of the clamping ring is frictionless. Surface-to-surface contact with "finite sliding" is adopted. An exponential “softened” contact pressure-overclosure relationship is used.

The model disc is pressurized by prescribing the fluid flux in a cavity below it (volume-controlled pressurization, see Fig. 3.2b). A cavity depth of 0.131 in (3.33 mm) is chosen to correspond to the height of the draw bead. The cavity is enclosed by 19924 four-node fluid elements (F3D4).

3.2 NUMERICAL RESULTS

3.2.1 Structural Responses

Numerical results for an imperfection amplitude of 0.01 t_o are now used to illustrate the performance of the model. Emphasis will be given to results based on the Yld04-3D constitutive model (Yoon [2009, 2011]), but select predictions based on H8 and vM will be included for comparison. Figure 3.3a shows the calculated pressure-cavity volume response (P- u/u_o, $\upsilon_o \equiv$ initial volume of cavity) and Fig. 3.3b the corresponding pressure-bulge height response (P- h/R). Both responses initially rise essentially linearly. They start to exhibit some reduction in stiffness around 1000 psi (69 bar). The stiffness reduction continues at an increasing pressure and in the absence of an imperfection would typically lead to a pressure maximum associated with the induced wall thinning. In the present case, the imperfection leads to localization, which in turn causes a pressure maximum at 1345.9 psi (92.82 bar) followed by a sharp drop in pressure.

It is important to emphasize that because of the anisotropy, a separate study was performed to determine the orientation of the imperfection at which the lowest maximum pressure occurred. Figure 3.4 shows the pressure maximum calculated for different orientations for a thickness imperfection of 1%. The minimum value is achieved when the linear imperfection is oriented at about 45^o to the rolling direction. This orientation is selected for all subsequent calculations using Yld04-3D.

3.2.2 Localization

An expanded P- u/u_o plot of the neighborhood of the pressure maximum is shown in Fig. 3.5a and six corresponding deformed configurations of the zone containing the imperfection appear in Fig. 3.5b (the imperfection is four elements wide by forty elements long). Color contours superimposed on the images correspond to the equivalent

plastic strain. Image ① is well before the pressure maximum and as a result the strain inside the imperfection band is approximately the same as the full-thickness material on either side of it. In image ②, closer to the maximum, the deformation inside the band starts to grow faster than its neighborhood. In image ③, essentially at the pressure maximum, the strain inside the band has grown even more and the difference with the strain outside it becomes more distinct, all strong signs that the deformation is localizing in the band. Indeed the localization accelerates in images ④ to ⑥ with the overall pressure decreasing sharply.

A more quantitative view of the localized wall-thinning that takes place in the neighborhood of the pressure maximum is shown in Fig. 3.6 where the through-thickness logarithmic strain, e_z, at two points at the apex of the bulge are plotted against u/u_o. Point A is inside the band at the apex and point B corresponds to the second element from the edge of the imperfection on the common meridian that is perpendicular to the band. The wall thinning at the two points follows the same trajectory up to a volume of about 4.4 u_o, which corresponds to a pressure of 1140 psi (78.6 bar). Beyond this point the two trajectories start to deviate from each other with the strain at point A growing progressively faster. As the value of u/u_o that corresponds to the pressure maximum is approached, the wall thinning at point A experiences precipitous growth at $P_{\max}$ and beyond. By contrast, e_z at point B follows the expected trend up to $P_{\max}$ and starts to increase beyond it due to the drop in the pressure under the bulge. The strain inside the band becomes unrealistically large and the calculation is terminated soon after point ⑥. Alternatively, the calculation can be terminated with the introduction of a failure criterion. Even at the pressure maximum the strain within the imperfection reached values on the order of 50%. Since our measured material response terminated at a strain of about 30%, it was extrapolated linearly

to allow the calculation to continue. Because of this calculations beyond $P_{\max}$ are less dependable.

3.2.3 Yield Function and Imperfection Sensitivity

Similar calculations were performed using the vM and H8 yield functions and the corresponding stress-strain response (see Fig. 2.10). These are isotropic models and thus the orientation of the imperfection does not affect the results. The calculated P-u/u_o and P-h/R responses are included in Figs. 3.3a and 3.3b respectively. Both types of responses are similar for all three constitutive models up to pressure levels of about 1150 psi (79.3 bar). At higher pressures, as they become more nonlinear, the Yld04-3D response traces slightly higher pressure values. However, the main difference is in the onset of localization. In the case of H8, deformation in the imperfection localizes in a similar manner as for Yld04-3D but at a higher volume and slightly lower pressure (1337 psi—92.2 bar). By contrast, the 1% thickness imperfection constitutes too small of a disturbance for the vM model and it does not localize; it does so for higher values of Δt when localization is delayed even more than for H8. The relatively small differences between the Yld04-3D and H8 models are of course mainly caused by the fact that the material anisotropy is quite small (especially the value of r_b). The difference with the vM predictions is larger because of yield function shape differences implied by its quadratic nature.

In such calculations the pressure maximum represents the bulge burst pressure. This value is of course dependent on the amplitude of the imperfection used. Figure 3.7 shows P-u/u_o responses calculated with the Yld04-3D model for imperfections values $0 \le \Delta t/t_o \le 3\%$. In the absence of an imperfection, the response develops the natural pressure maximum at 1366.8 psi (94.26 bar). As the imperfection amplitude increases the

burst pressure decreases reaching a value of 1237.3 psi (85.33 bar) for 3% amplitude (see Table 3.1).

Table 3.1 Burst pressure for various imperfection amplitudes predicted using the idealized FE model (Yld04-3D)

D/t_o (%)	0	0.5	1.0	2.0	3.0
P_{max} psi (bar)	1366.8 (94.26)	1364.6 (94.11)	1345.9 (92.82)	1293.1 (89.18)	1237.3 (85.33)

3.3 Model that Includes the Draw Bead

3.3.1 Detailed Clamping Process

It is interesting that in the experiments discs burst consistently at somewhat higher pressures than the pressure maxima of the simulations listed in Table 3.1, which ranged between 1413-1468 psi (97.45-101.2 bar). The main cause of this difference is the fixed boundary condition imposed to the edge of the disc in the idealized FE model adopted thus far (see Fig. 3.2). In the experiments, the disc is pressed over the draw bead by the clamping ring. It was observed that this condition allowed the edge of the disc to slide a small amount over the draw bead thus feeding material into the bulging section. To investigate the influence of this effect on the solution, the FE model was expanded to include the draw bead and the mating groove in the clamping ring.

A cross section of the expanded version of the model and the disc mesh is shown in Fig. 3.8a. It represents quite accurately the geometry of the experimental setup (see Fig. 3.1). The main part of the disc mesh remains nearly the same but the annulus beyond the draw bead is added to it. It follows the same angular distribution of elements as that given in Section 3.1, but has a finer radial distribution in the neighborhood of the draw bead as depicted in the figure. The base of the model, the draw bead and the clamping ring are

modeled as analytical rigid surfaces. The same surface-to-surface contact algorithm with finite sliding is adopted but now contact is frictional with Coulomb friction coefficient μ.

An additional step that mimics the clamping process used in the experiment is added to this model. The initial configuration of the model is shown in Fig. 3.8a. Clamping involves incrementally displacing the clamping ring downwards while keeping the volume in the cavity constant. In the process, the disc locally conforms to the shape of the draw bead and the mating groove in the clamping ring while the pressure under the disc increases. When the clamping ring reaches a predetermined position relative to the base, the two rigid surfaces are fixed in space. Figure 3.8b shows a cross sectional view of the deformation induced by clamping in the neighborhood of the draw bead. Furthermore, the deformation has resulted in significant straining of the arch formed at the crest of the bead. It is worth mentioning that the design of the experiments involved variation of the shape of the groove and the extent of clamping in order to minimize this strain to avoid premature failure at this location.

3.3.2 Structural Responses

After clamping, the disc is pressurized by prescribing incrementally the fluid flux into the cavity below the disc. Results from simulations using the new model for the same disc analyzed earlier are now used to illustrate the difference. The solution exhibits essentially the same imperfection sensitivity as before, so $\Delta = 0.01 t_o$ is chosen for this demonstration. As will be shown below, the new solution is also influenced by the friction coefficient adopted, so the value of $\mu = 0.3$ is used here. Calculated $P - h/R$ and $P - u/u_o$ responses from the "draw bead" model (DB) are compared to corresponding ones from the idealized model with fixed edge (FXE) in Figs. 3.9a and 3.9b respectively. The initial parts of the DB responses are somewhat different from the FXE one due to the clamping; it

causes an abrupt increase in pressure and a more direct increase in the height. Subsequently the two pressure-height responses rise with approximately the same slope up to a pressure of about 1000 psi (69 bar), and the same can be said about the pressure-volume responses. However, the DB responses exhibit a higher pressure maximum, larger corresponding volume, and rise to a slightly greater height. As a consequence of the sliding allowed by the draw bead, the DB model reached $P_{\max}$ = 1405.2 psi (96.91 bar), which compares with 1345.9 psi (92.82 bar) for the FXE model. As a reference point the pressure maxima for the DB and FXE models in the absence of an imperfection were 1414.8 psi (97.57 bar) and 1366.8 psi (94.26 bar) respectively. Following the pressure maximum deformation localizes in a similar manner to that described for the FXE model in Figs. 3.5. The extent of sliding that took place is demonstrated in the cross sectional view of the deformed disc corresponding to $P_{\max}$ shown in Fig. 3.8c.

As mentioned earlier, in the experiments the discs burst at pressures that ranged from 1413 to 1468 psi (97.45-101.2 bar). Included in Fig. 3.9a with a dashed line is the pressure-height response measured in an experiment that burst at 1413 psi (97.45 bar). The response follows essentially the same trajectory as the DB response, exhibiting a slightly stiffer trajectory close to burst.

The increase in $P_{\max}$ yielded by the DB model depends on the friction coefficient adopted. This is demonstrated in Fig. 3.10a in which pressure-height responses for Coulomb friction coefficients of 0.2, 0.3 and 0.4 are compared for $D/t_o = 1\%$. The values of $P_{\max}$ achieved in each case are listed in Table 3.2. Figure 3.10b shows plots of the pressure vs. the amount of edge sliding, s, normalized by the disc initial thickness t_o, for the three cases. Following an initial transient caused by the clamping process, the value of s increases monotonically but tends to saturate as the maximum pressure is approached. As μ decreases the amount of material that feeds into the bulging domain increases. This

reduces somewhat the stiffness of the P- h/R response, and increases the maximum pressure reached. It is interesting to observe that for $\mu = 0.4$ the amount of sliding that takes place after clamping is minimal, and as a result the pressure maximum is close to that yielded by the FXE model.

Table 3.2 Predicted burst pressures using the draw bead model for various Coulomb friction coefficients

μ	0.2	0.3	0.4	FXE
$P_{\max}$ psi (bar)	1474.1 (101.7)	1405.2 (96.91)	1350.4 (93.13)	1345.9 (92.82)
$s_{\max}/t_o$	4.26	2.33	0.93	0

3.3.3 Localized Deformation in Bulge Test

Al-2014-T3 is a structural material with relatively high yield stress and modest ductility. By contrast Al-6022-T43 is aimed at manufacturing and consequently has a lower yield stress, exhibits significant hardening and is much more ductile. Consequently in the bulge test on the latter material reported in Chen et al. [2018a], the pressure reached a maximum and concurrently deformation localized around the apex This section investigates the localization behavior through numerical simulation.

The main characteristics of the solution are illustrated through the results of a simulation that uses the calibrated Yld04-3D constitutive model reported in Section 2.3.1. Figure 3.11a shows the calculated pressure-height (P- h/R) response. The model has no imperfection and a Coulomb coefficient of 0.4 is adopted. The calculated response tracks that of the experiment very closely from the beginning to the end, and the latter is not included in this figure for clarity. A pressure maximum develops at 933.05 psi (64.35 bar), which compares with 932.8 psi (64.26 bar) recorded in the experiment. The analysis does

not employ a failure criterion so the response is followed further than in the experiment well past the pressure maximum. The evolution of the bulge profile is illustrated in Fig. 3.11b, which shows the complete shape of a meridian at the pressure and height values marked with numbered bullets on the response in Fig. 3.11a ($r \equiv$ radial distance measured from the bulge center). Profile ⑦ corresponds to the pressure maximum. As in the experiments, the bulge profiles exhibit a progressive increase in curvature with height and a reduction of the rate of increase as the bulge height increases. Furthermore, as in the experiment, the shape of the bulge remains continuous past the pressure maximum and the apex maintains its nearly circular shape.

Figure 3.11c shows the equivalent plastic strain (e_e^P) that develops in the same ten configurations, with profile ⑦ once more corresponding to the pressure maximum. In contrast to the bulge profiles, the strain profiles exhibit an increasingly tighter radius around the apex, which becomes significantly more pronounced after the pressure maximum. Thus in profiles ⑧-⑩, the zone around the apex becomes increasingly more conical indicating an acceleration of wall thinning. Simultaneously, the strain decreases nearly linearly with r moving away from the apex. These features are once again very similar to those of the experimental profiles in Fig. 3c of Chen et al. [2018a]. Figure 3.11d compares the strain at the apex with that developed at $r = 0.65R$. At lower values of bulge height the two strains grow at a similar rate gradually diverging. For $h > 0.4R$ when the pressure-height response starts to become nonlinear, the strains continue to grow at both locations but the trajectories increasingly diverge. Beyond the limit load (marked with solid bullets) the rate of growth of strain at the outer location where the bulge profile is becoming straighter, starts to decrease. By contrast, the strain at the apex grows at an even faster rate. This divergence in the rate of growth of strains is reminiscent of diffuse localized

deformation such as a neck in a tensile test. However, in the present problem the pre-limit load stresses and deformations at the two locations are different.

3.3.4 Effect of Slipping on Localization

The solutions presented above were generated with a Coulomb friction coefficient $m = 0.4$. In Section 3.3.2 we pointed out that slipping over the draw bead can affect the calculated response. The amount of slipping is governed by the extent of mechanical clamping and by friction. As shown in Fig. 3.8, the imposed displacement of the clamping ring was chosen to be as large as possible without causing failure of the disc at the draw bead. This process does not preclude some small amount of slipping at the draw bead. Consequently it is important that the effect of slipping on the localization behavior be evaluated. To this end, the bulge test simulation is repeated using the Yld04-3D constitutive model and Coulomb friction coefficients of 0.3, 0.4 and 0.5 and a thickness imperfection of $D / t_o = 0.25\%$. The calculated pressure-bulge height responses are shown in Fig. 3.12a. The magnitude of inward sliding of the outer edge, *s*, normalized by t_o, is plotted against the pressure in Fig. 3.12b. Clearly, increase in friction lowers the limit pressure and causes it to occur at a smaller bulge height.

The extra feed of material into the bulging domain allowed by sliding is responsible for the larger height reached for lower μ values, and for the increase in $P_{\max}$ observed in Fig. 3.12a and quantified in Table 3.3 below. At the same time however, it is noteworthy that the strain at the apex achieved at the pressure maximum decreases as the pressure and corresponding bulge height increase, as the values reported in the same Table indicate. (This result can also be demonstrated analytically using an extension of Hill's analysis of the critical strain–Appendix A.)

Table 3.3 Effect of friction on limit pressure and strain

μ	0.3	0.4	0.5
$P_{\max}$	958.5	935.2	922.6
e_e^p	0.53	0.56	0.57

Since most bulge testing facilities used in materials labs are relatively compliant, the bulge is expected to fail at the pressure maximum or soon thereafter. Clearly then, it can be concluded that better clamping can have the beneficial effect of increased strain measured in a bulge experiment. In the present simulations, the response for $\mu = 0.4$ was closest to the experimental response so this friction coefficient was adopted in the parametric study performed.

It should be mentioned that in the simulations presented sliding is axisymmetric and uniform. In practice, non-uniform, asymmetric slipping may take place as illustrated by the failed specimen shown in Appendix B from a previous study. Slipping can influence the state of stress and strain at the apex and, by extension, the extracted stress-strain response. In general then, every effort should be made to reduce slipping in bulge tests, as recommended in ISO [2014].

Finally, to assess the effect of the stress-strain response adopted on the numerical simulation of the bulge test, the FE model was used to calculate the bulge response using the Swift and Voce extrapolations of the uniaxial response along the rolling direction shown in Fig. 2.11. Figure 3.13 compares the pressure-height responses calculated using these two stress-strain responses with that produced using the stress-strain response extracted from the bulge test. Here the H8 constitutive model is adopted for all three cases. As can be seen from Fig. 3.13, the H8 prediction using the stress-strain response extracted from the bulge test is very close to the experimental one. As expected, the response

produced by the Swift extrapolation overestimates the experimental response and the Voce underestimates it, pointing to the inadequacies of such extrapolations.

3.4 SUMMARY AND CONCLUSIONS

A fully 3-D model with solid elements is used to simulate the bulge test and the onset of failure. The model incorporates the calibrated isotropic and anisotropic yield functions and the corresponding stress-strain responses extracted. The calculated results reproduce the experimental measurements very closely, including the pressure-height response, the pressure maximum, and the deformed strain profile and its evolution into a more conical shape after the pressure. Since the anisotropy in the sheets tested was small, the limit pressure is influenced only modestly by anisotropy and more significantly by the adoption of yield function with exponent 8. A small wall thickness imperfection in the spirit of Marciniak and Kuczynski is introduced at the apex in order to trigger localization. It leads to a sharp pressure maximum followed by precipitous localization in the zone of the imperfection. In the case of the anisotropic yield function the pressure maximum is shown to be sensitive to the orientation of the imperfection. As expected, it is also strongly dependent on the amplitude of the imperfection adopted.

In the bulge tester the edge of the disc is clamped over a draw bead. It was found that the clamping applied allowed a small amount of sliding over the draw bead during the experiments thus feeding material into the deforming bulge. The FE model was extended to include the draw bead and frictional contact with the clamped disc. Using this model it was demonstrated that sliding over the draw bead delays burst and increases the corresponding burst pressure. However, it causes a decrease in the strain at the pressure maximum.

Adoption of Swift and Voce extrapolations in the FE simulation of the bulge test resulted in significant deviations from the measured results. The reported differences are of paramount importance in forming simulations, and especially in calculations of FLDs, as well as in other calculations involving large deformations.

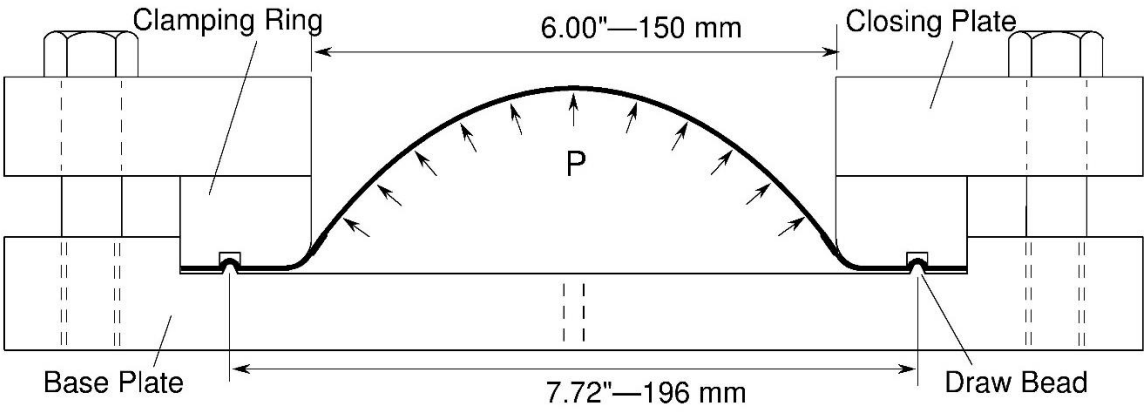

Fig. 3.1 Schematic of hydraulic bulge testing device (Chen et al., 2016).

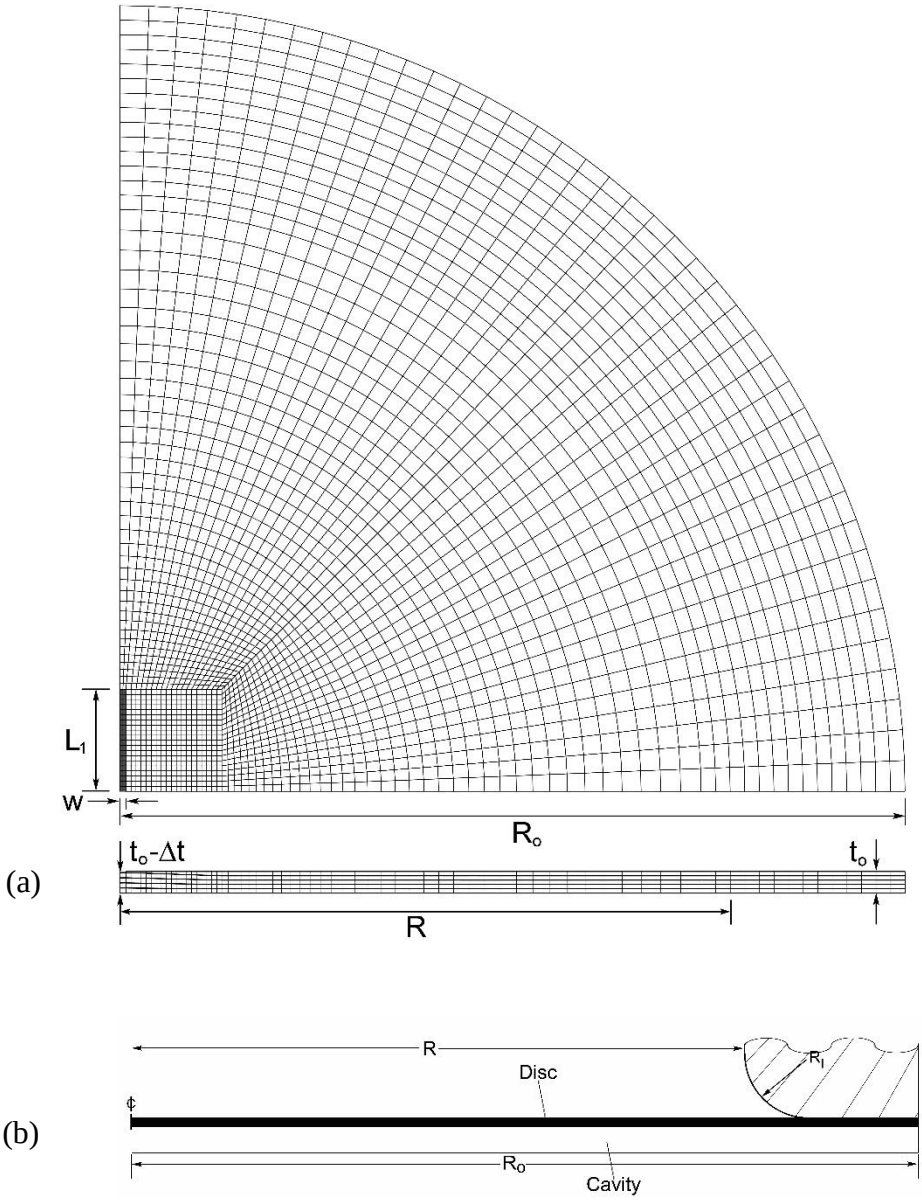

Fig. 3.2 (a) One quarter of the idealized finite element model of the bulge test and (b) cross-section of the finite element model showing the disk, cavity, and clamping ring

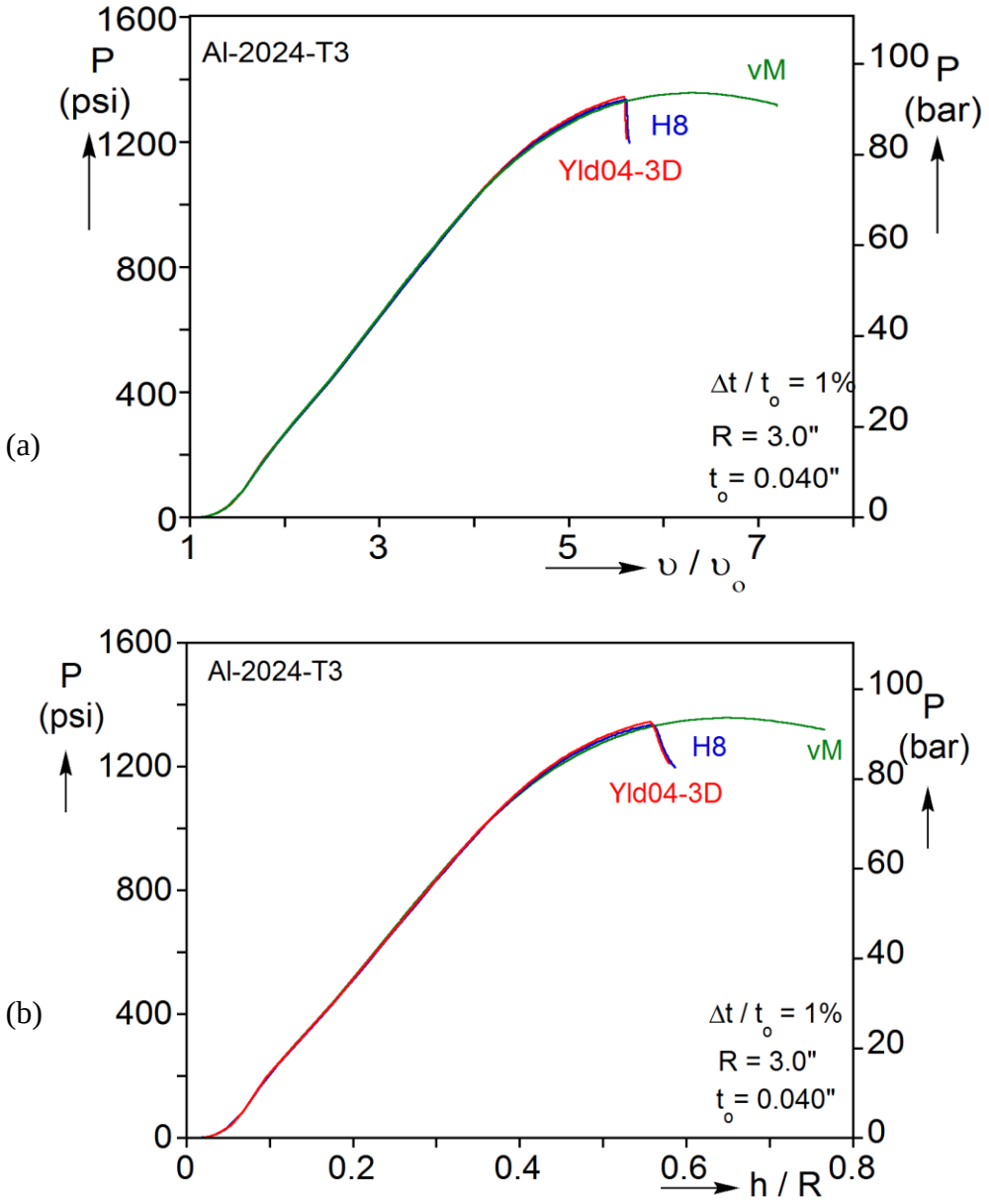

Fig. 3.3 Idealized FE model results using three different constitutive models: (a) pressure vs. normalized volume and (b) pressure vs. normalized height responses.

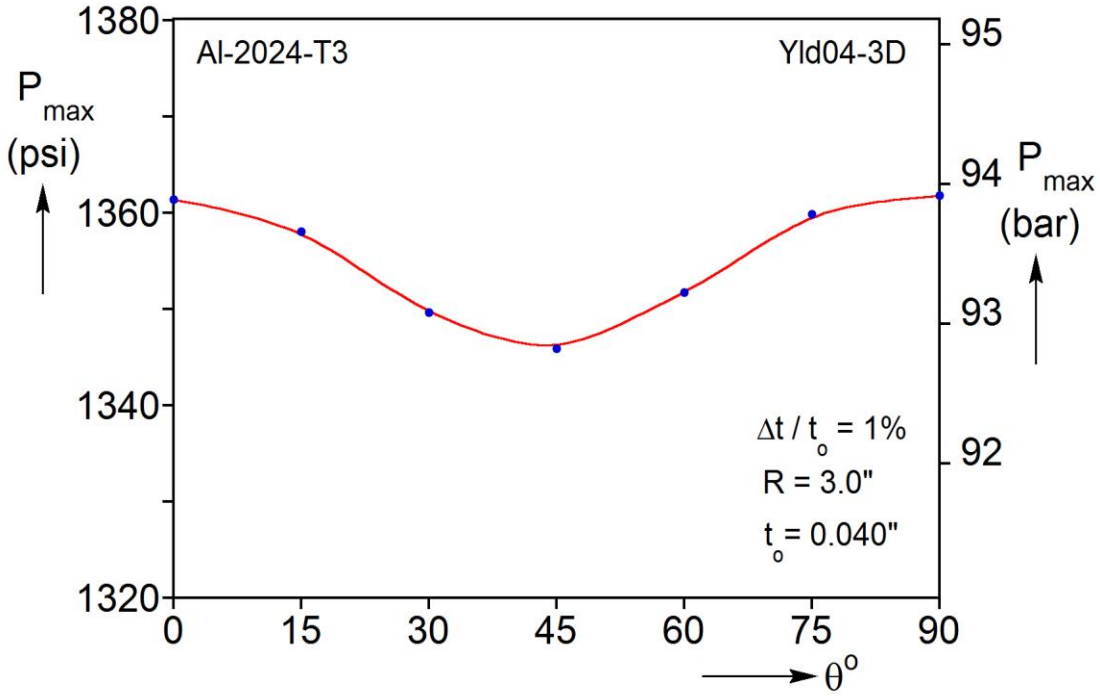

Fig. 3.4 Calculated pressure maximum for seven different imperfection orientations (Yld04-3D).

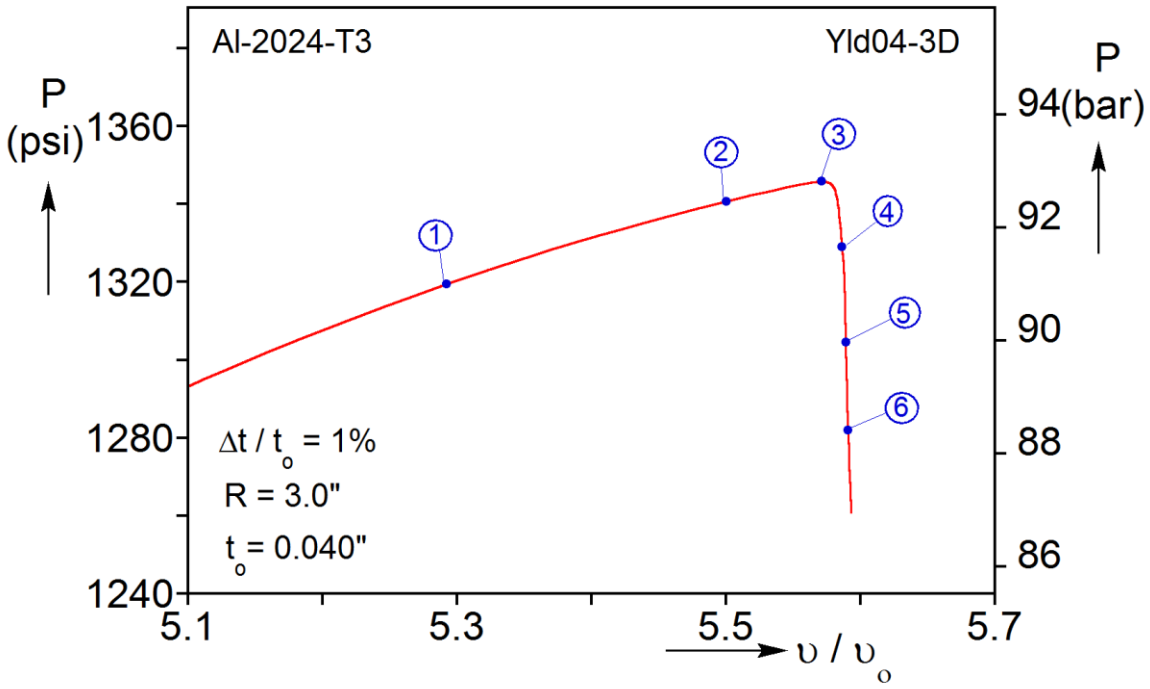

Fig. 3.5a Close-up view of the pressure-volume response near the pressure maximum (Yld04-3D).

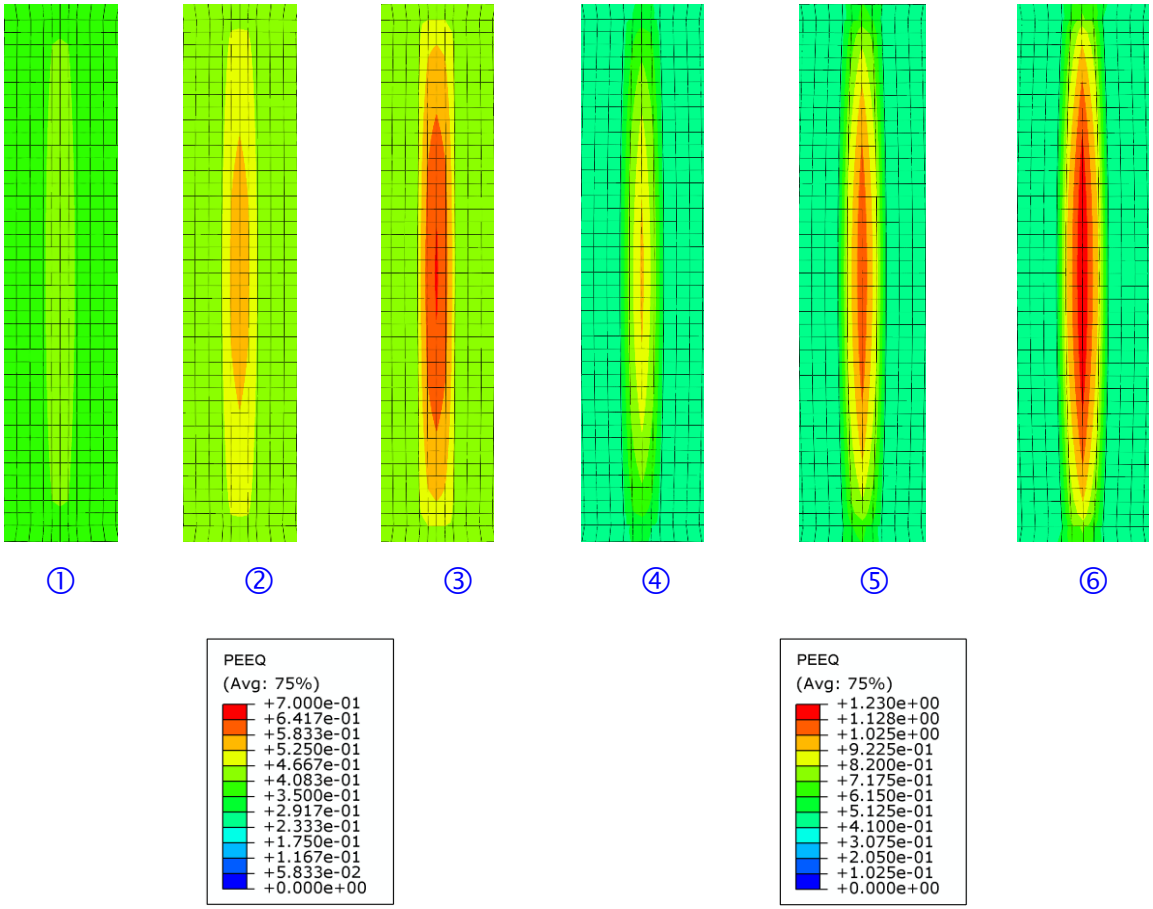

Fig. 3.5b Deformed configurations of the imperfection zone corresponding to the numbered bullets on the response in Fig. 3.5a with color contours of equivalent plastic strain superimposed (images ①-③ and ④-⑥ have different color scales).

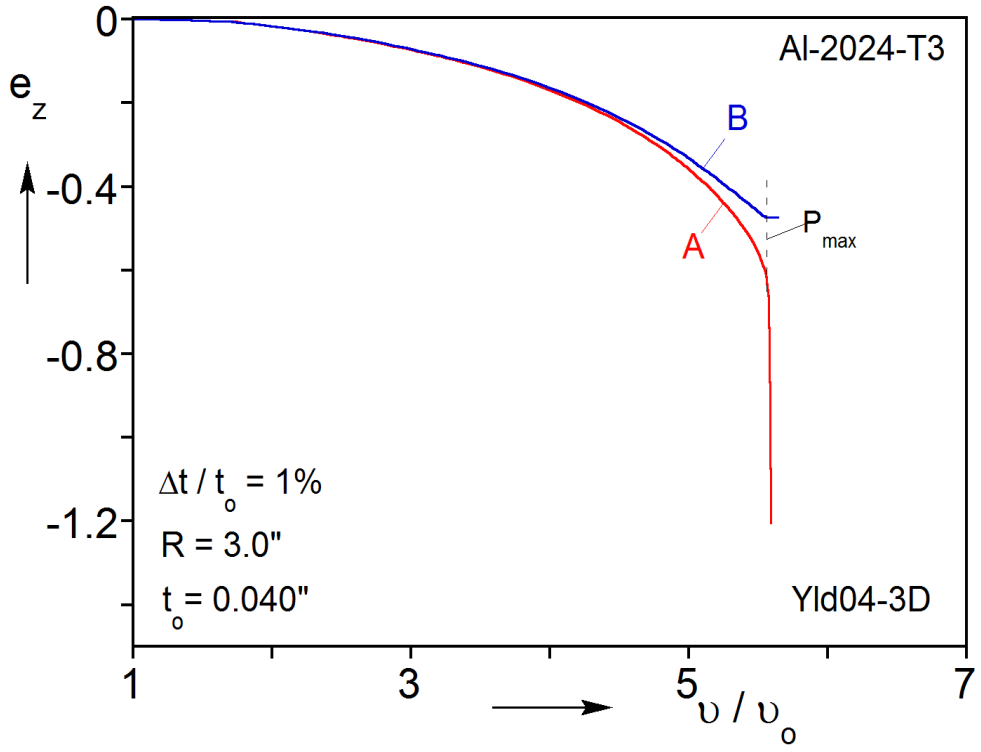

Fig. 3.6 Through-thickness strain at the apex vs. volume: A corresponds to an element inside the imperfection and B to one just outside it.

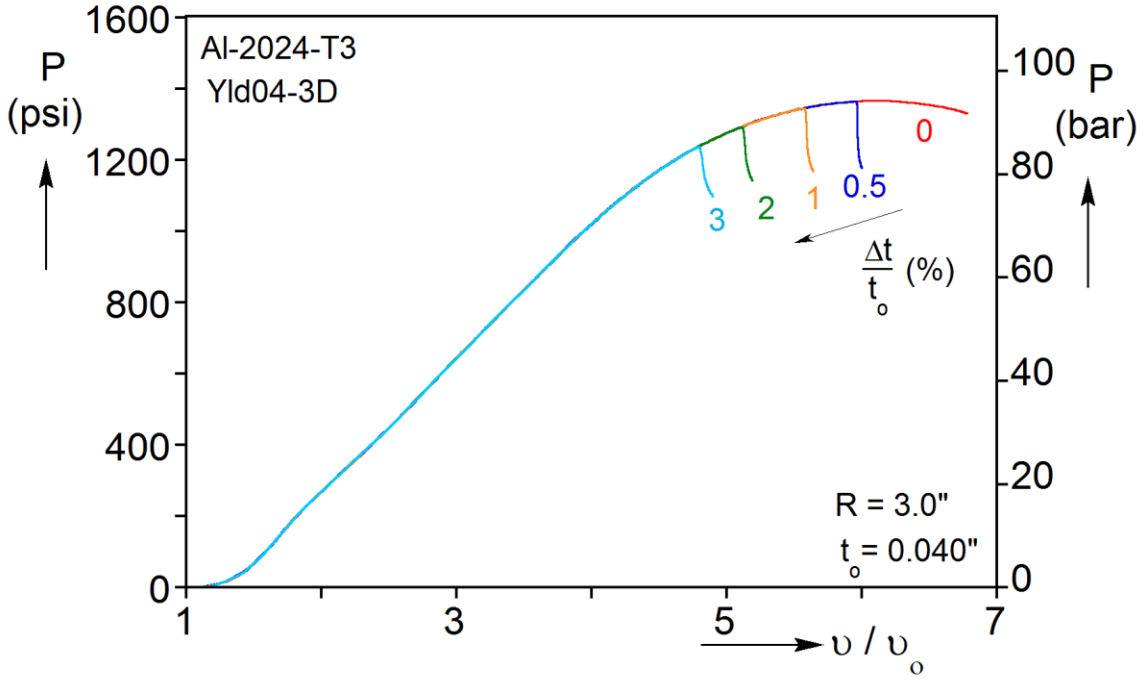

Fig. 3.7 Pressure vs. normalized volume responses for different imperfection values (Yld04-3D).

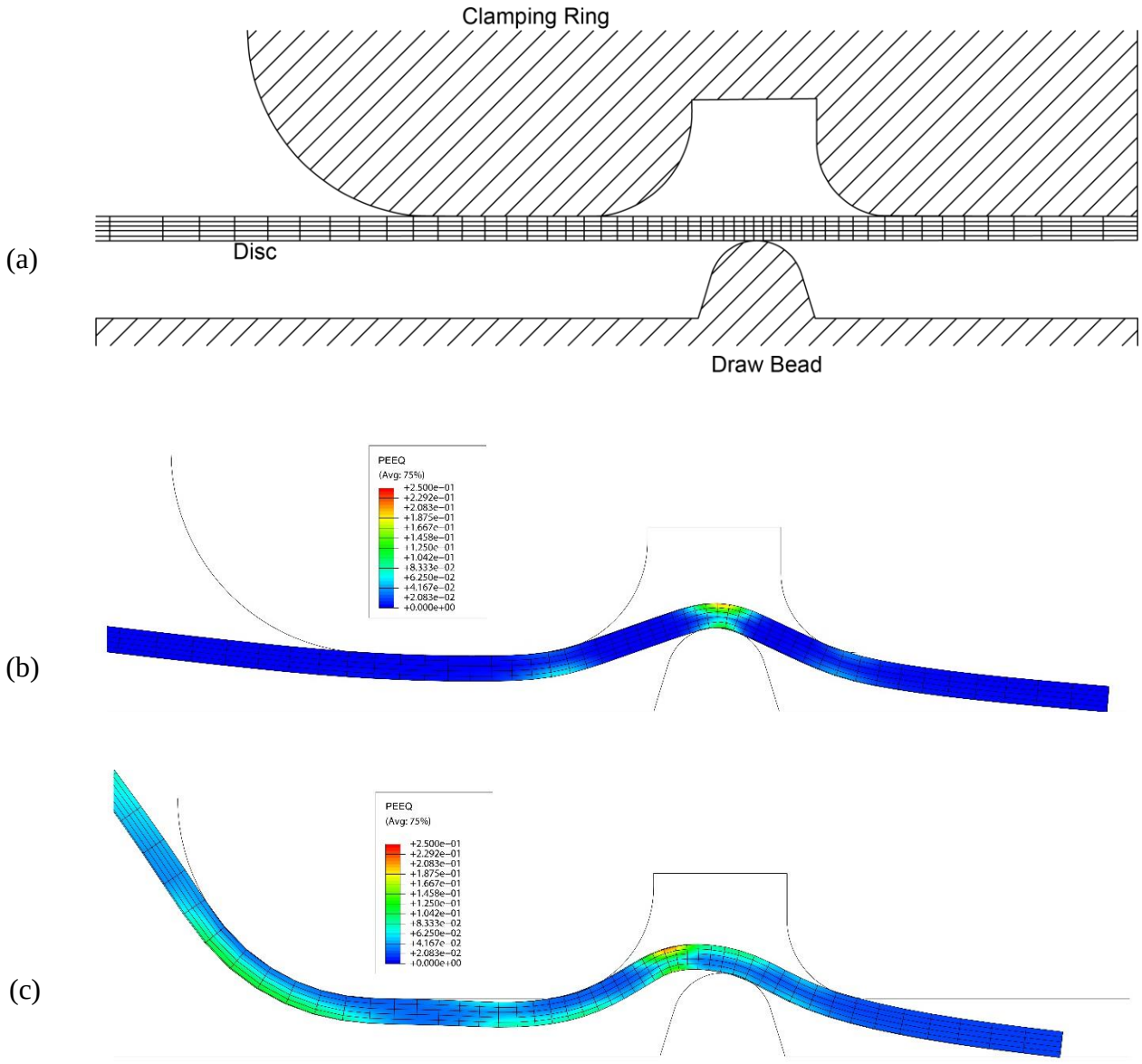

Fig. 3.8 Cross-sectional views of the FE model that includes the draw bead: (a) Undeformed geometry and disc mesh. (b) Deformed configuration with equivalent plastic strain color contours after clamping. (c) Deformed configuration with equivalent plastic strain color contours at the pressure maximum.

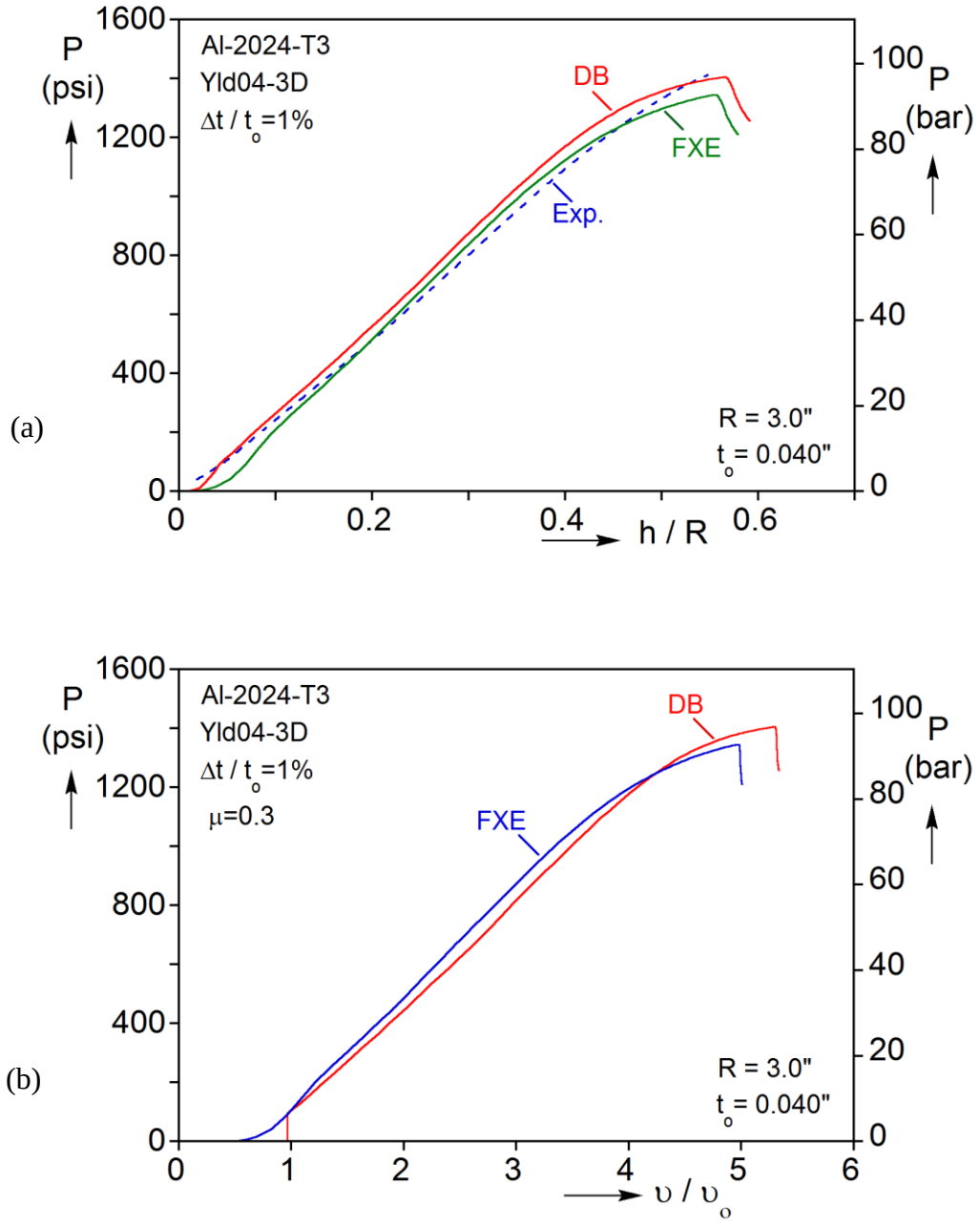

Fig. 3.9 (a) Pressure vs. normalized height responses from the FE model with fixed edge (FXE), the FE model with the draw bead (DB), and from an experiment (Exp.). (b) Pressure vs. normalized volume responses of the two finite element models.

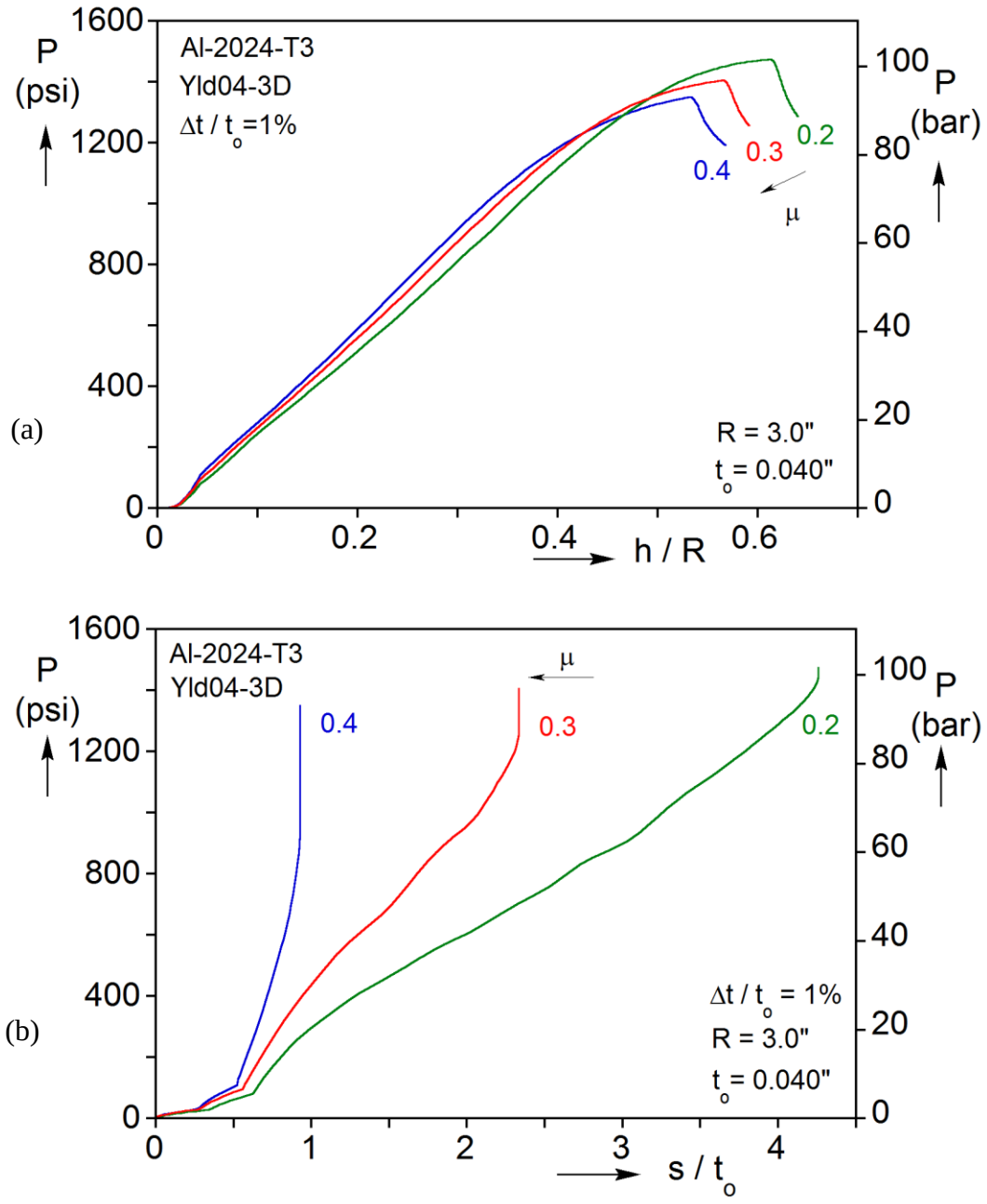

Fig. 3.10 (a) Pressure vs. normalized height for the DB model for different friction values. (b) Pressure vs. normalized disc edge displacement for three friction values.

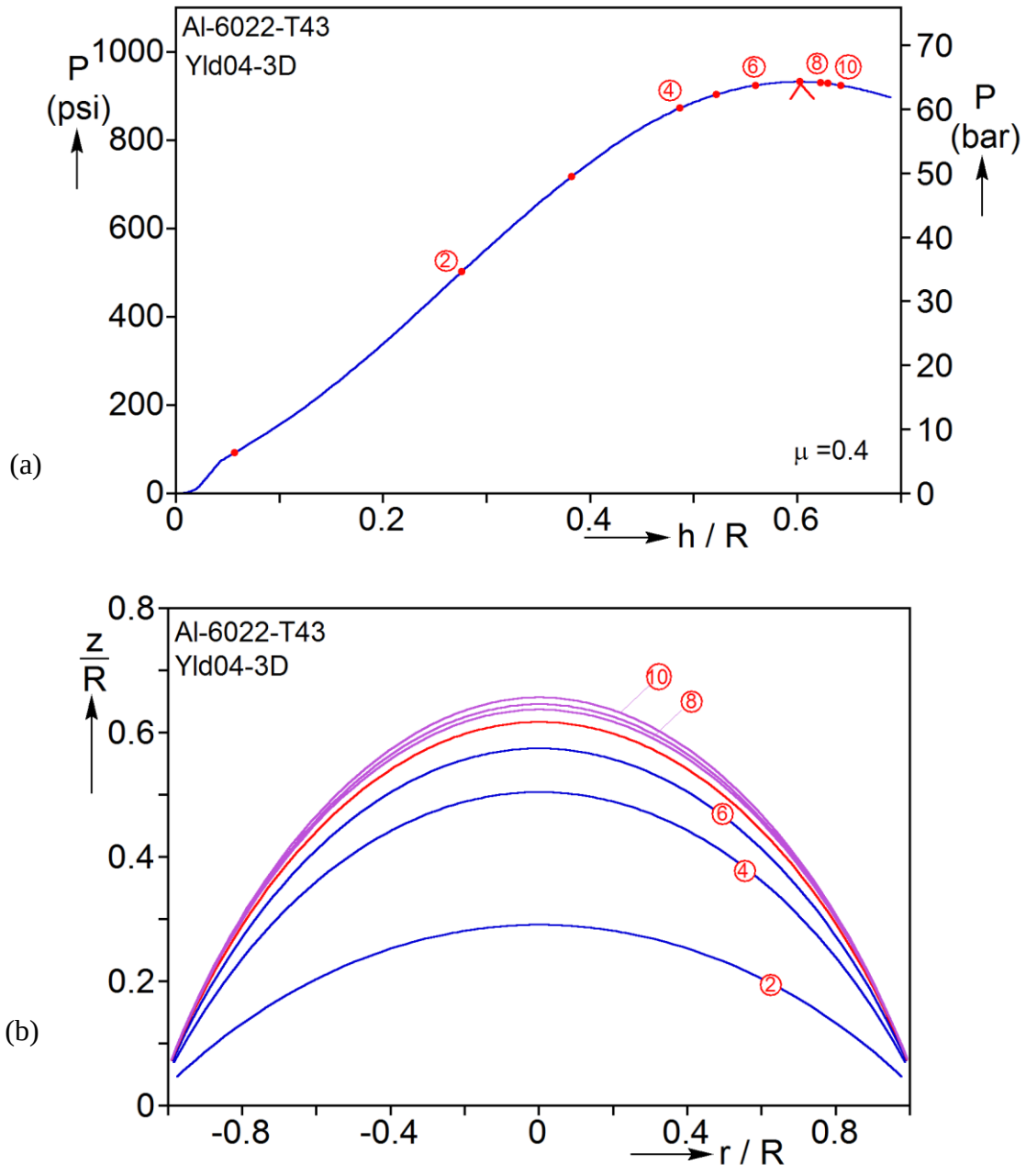

Fig. 3.11 Evolution of deformation in finite element simulation: (a) Pressure vs. height response and (b) deformed surface profiles

(c)

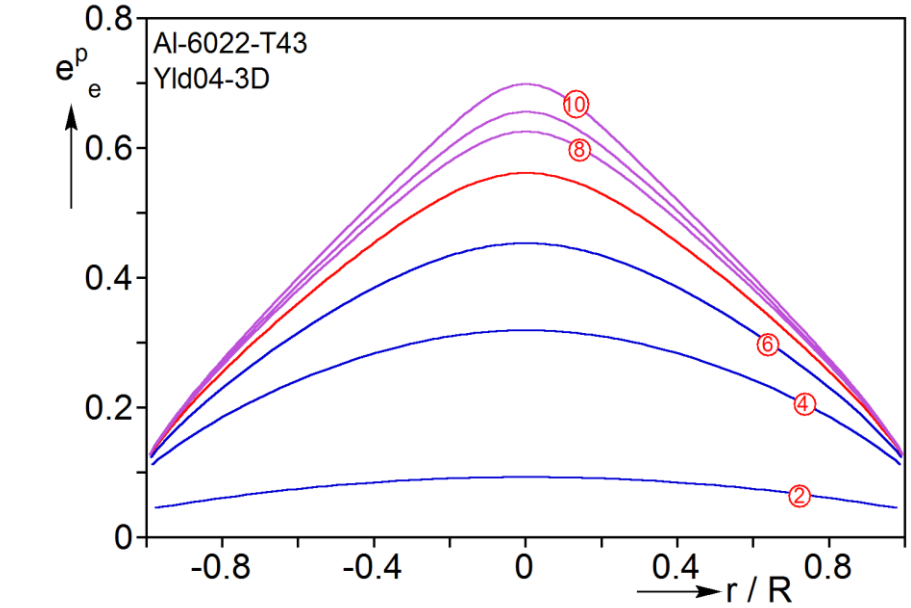

(d)

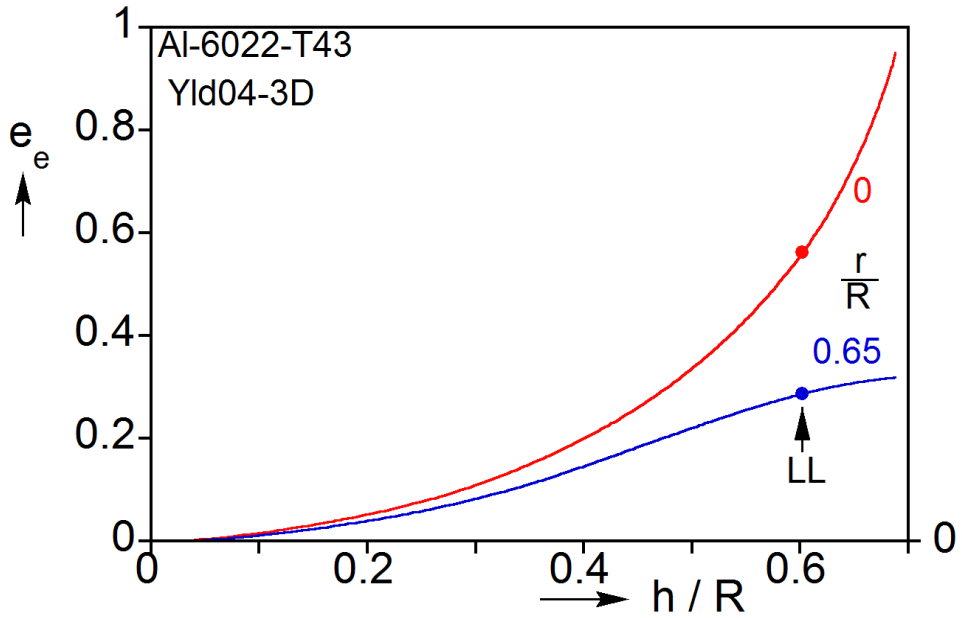

Fig. 3.11 (c) Evolution of corresponding equivalent strain profiles. (d) Evolution of equivalent plastic strain at the apex $(r = 0)$ and at a point a radial distance of $0.65R$ from the apex (location of pressure maximum denoted by LL).

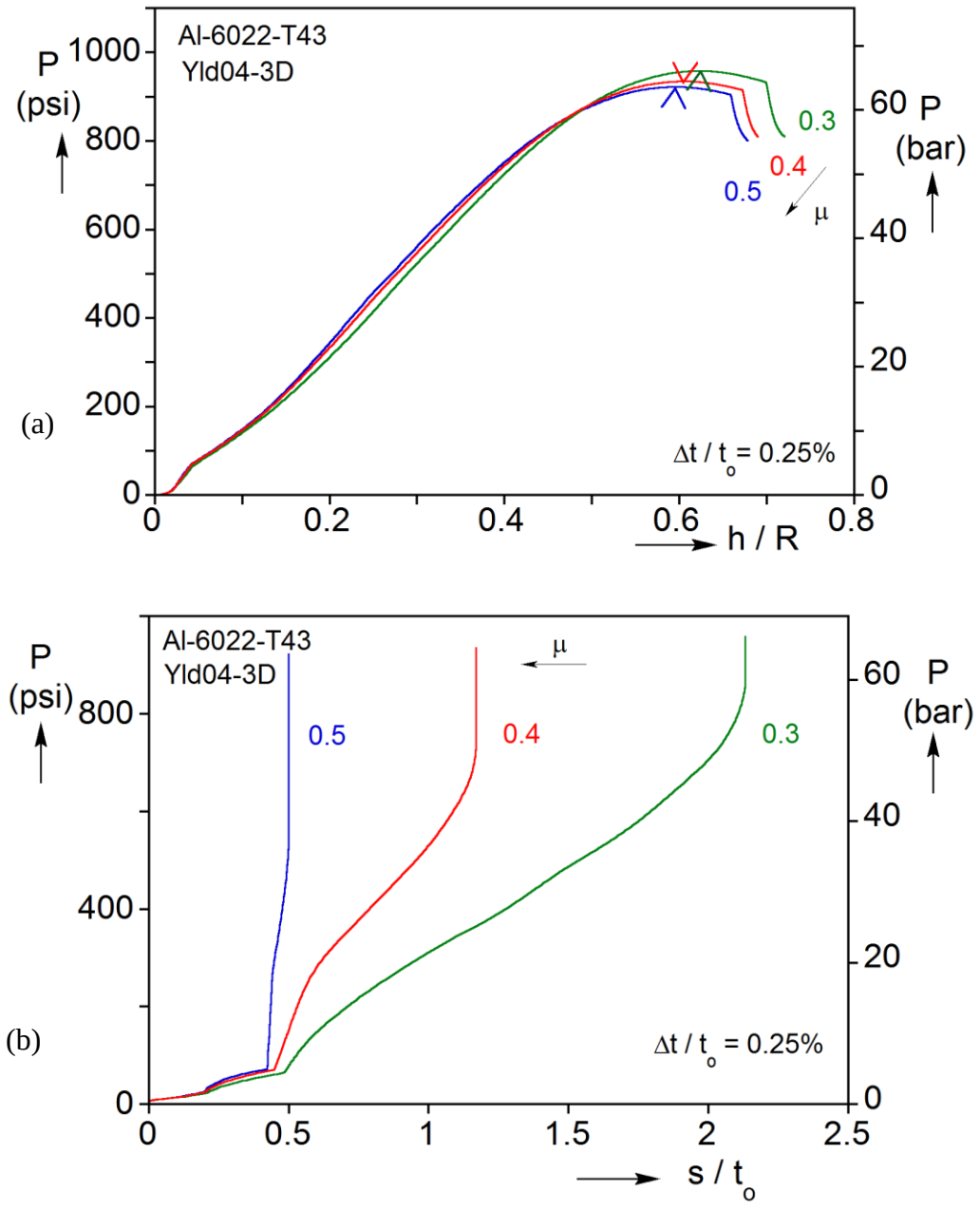

Fig. 3.12 Effect of friction coefficient on (a) Predicted pressure vs. height response, and (b) magnitude of radial displacement of the disc boundary.

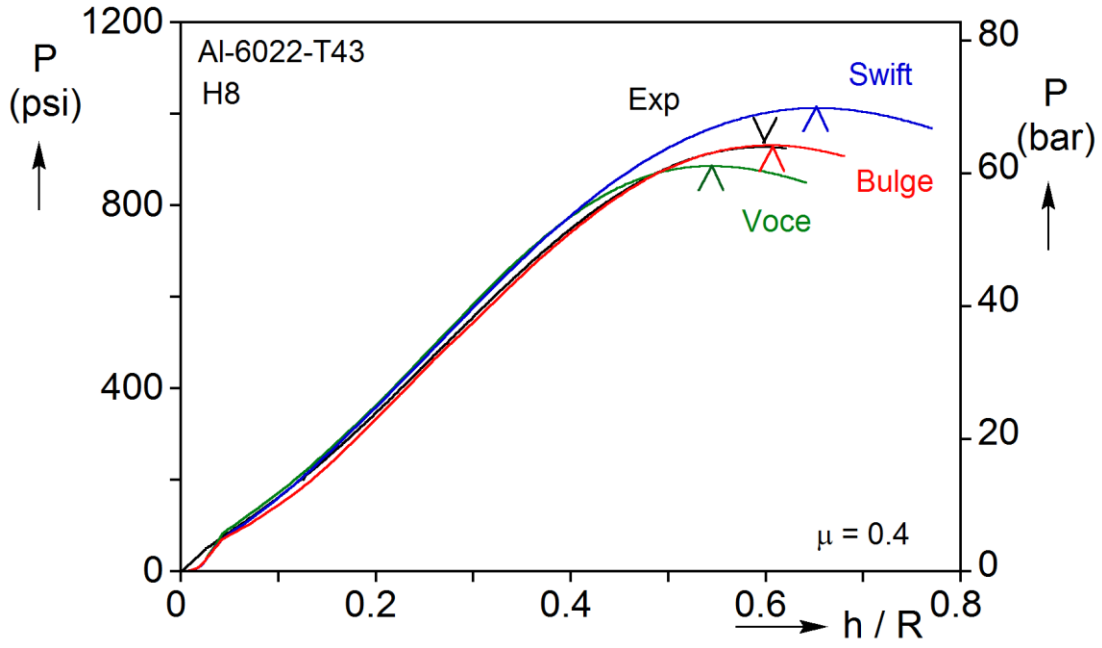

Fig. 3.13 Predicted pressure vs. height responses using the different stress-strain curves shown in Fig. 2.12. The measured experimental response is included.

Chapter 4: Constitutive Modeling of Tubular Specimen under Tension and Torsion[5]

4.1 INTRODUCTION

Scales et al. [2019] describes in detail the conduct and the results of a set of tension-torsion experiments on custom Al-6061-T6 thin-walled tubes used to establish the failure strain in the moderate to low triaxiality regime. The specimen design and the stiff test setup enabled localization in the form of diffuse necking to develop free of constrains until rupture occurred in the deepest part of the neck. High resolution DIC enabled continuous monitoring of the strain in the test section including the necked zone. The strains measured in the failure zone follow the classical trend of monotonic decrease with increasing triaxiality, but their values are significantly larger than previously reported ones. Both of these findings are in agreement with similar results in Scales et al. [2016]. The failure surfaces were found to have the usual dimpled relief suggestive of ductile failure by void growth and coalescence. X-ray tomography and microscopic observations (e.g., Ghahremaninezhed and Ravi-Chandar, 2012, 2013; Haltom et al., 2013) found that this alloy had very small initial porosity and very limited pore growth away from the failure zone; it was further concluded that in the failure zone void growth and coalescence occurred very close to the end of life of the material.

Collectively these results prompt the modeling effort, reported in Chapters 4 and 5, that aims to establish the extent to which plasticity can reproduce the measured responses and the evolution of localization without the introduction of damage. To this end this chapter presents the constitutive modeling of the anisotropic material which consists of:

[5] Chen, K., Scales, M., Kyriakides, S. (2019). Material response, localization and failure of an Aluminum alloy under combined shear and tension: Part II Analysis. *Int'l J. Plasticity* **120**, 361-379. (Chen conducted the analysis, numerical simulations and helped write the paper)

(a) the calibration of the anisotropic yield function of Barlat et al. [2005] Yld04-3D based on the tension-torsion and pressure-tension results in Scales et al. [2019], and (b) the extraction of the material hardening response from a simple shear test using the calibrated Yld04-3D constitutive model as well as quadratic and non-quadratic isotropic yield functions. Chapter 5 uses the calibrated constitutive models and material hardening to simulate the tension torsion experiments including the stress-deformation responses, and the onset and evolution of localization.

4.2 CONSTITUTIVE MODELS AND CALIBRATION

It is now well established that the constitutive model used in the analysis of forming and other large deformation processes can influence the prediction of localization and failure in thin-walled structures. The use of more advanced non-quadratic yield functions that can account for prevailing anisotropies are thus preferred in modern studies and practices. Thus the main model adopted in this study is Barlat et al. [2005] Yld04-3D (see other uses Korkolis and Kyriakides, 2008b, 2009; Korkolis et al. 2010; Giagmouris et al., 2010; Tian et al., 2017; Chen et al. 2016, 2018a; Dick and Yoon, 2018; Gorji and Mohr, 2018; Lee et al., 2018; Ha et al., 2018). For comparison, isotropic plasticity is modeled through Hosford's [1972] non-quadratic yield function, which in terms of the principal values of the stress deviator is given by:

$$F = [(|s_1 - s_2|^k + |s_2 - s_3|^k + |s_3 - s_1|^k)/2]^{1/k}. \qquad (4.1)$$

For completeness the von Mises quadratic yield function, i.e., $k = 2$ in (4.1), will also be used to simulate the tension-torsion experiments.

Barlat et al. [2005] introduce orthotropic anisotropy into (4.1) through two linear transformations to construct the tensors $\boldsymbol{S}'$ and $\boldsymbol{S}''$ from the Cauchy stress as follows:

$$\boldsymbol{S}' = \boldsymbol{C}'\boldsymbol{s} = \boldsymbol{C}'\boldsymbol{T}\boldsymbol{\sigma} = \boldsymbol{L}'\boldsymbol{\sigma} \text{ and } \boldsymbol{S}'' = \boldsymbol{C}''\boldsymbol{s} = \boldsymbol{C}''\boldsymbol{T}\boldsymbol{\sigma} = \boldsymbol{L}''\boldsymbol{\sigma} \qquad (4.2)$$

where $\boldsymbol{C}', \boldsymbol{C}'', \boldsymbol{T}, \boldsymbol{L}', \boldsymbol{L}''$ are transformation tensors. $\boldsymbol{T}$ transforms $\boldsymbol{\sigma}$ to $\boldsymbol{s}$ and $\boldsymbol{C}', \boldsymbol{C}''$ contain anisotropy parameters as shown in (2.11).
The yield function in terms of the principal values of $\boldsymbol{S}'$ and $\boldsymbol{S}''$ is then expressed as:

$$\bar{\sigma} = [(|S'_1 - S''_1|^k + |S'_1 - S''_2|^k + |S'_1 - S''_3|^k + |S'_2 - S''_1|^k + |S'_2 - S''_2|^k + |S'_2 - S''_3|^k + |S'_3 - S''_1|^k + |S'_3 - S''_2|^k + |S'_3 - S''_3|^k)/4]^{1/k} \quad (4.3)$$

where again k is assigned the value 8 (Logan and Hosford, 1980). Details about the derivations and the derivatives of the yield function with respect to the stress components can be found in Barlat et al. [2005] and Yoon et al. [2006] (the model is implemented in a subroutine developed by Yoon [2011]).

4.2.1 Characterization of Anisotropy

Calibration of anisotropy requires results from different material orientations. Although such procedures have been developed for sheet metals (Barlat et al., 2005; Yoon et al., 2006), a new procedure had to be developed for the tubes used in this study. The model is calibrated using the responses of 7 tension-torsion experiments, a "plane strain" tension test, a simple shear test, and a uniaxial tension test on an axial strip all extracted from the same batch of tubes. These were supplemented with results from the 7 tension-internal pressure radial path experiments. The state of stress and the strain ratios are evaluated for each experiment at a chosen value of plastic work ($W^p = 1000$ psi—6.897 MPa). Details of the calibration process are given below.

The calibration follows broadly the procedure in Appendix B of Barlat et al. [2005] but uses different types of experiments (see also the calibrations in Tardif and Kyriakides [2012], Chen et al. [2016]). Through-thickness shear measurements are not available thus the anisotropy constants $\{c'_{44}, c'_{55}, c''_{44}, c''_{55}\}$ in Eq. (4.2) are assigned the value 1.0. The rest of the constants are determined by minimizing the error function that is developed below.

The test sections in the experiments are assumed to be under plane stress represented by the vector:

$$\boldsymbol{\sigma} = (\sigma_{11}, \sigma_{22}, \sigma_{12})^T, \tag{4.4}$$

where the subscripts "1" and "2" represent the hoop and axial directions of the tubes, respectively.

(i) Uniaxial Tension Test

A dogbone uniaxial tension specimen was extracted from the axial direction of a tube from the same batch as the rest of the experiments. The specimen is 0.100 in (2.54 mm) thick, 0.365 in (9.27 mm) wide and has a 3-inch long (76 mm) gage section. The tensile test was carried out under quasi-static displacement control. The strain field was monitored using 3-D DIC. The gage section reached a maximum uniform strain of around 7% at the limit load (more details can be found in Scales [2019]). The plastic work is determined from the true stress-plastic strain response as follows:

$$W^p = \int_0^{\varepsilon_{22}^w} \sigma_{22}\, d\varepsilon_{22}^p \tag{4.5}$$

where e_{22}^w is the plastic strain at the chosen value of plastic work of 1000 psi (6.897 MPa) and s_{22}^w is the corresponding stress. The uniaxial stress state is introduced in the current yield function (4.3) resulting in

$$\sigma_e = \Phi(\boldsymbol{\sigma}_u). \tag{4.6}$$

Using (4.5) the following error function is established:

$$\varepsilon_u = \left(\frac{s_e}{s_{22u}^w} - 1 \right)^2. \tag{4.7}$$

The R-value is determined by fitting linearly the measured $e_{11}^p - e_{22}^p$ data to obtain $r = -de_{11}^p / de_{22}^p$, and then

$$R_{exu} = \frac{d\varepsilon_{11}^{p}}{d\varepsilon_{33}^{p}} = \frac{r}{1-r}. \tag{4.8}$$

Use the flow rule to evaluate

$$d\varepsilon_{ij}^{p} = d\Lambda \frac{\partial \Phi}{\partial \sigma_{ij}} \tag{4.9}$$

at $\boldsymbol{\sigma} = (0, \sigma_{22}^{w}, 0)^{T}$ and establish the strain ratio predicted through (4.3),

$$R_{Fu} = d\varepsilon_{11}^{p} / d\varepsilon_{33}^{p}. \tag{4.10}$$

Then form the error function

$$\varepsilon_{Ru} = \left(\frac{R_{Fu}}{R_{exu}} - 1 \right)^{2}. \tag{4.11}$$

(ii) Pressure-Tension Experiments

The pressure-tension specimens from the same stock tubing as the tension-torsion specimens have a total length of 12 inches (305 mm) and feature a 4-inch long (101 mm) uniform test section with a nominal wall thickness of 0.05 in (1.27 mm) and a radius of 0.86 in (21.84 mm). The specimen was loaded under combined internal pressure and axial loading such that the nominal axial and hoop stresses remain proportional, i.e., $\Sigma_x = \eta \Sigma_\theta$ with η constant. For thin-walled tubes, the nominal stresses can be calculated directly from the internal pressure and axial force as follows:

$$S_q = \frac{PR_o}{t_o}, \; S_x = \frac{F}{2\pi R_o t_o} + \frac{PR_o}{2t_o}, \tag{4.12}$$

where P is the internal pressure, F the axial force, and R_o and t_o are the initial mean radius and thickness of the test section. Deformation was monitored using 3-D DIC (more details can be found in Scales [2019]). By assuming incompressibility, the current thickness and radius of the test section can be calculated from the measured axial and hoop strains (averaged over a zone 0.6 (axial) × 1.2 (hoop) in (15.3 × 30.6 mm) in the middle of the test section) as follows:

$$t = t_o \exp(-\varepsilon_x - \varepsilon_\theta), \tag{4.13}$$

$$R = R_o \exp(\varepsilon_\theta), \tag{4.14}$$

which were used to replace the nominal thickness and radius in Eq. (4.12) to obtain the true stresses.

Seven σ_{11} - σ_{22} radial paths were performed. Figures 4.1a-b show the extracted true stress-plastic strain responses in the hoop and axial directions, respectively. Let $(\varepsilon_{11}^w, \varepsilon_{22}^w)$ be the strains corresponding to

$$W^p = \int_0^{\varepsilon_{11}^w} \sigma_{11}\, d\varepsilon_{11}^p + \int_0^{\varepsilon_{22}^w} \sigma_{22}\, d\varepsilon_{22}^p = 1000 \text{ psi}, \tag{4.15}$$

and $(\sigma_{11}^w, \sigma_{22}^w)$ be the corresponding stresses, which are marked with symbols "▲" in Fig. 4.1. This biaxial stress is introduced in the current yield surface (4.3) to produce

$$\sigma_e = \Phi(\boldsymbol{\sigma}_{PT}), \tag{4.16}$$

where the subscript "PT" represents the pressure-tension experiments. The following error function is developed:

$$\varepsilon_{PT} = \left(\frac{\sigma_e}{\sigma_{22u}^w} - 1 \right)^2. \tag{4.17}$$

The flow rule (4.9) is used to evaluate the strain increments for $(\sigma_{11}^w, \sigma_{22}^w, 0)^T$ and develop the predicted strain ratio $R_{FPT} = d\varepsilon_{11}^p / d\varepsilon_{22}^p$, which is compared with the measured plastic strain ratio for each radial path as shown in Fig. 4.2. The following error function is then constructed:

$$\varepsilon_{RPT} = \left(\frac{R_{FPT}}{R_{\text{exp}}} - 1 \right)^2. \tag{4.18}$$

(iii) Tension-Torsion Experiments

Seven radial path tension-torsion tests were conducted on Al-6061-T6 tubes. The test section of the specimens was designed to have a 0.40-inch long (10.2 mm) uniform

section with an initial thickness of 0.038 inches (0.965 mm) and a mean radius of 0.893 in (22.68 mm). The specimens were loaded in a servo-hydraulic axial/torsional biaxial testing system up to failure while maintaining proportional ratios of the nominal axial stress (Σ) and shear stress $(\mathcal{T})$ in the test section i.e., $\Sigma = \alpha\mathcal{T}$, with α being constant (see Scales et al., 2019). For thin-walled tubes, the nominal axial and shear stresses can be calculated directly from the applied force (F) and torque (T) as follows:

$$\Sigma = \frac{F}{2\pi R_o t_o} \quad \text{and} \quad \mathcal{T} = \frac{T}{2\pi R_o^2 t_o}. \tag{4.19}$$

where R_o and t_o are the initial mean radius and wall thickness of the test section. The deformations in the test section were monitored through the use of 3-D DIC. By neglecting elastic deformation and assuming plastic incompressibility, the current thickness and radius can be obtained as:

$$t = t_o / \lambda_1 \lambda_2 \tag{4.20}$$

$$R = R_o \exp(\varepsilon_\theta), \tag{4.21}$$

where λ_1, λ_2 are the in-plane principal stretches and ε_θ is the hoop strain, all averaged over a zone 0.2 (axial) × 0.4 (hoop) in (5.1 × 10.2 mm) in the middle of the test section. The true stresses, (s_{22}, s_{12}), are then calculated by replacing the nominal thickness and radius with the current counterparts in Eq. (4.19).

The DIC measurements revealed that the radial deformation of the test section developed a small radial deflection that varied in the axial direction (see Fig. 8 in Scales et al., [2019]). Thus the hoop stress is different from the ideal plane strain condition. These differences in hoop stress and strain influence the calibration of the yield function and were introduced in the following approximate manner: The hoop-to-axial stress ratio β $(= \sigma_{11} / \sigma_{22})$ is assumed to be constant and is evaluated for each stress ratio, a, as outlined in Appendix C.

Figures 4.3a and 4.3b show respectively the extracted shear stress-plastic shear strain responses and the axial stress-plastic strain responses from the seven radial path tension-torsion experiments. Figure 4.3c shows the estimated stress in the hoop direction plotted against the measured hoop plastic strain for the same seven experiments.

These responses are then used to evaluate

$$W^p = \int_0^{\varepsilon_{11}^w} \sigma_{11}\, d\varepsilon_{11}^p + \int_0^{\varepsilon_{22}^w} \sigma_{22}\, d\varepsilon_{22}^p + 2\int_0^{\varepsilon_{12}^w} \sigma_{12}\, d\varepsilon_{12}^p = 1000 \text{ psi}, \tag{4.22}$$

where $(e_{11}^w, e_{22}^w, e_{12}^w)$ and $(s_{11}^w, s_{22}^w, s_{12}^w)$ are the corresponding strains and stresses, and are marked with symbols "▲" in Figs. 4.3. This state of stress is introduced in the current yield surface (4.3) to produce

$$\sigma_e = \Phi(\boldsymbol{\sigma}_{TT}), \tag{4.23}$$

which is then used to generate the following error function:

$$\varepsilon_{TT} = \left(\frac{s_e}{s_{22u}^w} - 1 \right)^2. \tag{4.24}$$

The flow rule (4.9) is used to evaluate the strains for $(s_{11}^w, s_{22}^w, s_{12}^w)^T$ and develop the strain ratios $R_{FTT1} = de_{11}^p / de_{22}^p$ and $R_{FTT2} = de_{12}^p / de_{22}^p$. These are compared to the measured plastic strain ratios for each of the radial paths shown in Fig. 4.4. The following error function is then formed:

$$\varepsilon_{RTT} = \left(\frac{R_{FTT1}}{R_{\exp 1}} - 1 \right)^2 + \left(\frac{R_{FTT2}}{R_{\exp 2}} - 1 \right)^2, \tag{4.25}$$

(iv) Pure Torsion Test

The simple shear test is a special case of the tension-torsion tests described above, for which the axial force was prescribed to be zero. The pure torsion specimen had a test section of the same length but a slightly thicker (0.0461 in-1.17 mm) wall thickness compared with the other tension-torsion test specimens. This was intentionally designed to

delay buckling, thus facilitating the extraction of material hardening property as will be discussed in Section 4.2.3. Similarly, deformation in the test section was monitored using 3-D DIC. The shear deformation was found to remain quite uniform and no significant axial deformation was observed. The shear stress was directly calculated adopting thin-walled assumptions for the test section.

Let e_{12}^{w} be the shear strain corresponding to the chosen value of plastic work evaluated from

$$W^{p} = 2\int_{0}^{\varepsilon_{12}^{w}} \sigma_{12}\, d\varepsilon_{12}^{p} = 1000 \text{ psi} \tag{4.26}$$

and s_{12}^{w} be the corresponding stress. This pure shear stress-state is introduced into the current yield surface (4.3) resulting in

$$\sigma_{e} = \Phi(\boldsymbol{\sigma}_{s}). \tag{4.27}$$

The following error function is then established:

$$\varepsilon_{s} = \left(\frac{s_{e}}{s_{22u}^{w}} - 1 \right)^{2}. \tag{4.28}$$

Finally, the optimal values of the anisotropy coefficients (c_{ij}', c_{ij}'') are then chosen by minimizing the following weighted sum of these error functions:

$$\varepsilon(c_{ij}', c_{ij}'') = \sum_{m} w_{m} \left(\frac{s_{eF}}{s_{22u}^{w}} - 1 \right)_{m}^{2} + \sum_{n} w_{n} \left(\frac{R_{F}}{R_{ex}} - 1 \right)_{n}^{2} \tag{4.29}$$

In (4.29) the first series represents the errors from the *m* flow stresses, the second the errors from the *n* strain ratios developed above. The variables (w_{m}, w_{n}) are weight functions that represent the confidence level assigned to each particular experiment. The minimization was performed using the routine *NMinimize* in Mathematica.

The anisotropy parameters determined from the process are listed in Table 4.2. Note that the cylindrical coordinate system used is the one defined in Fig. 4.6. It is different from the more conventional cylindrical coordinate system used in ABAQUS.

As noted by previous researchers, the results of such calibration processes are not unique. To further evaluate the present solution the calibrated yield function and some of the corresponding experimental points are compared in Fig. 4.5a (T-T ≡ Tension-Torsion, P-T ≡ Pressure-Tension). Plotted are the work contours in the σ_{11} - σ_{22} plane both normalized by the measured axial stress σ_{22u}^{w} at W^{p} = 1000 psi (6.897 MPa) for different values of normalized shear stress σ_{12}. The comparison of experimental data and the calibrated work contours is deemed as satisfactory. A work contour in the σ_{22} - σ_{12} space, important to the problem at hand, is compared to measured tension-torsion data in Fig. 4.5b. The comparison is again favorable providing additional support for the soundness of the anisotropy calibration procedure.

Table 4.2 Anisotropy parameters for Yld04-3D model

c_{12}	c_{13}	c_{21}	c_{23}	c_{31}	c_{32}	c_{44}	c_{55}	c_{66}
1.028	1.150	1.162	0.941	0.679	0.985	1.0	1.0	1.367
c_{12}	c_{13}	c_{21}	c_{23}	c_{31}	c_{32}	c_{44}	c_{55}	c_{66}
0.713	0.683	0.847	1.093	1.056	0.962	1.0	1.0	0.695

4.2.2 Extraction of the Stress-Strain Response from Simple Shear Test

The material response is commonly measured in a uniaxial tension test, which usually necks at a strain of a few percent. By contrast, simple shear tests remain free of instabilities to large strains and thus offer an attractive alternative. Since the present study involved tension-torsion of tubes, it was convenient to extract the material hardening from a pure torsion experiment on a tube that originated from the same batch as those of the

biaxial specimens. Since the response is influenced by the constitutive model adopted (e.g., see Tardif and Kyriakides, 2012; Chen et al., 2018a; Kang et al., 2008), it is extracted for each of the three constitutive models considered. Furthermore, Chen et al. [2018b] showed that in the case of simple shear tests, the material axes rotate during shearing, and this must be accounted for when the material exhibits plastic anisotropy (see also Ch. XII-1 in Hill, 1950; ABAQUS, 2016). This section discusses the extraction process.

The specimen overall geometry is the same as in Fig. 1 of Scales et al. [2019], but the test section wall thickness was increased to 0.0461 in (1.17 mm) in order to delay buckling. The specimen was twisted under rotation control producing a shear strain rate of approximately 2×10^{-4} s^{-1}, while the axial load was prescribed to remain at zero.

The shear stress, τ, is calculated directly from the recorded torque using the thin-walled geometry of the test section. The deformation in the test section was monitored using DIC (see Section 2.3 of Scales et al. [2019], with the deformation gradient, $\boldsymbol{F}$, being provided directly from the ARAMIS software. The deformation in the test section was found to remain quite uniform, but $\boldsymbol{F}$ was averaged over a zone 0.2 × 0.4 in (5.1 × 10.2 mm) in the center of the test section. For the case of simple shear, $\boldsymbol{F}$ is given by

$$\boldsymbol{F} = \begin{bmatrix} 1 & \gamma & 0 \\ 0 & 1 & 0 \\ 0 & 0 & 1 \end{bmatrix}, \tag{4.30}$$

where γ is defined in Fig. 4.6. The incremental strain tensor is then given by

$$d\boldsymbol{\varepsilon} = sym(d\boldsymbol{F}\boldsymbol{F}^{-1}) = \begin{bmatrix} 0 & d\gamma/2 & 0 \\ d\gamma/2 & 0 & 0 \\ 0 & 0 & 0 \end{bmatrix}. \tag{4.31}$$

Figure 4.7 shows the shear stress-plastic shear strain (τ - γ^p) response measured in this experiment. It extends to a strain of just under 1.2 and exhibits hardening throughout.

The incremental spin tensor is given by

$$d\boldsymbol{\omega} = skewsym(d\boldsymbol{F}\boldsymbol{F}^{-1}) = \begin{bmatrix} 0 & d\gamma/2 & 0 \\ -d\gamma/2 & 0 & 0 \\ 0 & 0 & 0 \end{bmatrix}, \tag{4.32}$$

which integrates to

$$\boldsymbol{\omega} = \begin{bmatrix} 0 & \gamma/2 & 0 \\ -\gamma/2 & 0 & 0 \\ 0 & 0 & 0 \end{bmatrix}. \tag{4.33}$$

Thus, the transformation tensor for the material frame becomes

$$\boldsymbol{A} = \begin{bmatrix} \cos\gamma/2 & -\sin\gamma/2 & 0 \\ \sin\gamma/2 & \cos\gamma/2 & 0 \\ 0 & 0 & 1 \end{bmatrix}. \tag{4.34}$$

The stress, when rotated into the material frame, is then:

$$\boldsymbol{\sigma}' = \boldsymbol{A}\sigma\boldsymbol{A}^{T} = \tau\begin{bmatrix} -\sin\gamma & \cos\gamma & 0 \\ \cos\gamma & \sin\gamma & 0 \\ 0 & 0 & 1 \end{bmatrix}. \tag{4.35}$$

For the anisotropic material in Eqn. (4.3), the equivalent stress in the material frame then becomes

$$\sigma_e = \sigma_e(\sigma'_{ij}, c'_{ij}, c''_{ij}). \tag{4.36}$$

By contrast, in the reference frame it is given by

$$\sigma_e = \sigma_e(\sigma_{ij}, c'_{ij}, c''_{ij}). \tag{4.37}$$

The equivalent stress is then used to evaluate the work compatible plastic equivalent strain increment at stage *n* in the incremental process from

$$d\varepsilon_e^p\Big|_n = \left.\frac{\tau\, d\gamma^p}{\sigma_e}\right|_n. \tag{4.38}$$

The complete response is assembled by summing the increments over the whole test history. If the material yields isotropically, (4.3) reduces to the Hosford's non-quadratic

yield function (4.1) with exponent 8 (H8). This is invariant to transformation and, as a result, the simple shear test reduces to:

$$\sigma_e\big|_{\text{H8}} = (2^7+1)^{1/8}\,\tau \tag{4.39a}$$

and

$$d\varepsilon_e^p\big|_{\text{H8}} = \frac{d\gamma^p}{(2^7+1)^{1/8}}, \tag{4.39b}$$

which integrates directly.

To facilitate a comparison with a quadratic yield function, we include the equivalent stress for simple shear for von Mises (vM)

$$\sigma_e\big|_{\text{vM}} = \sqrt{3}\,\tau\,. \tag{4.40a}$$

The corresponding equivalent plastic strain increment is

$$d\varepsilon_e^p\big|_{\text{vM}} = \frac{d\gamma^p}{\sqrt{3}}, \tag{4.40b}$$

which also integrates directly.

The anisotropy parameters in Table 4.2 and the measured shear stress and strain values were used in Eqs. (4.36) and (4.38) to generate incrementally the equivalent stress-equivalent plastic strain response of the material. It is referred to as the *Material Frame* (MF) response and is plotted in Fig. 4.8a. Included is the corresponding response when the rotation of the material frame is not accounted for—referred to as *Reference Frame* response (RF). Clearly, this particular anisotropy leads to progressive reduction in tangent modulus for equivalent strains larger than about 0.1. In Section 5.1 it will be demonstrated that such changes in modulus can have a significant influence on the prediction of localization and other instabilities and the onset of failure. Chen et al. [2018b] examined how the material frame rotation affects the extraction of the hardening response for the Hill-48 anisotropic yield function-see Appendix D.)

Figure 4.8b shows the equivalent stress-equivalent plastic strain responses corresponding to the isotropic von Mises and Hosford yield functions. Included is the Reference Frame response based on the Yld04-3D anisotropic yield function. The three responses exhibit similar hardening, but trace different stress levels. The difference in stress level between H8 and Yld04-3D is caused by the anisotropy, whereas the difference between vM and H8 is due to the different exponent of the two yield functions.

In order to facilitate a comparison with the response in Figs. 4.8, the material hardening was also measured in an independent uniaxial tension test (see Scales et al., 2019). The test was performed on an axial specimen machined out of a tube form the same batch. The nominal stress achieved a maximum at a strain of only 7%; thus the response was extrapolated using the inverse method of Tardif and Kyriakides [2012]. The location of the neck was controlled by machining a large radius into the sides of the test specimen, and the deformation in this zone was monitored with DIC. Several constitutive models were used in the extrapolation. Figure 4.8a includes the response evaluated using the Yld04-3D constitutive model as calibrated in Section 4.2. The data extend to a strain of about 35% when the specimen failed in the neck. To accommodate the needs of the present study, the response was linearly extrapolated to the same strain level as that of the simple shear test (extrapolation based on the slope of the last 2 points). The uniaxial response traces a slightly lower stress up to a strain of about 0.12 and overshoots the shear response at higher strains.

4.3 Summary and Conclusions

Successful simulation of ductile failure within the framework of conventional plasticity requires suitably calibrated yield functions and material hardening responses to large strains. A non-quadratic yield function Yld04-3D, which has been shown to be

suitable for Al-alloys, is adopted to characterize the anisotropy in Al-6061-T6 tubes used in the study. The model was calibrated using the radial path tension-torsion experiments together with a set of tension-pressure results.

Because of the high strains recorded in the experiments, the material hardening was established from a pure torsion test on a tubular specimen. This test produced a stress-strain response to a much higher strain level than, for example, the value obtained from the necked zone of a tensile test using an inverse method. It was further demonstrated that the extraction of the material hardening must be accomplished using the constitutive model adopted in the simulation of the structural responses, which in this study meant the Yld04-3D yield function. In the simple shear test used the material frame rotates, which must be accounted for in the extraction of the material hardening when using an anisotropic yield function.

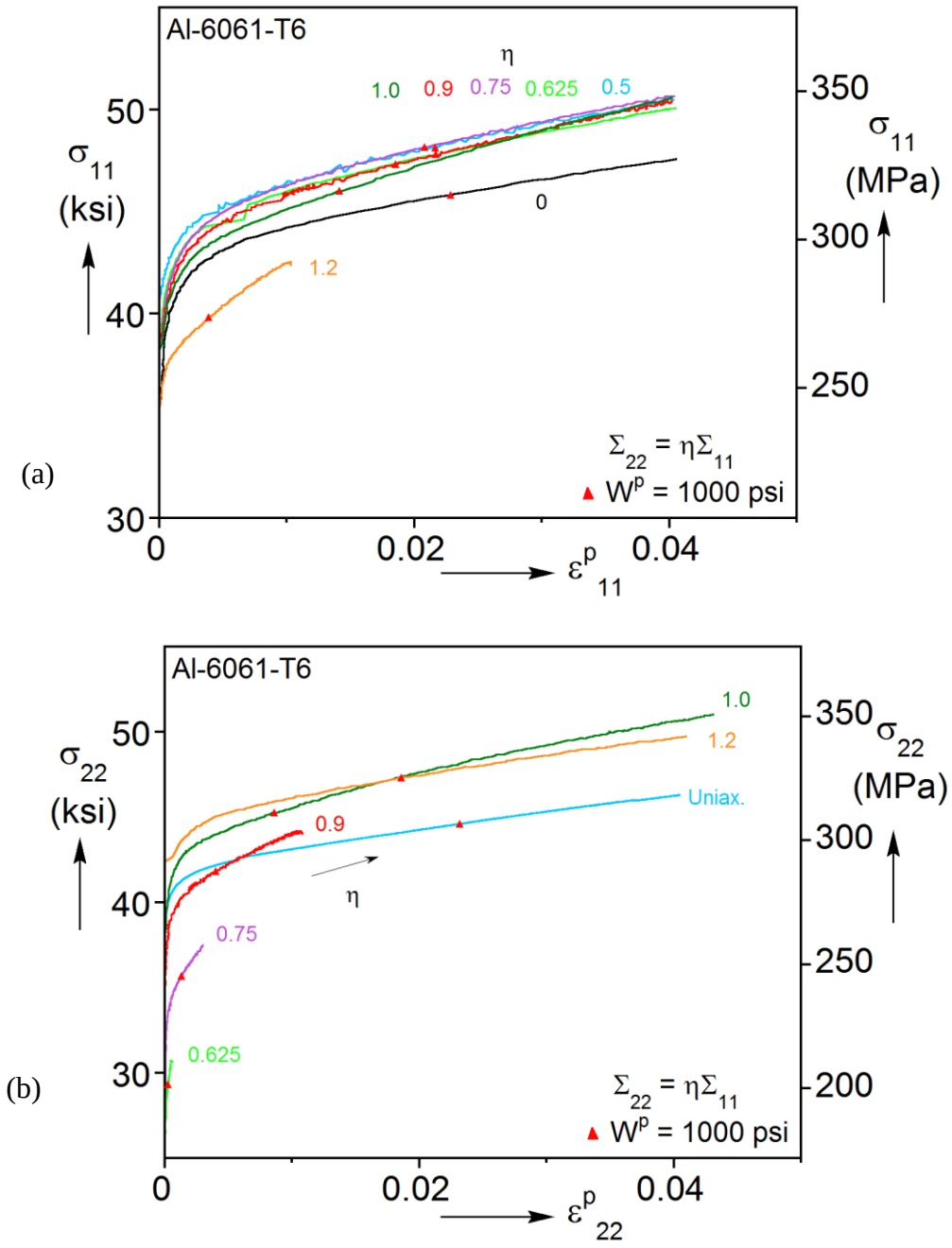

Fig. 4.1 True stress-plastic strain responses for a set of radial path pressure-tension tests in: (a) hoop direction and (b) axial direction. Included in (b) is the uniaxial tension response.

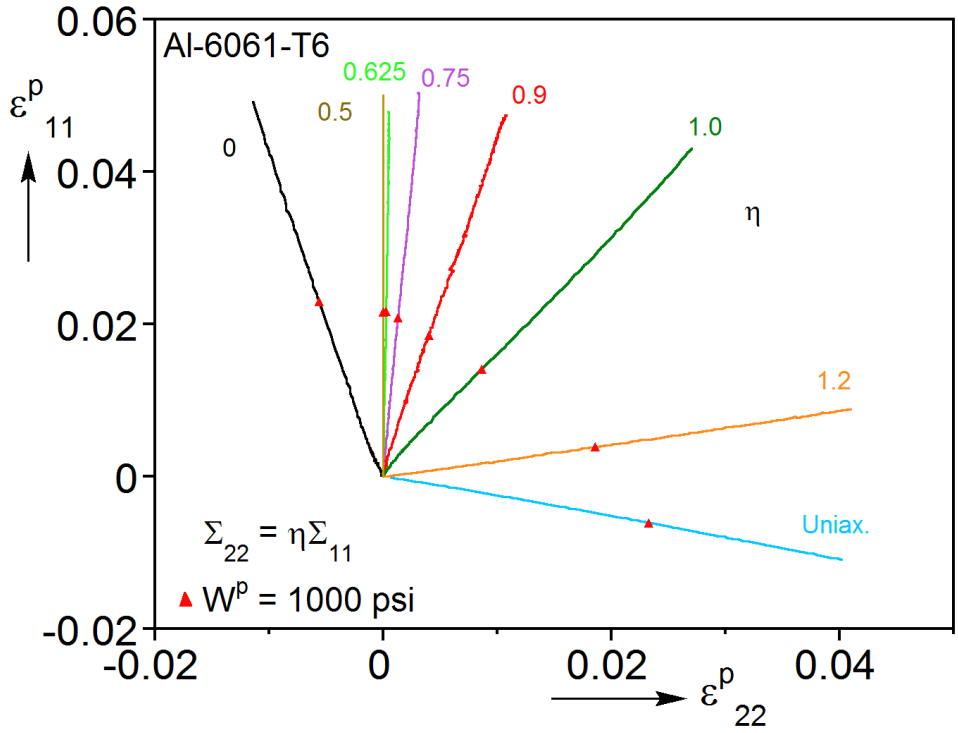

Fig. 4.2 True plastic strain paths for a set of radial path pressure-tension tests. Included is the uniaxial tension strain path.

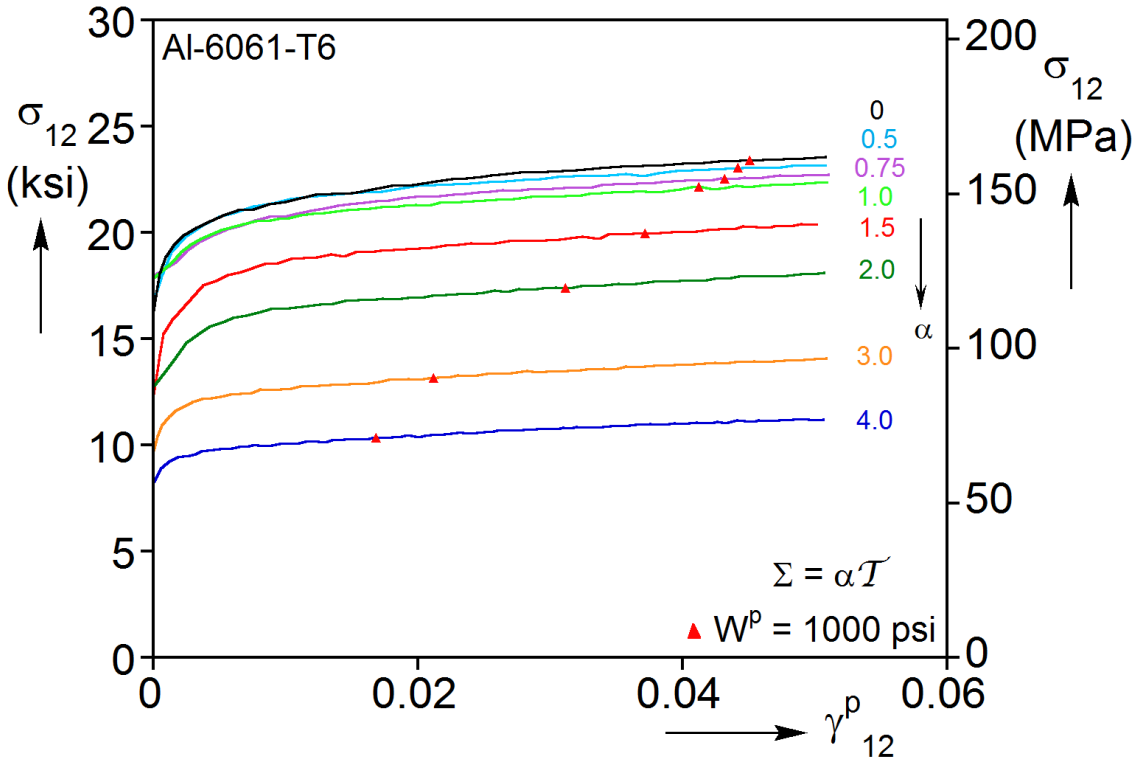

Fig. 4.3a True shear stress-plastic shear strain responses for a set of radial path tension-torsion tests

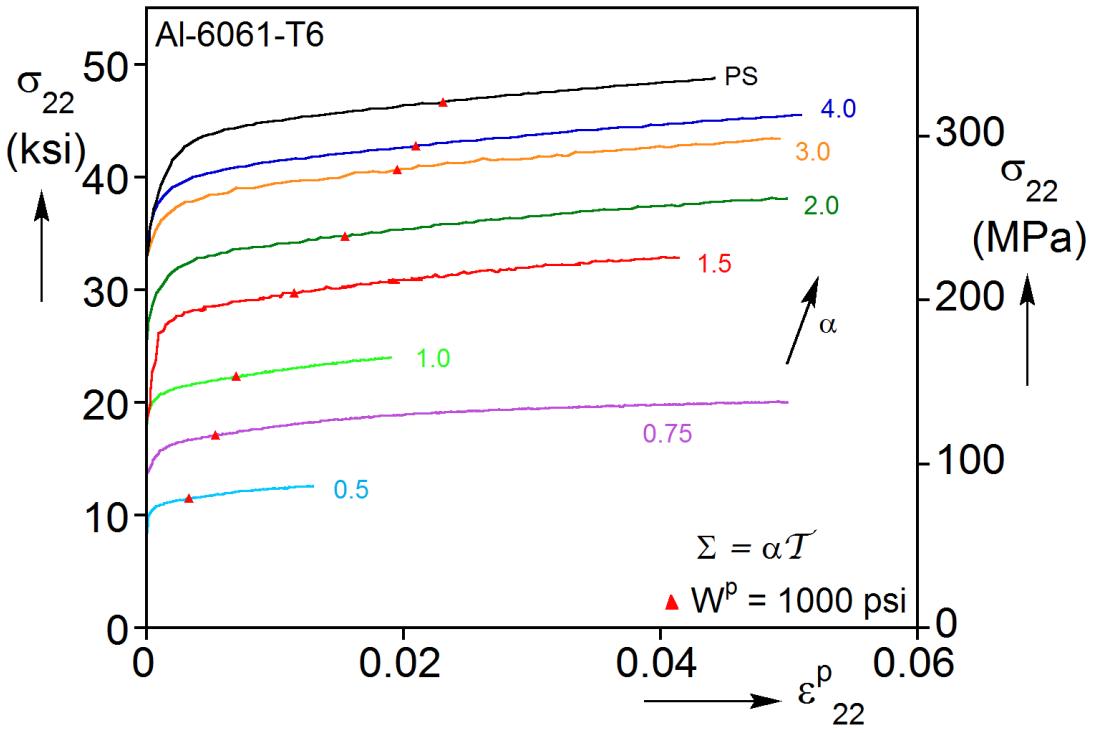

Fig. 4.3b True axial stress-plastic axial strain responses for a set of radial path tension-torsion tests

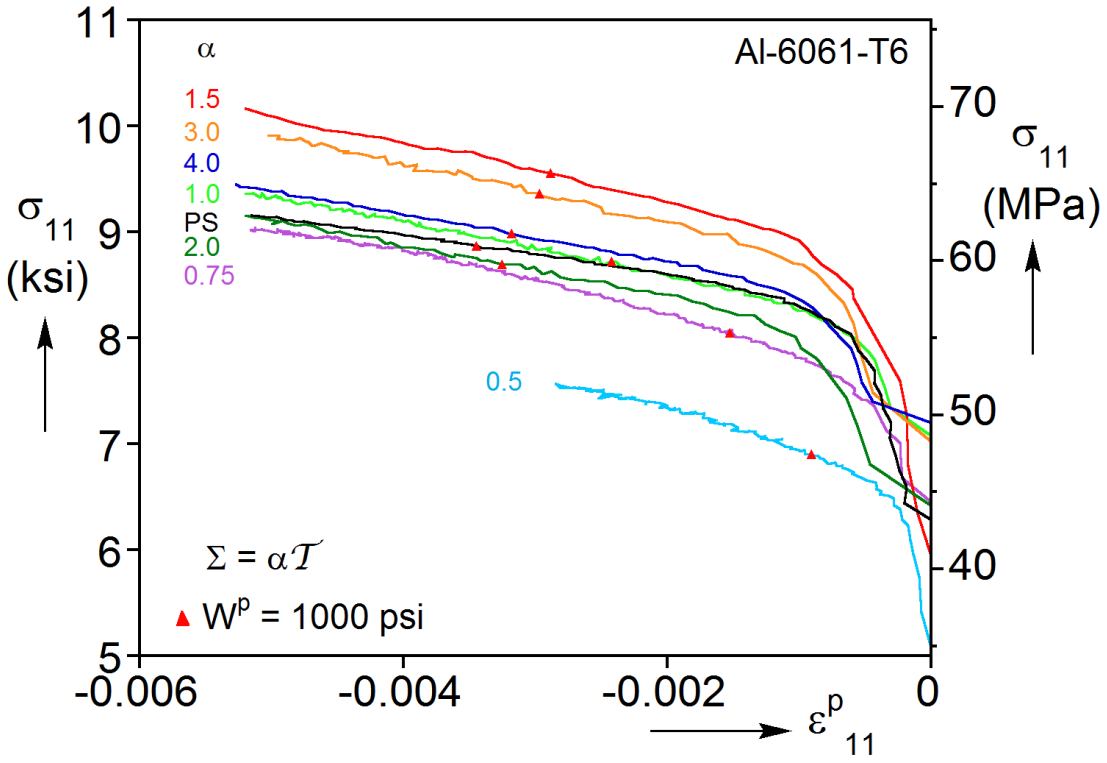

Fig. 4.3c Hoop stress-plastic hoop strain responses for a set of radial path tension-torsion tests

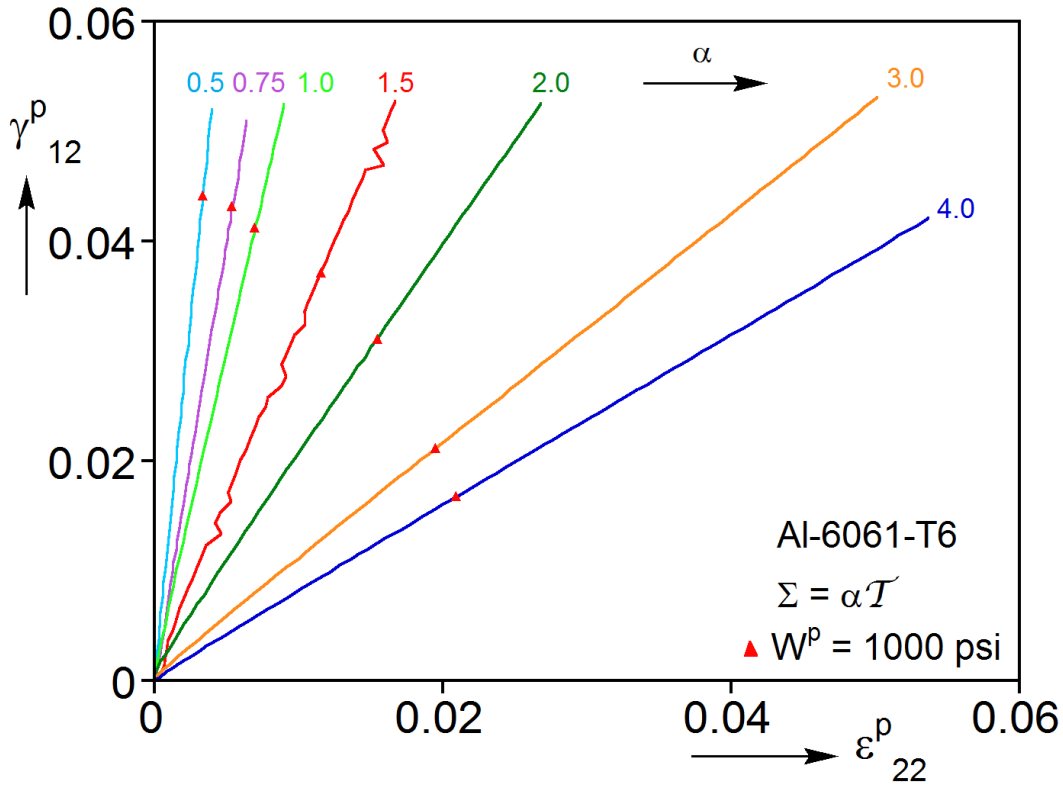

Fig. 4.4a Shear plastic strain vs. axial plastic strain responses for a set of radial path tension-torsion tests

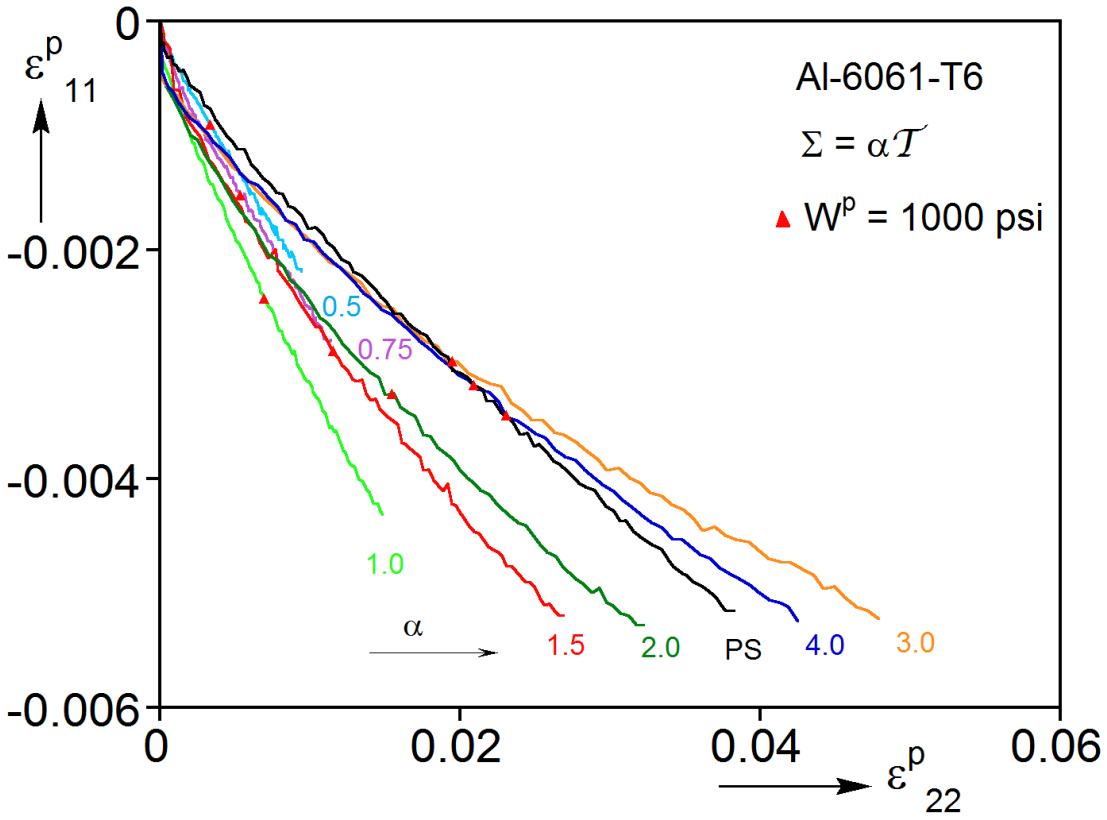

Fig. 4.4b Hoop plastic strain vs. axial plastic strain responses for a set of radial paths tension-torsion tests

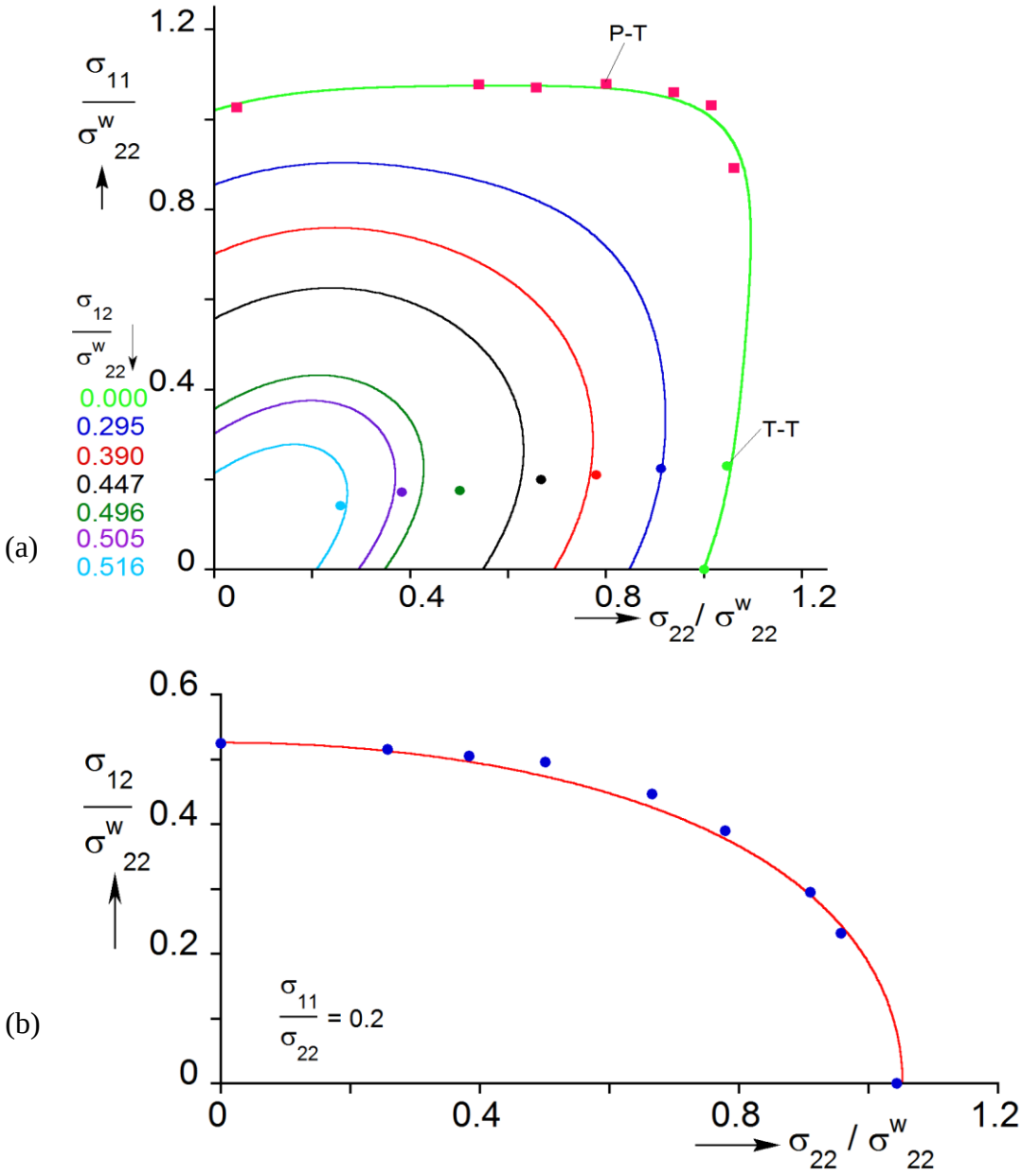

Fig. 4.5 (a) Work contours of the calibrated Yld04-3D constitutive model in the axial and hoop stress space at varying levels of shear. Experimental data used in calibration are included with solid bullets (T-T≡ tension-torsion, P-T≡ pressure-tension). (b) Work contour in the shear-axial stress space for $s_{11}/s_{22} = 0.2$.

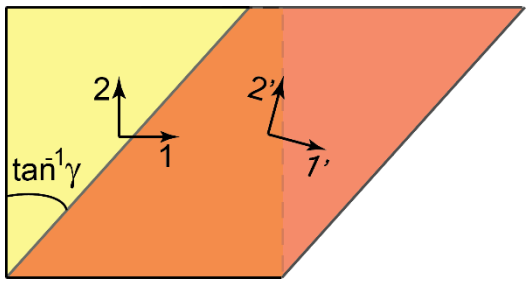

Fig. 4.6 Material element under simple shear; shown are the initial and rotated material axes.

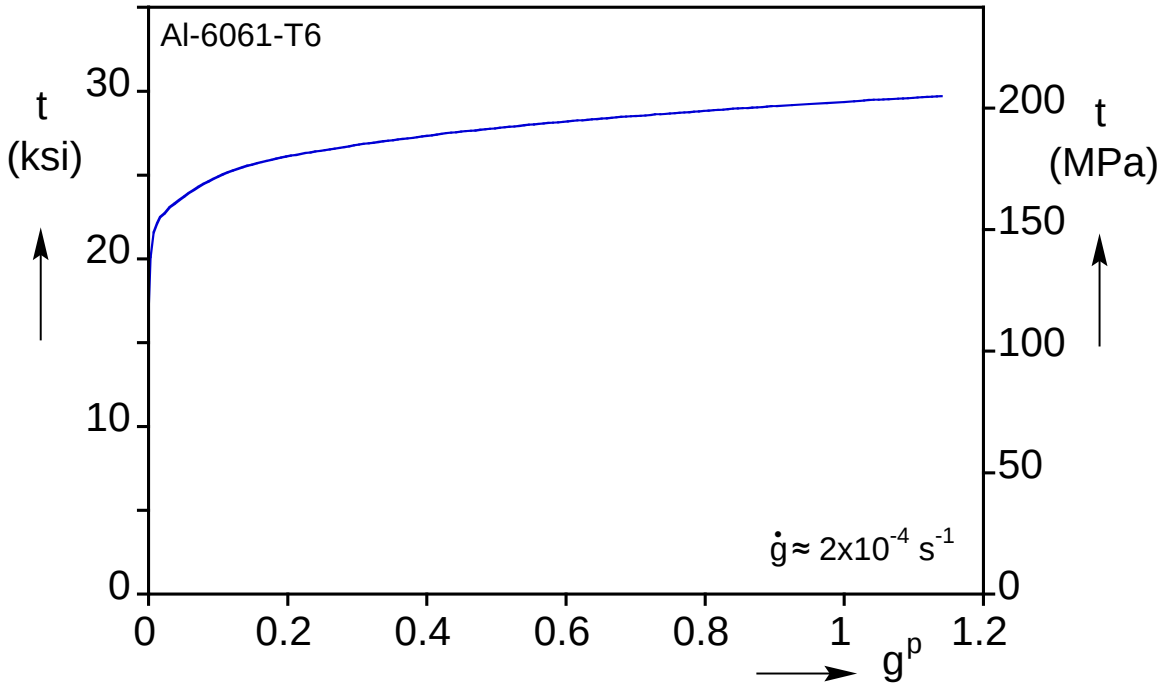

Fig. 4.7 Measured shear stress-plastic shear strain (t - g^p) response for the Al-6061-T6 tube analyzed.

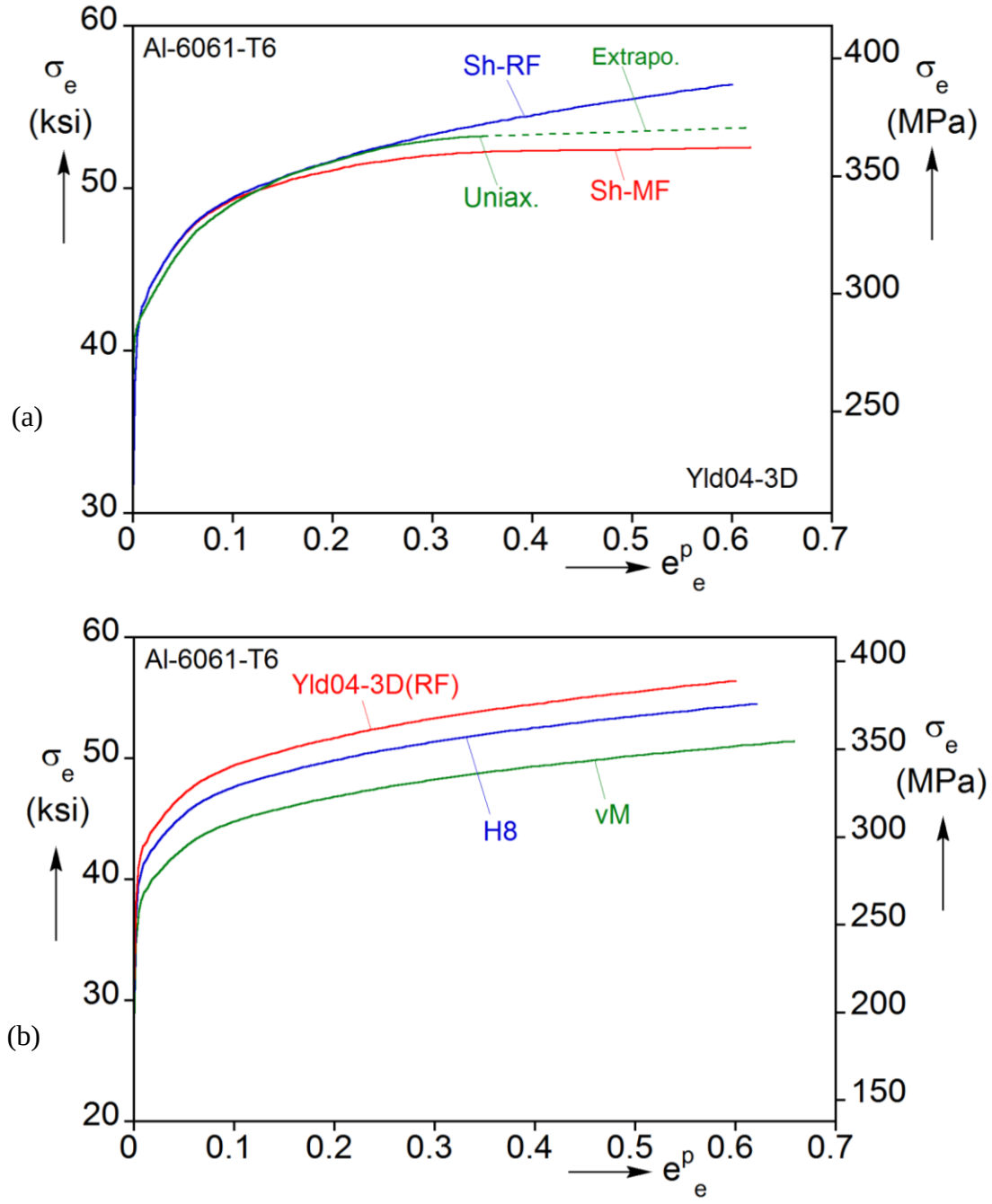

Fig. 4.8 (a) The *Material* and *Reference Frame* equivalent stress-equivalent plastic strain responses extracted from the measured t - g^p response. Included is the material response from a uniaxial tension test. (b) Comparison of the Reference Frame equivalent stress-equivalent plastic strain response with the isotropic von Mises and Hosford responses.

Chapter 5: Numerical Simulation of Tubular Specimen under Tension and Torsion[6]

This Chapter first develops a finite element model appropriate for simulating the tension-torsion experiments of Scales et al. [2019] with emphasis on reproducing the measured responses and the evolution of localized deformation. The three constitutive models of von Mises, Hosford, and Yld04-3D calibrated in Chapter 4, are incorporated in the simulations, each together with the corresponding material hardening response. The calculations first allow the development of a richer understanding of the localization process that precedes failure; and second, comparison of measured and calculated results enables evaluation of the performance of the constitutive models.

5.1 Finite Element Model

The finite element model of the tubular test specimens used in the experiments of Scales et al. [2019] is shown in Fig. 5.1 (see Fig. 1 of Reference). Symmetry about the center of the test section is assumed, which allows consideration of only half of the tubular test specimen. It consists of a 0.330 in (8.38 mm) long thicker upper section, a 0.200 in (5.08 mm) straight test section, connected with a 0.125 in (3.18 mm) radius fillet. The specimen has an axially uniform inner surface with a radius of 0.815 in (20.5 mm); the thicker section has a wall thickness of 0.170 in (4.32 mm) and the test section is assigned the average wall thickness of the specific test specimen analyzed (typically 0.039 in–1.0 mm).

The model is meshed with solid elements in ABAQUS (C3D8R) as follows:

[6] Chen, K., Scales, M., Kyriakides, S. (2019). Material response, localization and failure of an Aluminum alloy under combined shear and tension: Part II Analysis. *Int'l J. Plasticity* **120**, 361-379. (Chen conducted the analysis, numerical simulations and helped write the paper)

- A 0.08 in (2.0 mm) long part of the test section adjacent to the symmetry plane has 9 elements through the thickness and 450 elements around the circumference in order to facilitate the development of the expected localization.
- The rest of the straight test section has a coarser mesh with 3 elements through the thickness and 150 around the circumference.
- The thick upper section has the same mesh distribution and consequently larger elements.
- The fillet also has the same mesh distribution as the two sections it joins so the element size along the length is adjusted to comply with the curvature of the fillet.

The measured wall eccentricity of each specimen, listed in Table 1 of Scales et al. [2019], is incorporated into the model by shifting the inner cylindrical surface relative to the outer one by the required amount, which changes slightly the mesh dimensions.

The degrees of freedom of nodes on the symmetry plane are constrained except that they are free to move in the radial direction. The complex clamping of the specimen used in the experiments was not reproduced in the model. Instead, a reference node was created which is kinematically coupled to the nodes of the upper surface. The specimen was loaded as follows:

- For $a < 3$ the angle of rotation of the reference node is prescribed incrementally causing a change in the torque, which is monitored by a "sensor." An axial force increment is then prescribed through a user subroutine (UAMP) to generate the required axial force-torque proportionality (similar schemes used in Papasidero et al., 2014; Xue et al., 2013).

- For $\alpha \geq 3$ the axial displacement of the reference node is prescribed incrementally resulting in a force registered by the sensor. A torque increment is then prescribed through the UAMP to generate the required axial force-torque proportionality.

5.2 SIMULATION OF THE $a = 0.75$ RADIAL PATH EXPERIMENT

The results of the simulation of the experiment with $a = 0.75$ are now used to illustrate the performance of the numerical modeling effort. The experiment was simulated using the vM, H8 and Yld04-3D constitutive models, along with the corresponding material stress-strain response of each (see Fig. 4.8). Figure 5.2 compares the three calculated nominal shear stress-rotation and axial stress-elongation responses to the experimental ones. As in the experiments, the rotation and elongation are evaluated from the edges of the test section. The three simulations match the experimental responses closely up to yielding. Subsequently, the numerical responses trace mildly hardening trajectories that mimic the experimental one, and develop a limit load followed by a decaying branch, an indication that deformation is localizing ($\triangle \equiv$ limit load). The limit load is the result of tension-induced wall thinning which is also responsible for the subsequent downturn in the nominal stress responses. It is worth remembering that by contrast, under pure torsion the test section wall thickness does not change and deformation does not localize (see Section 3.2 of Scales et al. [2019]). The H8 and Yld04-3D responses match the experimental one very well up to the limit load whereas vM underestimates both the axial and shear stress experimental values. Furthermore, the shear maximum of vM occurs at a much smaller rotation.

5.2.1 Onset of Instability under Combined Tension and Torsion

Because the limit loads correspond to the onset of localization, a critical stress state in manufacturing, it is useful to compare the limit states obtained using the classical analytical Considère condition with the FE model values. At the onset of instability, both the applied force and torque are assumed to reach maxima, i.e.,

$$dF = 0 \tag{5.1a}$$

and $$dT = 0 \tag{5.1b}$$

If elastic deformations and the small radial deflection of the test section are neglected, Eq. (5.1) reduce to:

$$\left.\frac{d\sigma_{22}}{d\varepsilon_{22}}\right|_c = \sigma_{22c}\,. \tag{5.2a}$$

and $$\left.\frac{d\sigma_{12}}{d\varepsilon_{22}}\right|_c = \sigma_{12c} \tag{5.2b}$$

The equivalent stress increment can be related to increments of stress components as follows:

$$d\sigma_e = \frac{\partial \Phi}{\partial \sigma_{22}} d\sigma_{22} + \frac{\partial \Phi}{\partial \sigma_{12}} d\sigma_{12} \tag{5.3a}$$

where F is the yield function, s_e is the associated equivalent stress.

Substituting (5.2) into (5.3a):

$$d\sigma_e = \frac{\partial \Phi}{\partial \sigma_{22}} \sigma_{22} d\varepsilon_{22} (1 + \frac{1}{\alpha} \frac{\partial \Phi}{\partial \sigma_{12}} / \frac{\partial \Phi}{\partial \sigma_{22}}) \tag{5.3b}$$

From work compatibility:

$$\sigma_e d\varepsilon_e = \sigma_{22} d\varepsilon_{22} + 2\sigma_{12} d\varepsilon_{12} \tag{5.4a}$$

where $d\varepsilon_e$ is the work compatible equivalent strain increment.

Using flow rule, Eq. (5.4a) can be rewritten as:

$$\sigma_e d\varepsilon_e = \sigma_{22} d\varepsilon_{22} (1 + \frac{1}{\alpha} \frac{\partial \Phi}{\partial \sigma_{12}} / \frac{\partial \Phi}{\partial \sigma_{22}})\,. \tag{5.4b}$$

Combining (5.3b) and (5.4b), it can be shown that for isotropic yield functions the onset of instability implies that

$$\left.\frac{d\sigma_e}{d\varepsilon_e}\right|_c = \sigma_e \left.\frac{\partial \Phi}{\partial \sigma_{22}}\right|_c\,. \tag{5.5}$$

For vM $$\Phi = \left(\sigma_{11}^2 + \sigma_{22}^2 - \sigma_{11}\sigma_{22} + 3\sigma_{12}^2\right)^{1/2} \tag{5.6a}$$

Then (5.5) becomes

$$\left.\frac{d\sigma_e}{d\varepsilon_e}\right|_c = \frac{\sqrt{3}\sigma_{ec}}{2[1+4/a^2]^{1/2}}. \tag{5.6b}$$

The equivalent strain at the limit load can be evaluated from (5.6b) using the material response for vM extracted from the simple shear test in Fig. 4.8b. For $a = 0.75$ $\varepsilon_{ec}^p = 0.247$, which compares with 0.244 from the FE model (taken from the mid-thickness at the symmetry plane). Similar level of agreement was found for all radial paths with $\alpha \geq 0.5$, and this is demonstrated in Fig. 5.3 where numerical and analytical equivalent critical strains are compared. For even smaller values of a, localization becomes increasingly more difficult to achieve numerically requiring the introduction of a small thickness imperfection in the FE model.

The critical state for H8 can be similarly derived analytically from (5.5) as outlined in Appendix E. The same procedure is applicable to the Yld04-3D anisotropic yield function, which however requires numerical treatment. Overall, the critical strain predicted for all three constitutive models was found to be within a few percent of the values from the full finite element simulations. This points to the usefulness of the Considère type analysis for estimating the limit states for uniform axial-shear stress states.

5.2.2 Evolution of Localized Deformation

We now compare additional aspects of the numerical simulations to the experimental results in some detail. Figure 5.4a compares the radial deflection across the test section predicted using Yld04-3D with the measured values at the three stations marked on the experimental responses in Fig. 5 of Scales et al. [2019] — profiles ③ correspond to the location of the limit load in the experiment. The predicted profiles are in good agreement with the measured values. This agreement is another indication of the success of the Yld04-3D calibration scheme used. It is worth pointing out that although for smaller

values of a the radial deformation is quite small, the stress inhomogeneity caused by it is sufficient to trigger localization without the need for a geometric imperfection perturbation for all values of biaxiality ratios considered except for $a = 0.5$. For the smallest a the induced radial deformation is too small, so localization was induced by decreasing the wall thickness by 0.1% in a circular band $2t_o$ wide spanning the symmetry plane.

Beyond the limit loads, deformation localizes for all three constitutive models and both the nominal shear and axial stresses in Fig. 5.2 start to decrease. The decaying part of the vM shear response occurs early and the downturn is more pronounced. The Yld04-3D matches the experimental downturn very well and the H8 downturn occurs at a slower rotation rate. A diffuse neck approximately $2t_o$ wide starts to develop forming a circular band spanning the symmetry plane. Figure 5.4b plots the equivalent plastic strain on the outer surface at the symmetry plane against the rotation angle from the three models (note that the variation in strain across the wall thickness is quite small). Included for comparison is the corresponding experimental plot. The three calculated trajectories track the experimental one up to their respective limit loads, and take a significant upturn thereafter. The H8 and Yld04-3D results follow the nearly exponential growth of the experimental trajectory very well. The vM trajectory on the other hand, although exhibiting a similar increasing trend, takes place at a much smaller rotation because of the early development of the load maxima. The trajectories clearly indicate the significant shearing and axial deformation experienced in the localizing zone.

The evolution of the deformation in the localizing zone produced by the Yld04-3D model, is illustrated in Fig. 5.5a, which plots ten profiles of equivalent plastic strain over a $6t_o$ height across the band corresponding to the stations marked on the experimental responses with "○" symbols in Fig. 5.2. Profiles ① and ② correspond to the early parts of the stress history so they show the deformation to be essentially uniform across this zone.

Profile ③, which corresponds to the f at the experimental load maxima, is also uniform but slightly bent upwards due to the radial deformation of the test section in Fig. 5.4a (note that the predicted load maximum occurs at a somewhat larger f than in the experiment). Beyond this point deformation concentrates in a zone about $2t_o$ wide while outside the band the deformation remains relatively unchanged. This divergence in the deformation between points within and outside the localizing band is also illustrated in Fig. 5.4b, which includes the strain-rotation response outside the localizing zone at $y = 3t_o$.

The neck that forms is seen to sharpen with the deformation concentrating in the central few elements. By station ⑩ the strain in the center of the neck has reached a value of about 1.0, which corresponds to the mean strain at failure reported in the experiment. Figure 5.5b shows a cross sectional view of the necked zone at the plane of symmetry of the FE model at station ⑩. Superimposed are color contours corresponding to equivalent plastic strain. The upper edge represents the outer side of the specimen and the arrows indicate the $6t_o$ length captured in Fig. 5.5a. It is noteworthy that the localization is in the form of a diffuse neck as seen in experiments by sectioning. Furthermore, the deformation across the wall thickness is seen to be quite uniform (less than 1% difference between the center and the outer surface). The small curvature of the section is due to the radial deflection mentioned earlier. This zone was meshed with 9 nearly cubical elements across the wall thickness (see Fig. 5.1). This discretization roughly corresponds to that of the DIC, governed by the facet size and spacing, used to capture the deformation in the experiment. Increasing the number of elements in this zone does not change the width of the neck but allows sharper strain gradients to develop leading to an increase in the peak strain. Furthermore, in the absence of a failure criterion, the FE analysis must be terminated by the operator. Thus in Fig. 5.4b each of the three strain trajectories were terminated at a value of about 1.0, which is the mean measure of failure strain in the experiment.

5.2.3 Structural Responses Based on Alternative Hardening Curves

For comparison purposes the $a = 0.75$ experiment was also simulated using the material hardening response extracted from the uniaxial tension test for the same constitutive model–shown extrapolated in Fig. 4.8a. The shear-rotation and axial stress-elongation responses are compared to the ones based on the simple shear stress-strain response in Fig. 5.6. The two material hardening models produce similar responses but the limit loads of the Uniax. material are delayed somewhat, while subsequently the stress drops at a similar rate. The effect of this difference on the equivalent strain at the symmetry plane, is illustrated in Fig. 5.4b. The trajectory of "Uniax." is similar to that from the Sh-MF model, but the upturn is now delayed moving from $\phi \approx 13.9^\circ$ to 15.4°. It must, however, be emphasized that the neighborhoods of the limit loads and beyond occur at high enough strains to be influenced by the extrapolation of the uniaxial response adopted. For completeness Fig. 5.6 includes responses based on the Reference Frame (RF) hardening curve (Fig. 4.8a) which, in the strain regime of interest here, is much stiffer than the Material Frame (MF) response. Consequently, the localization is delayed to strain levels much higher than those of the experiment.

5.3 Simulation of the $\alpha = 2.0$ Radial Path Experiment

We now examine in some detail the results of the numerical simulations for $a = 2.0$, which is representative of the more axial stress dominant stress paths considered. Figures 5.7 to 5.10 present similar sets of results as those presented for $a = 0.75$. Figures 5.7 compare the shear-rotation and axial stress-elongation responses calculated using the three constitutive models with the experimental ones. The shear response is predicted very well by Yld04-3D including the limit load and the decaying part after it. H8 is very good up to the limit load, which however occurs slightly earlier causing the post-limit load

response to start its downward trajectory somewhat earlier. The vM underpredicts the complete response for this case also. The axial stress responses for Yld04-3D and H8 follow each other closely. Their limit loads occur somewhat earlier and the decaying trajectories occur somewhat earlier than in the experimental response. The vM response underpredicts the complete experimental one again.

Figure 5.8a compares the radial deflection across the test section predicted by the Yld04-3D analysis for three stations, with station ③ corresponding to the limit load in the experiment. The predicted deflections follow those measured very well. Higher axial stress is of course expected to result in deeper necking. However, the maximum value of the radial displacement at ③ is smaller than that in Fig. 5.4a, because here the limit load occurs at smaller overall strains.

Figure 5.8b draws the evolution of strain with f on the outer surface at the symmetry plane together with the corresponding experimental result. The Yld04-3D trajectory matches the experimental one very well in all respects. The H8 trajectory starts on the upward path earlier than the experiment, this despite producing stress responses that are close to those of Yld04-3D in Fig. 5.7. The vM trajectory is between those of Yld04-3D and H8. The results demonstrate that accurate prediction of the structural responses is not sufficient for evaluating the performance of each constitutive model.

Figure 5.9a shows the evolution of deformation in the localization zone produced by Yld04-3D. Plotted are ten profiles of equivalent plastic strain that correspond to the stations marked on the measured stress-deformation responses in Fig. 5.7 with open symbols – ○. Following the load maxima deformation localizes becoming progressively more concentrated in a zone about $3t_o$ tall while outside this zone deformation remains essentially unchanged. In configuration ⑩, which corresponds to the last station before rupture occurred in the experiment, the strain in the neck is just under 0.6. This is

significantly lower than the 1.0 strain achieved for $\alpha = 0.75$ at the point of rupture. A cross section of the necked region in this configuration is shown in Fig. 5.9b. Despite the smaller maximum strain, the neck is deeper and more diffuse. Furthermore, the strain varies more across the wall thickness than for $\alpha = 0.75$ with the maximum being in the center where the strain is about 20% higher than on the outer surface. It's worth pointing out that in this configuration, the row of elements at the symmetry plane are rather elongated, which may affect the accuracy of the local strain. Further refinement of the mesh can improve the accuracy of the local strain when they are implemented in a failure criterion. Such a refinement has small influence on the calculated responses in Fig. 5.7.

Figure 5.10 compares the shear stress-rotation and axial stress elongation responses produced using the simple shear (Sh-MF) and uniaxial (Uniax.) stress-strain responses, both based on Yld04-3D. The limit load of the $\mathcal{T}$ - f response based on the uniaxial hardening is delayed compared to the experimental one and so is the decaying part. The same is the case for the $\mathcal{S}$ - d response. This limit load occurs at a relative small strain (~0.12) where the Uniax. has a higher tangent modulus than the Sh-MF stress-strain response, causing the observed difference in the limit load. The delay in the downturns of the two responses results in a significant delay in the rotation angle at which the upturn in the equivalent strain takes place in Fig. 5.8b.

5.4 Summary of Simulations of All Radial Path Experiments

All seven radial path tension-torsion experiments were simulated numerically and the same sets of results as those presented for $\alpha = 0.75$ and 2.0 were generated. For brevity here we present the predictions using Yld04-3D and limit discussion about the other two sets of predictions to general trends. Figure 5.11 compares the calculated shear-rotation and axial stress-elongation responses using Yld04-3D with the experimental responses.

The shear responses are uniformly in very good agreement with the measurements. The responses track the experimental ones very closely. The rotations at the limit loads are also in good agreement with those of the measured responses, except for $a = 0.5$ where the predicted limit load is somewhat delayed. The decaying shear stress trajectories are also in very good agreement with the experimental ones. The corresponding H8 predictions shown in Fig. 5.12a follow the responses up to the limit loads. The limit loads tend to be somewhat delayed for low values of a causing a delay in localization, while for the axial stress dominant paths the responses are close to those of Yld04-3D. By contrast, the vM responses shown in Fig. 5.13a uniformly underpredict the experimental ones, and in most cases the limit load and the subsequent downturns are also missed.

The axial stress-elongation predicted using Yld04-3D (Fig. 5.11b) track the experimental ones well up to the limit loads with the elongations at the limit load predicted adequately also. The localization parts of the responses that follow the stress maxima agree with the experimental ones for the three lower values of a, but undershoot them for the four higher stress ratios. The H8 responses shown in Fig. 5.12b follow the Yld04-3D ones closely and produce limit loads that are also close except for lower values of a. The post-limit load responses are close to those of Yld04-3D for higher stress ratios, but tend to localize early for the lower ones. The vM responses shown in Fig. 5.13b are also lower than the measured ones, the limit loads are mostly off, and the localizing sections occur either early or late.

Figure 5.14 plots the equivalent plastic strain at the symmetry plane vs. rotation from the Yld04-3D predictions together with the corresponding results from the seven experiments. The predictions track the measured trajectories very well for the higher stress ratios. For the two lower values of a the trajectories undershoot the experimental ones up to the limit load but follow the experimental trend during the localization upturn. The ends

of the experimental trajectories correspond to rupture, so the predictions were terminated at the same strain. It is noteworthy that the evolution of necking was captured with the same degree of success as in the two examples shown in Figs. 5.5b and 5.9b. Interestingly, the upturn of the strain-rotation for the H8 predictions, as shown in Fig. 5.15, occurs at a smaller value of f than in the experimental results, much like the $a = 2.0$ case in Fig. 5.8b. The predicted trajectory for the 0.5 stress ratio is an exception as here the upturn occurs well after the experimental one. The corresponding vM results shown in Fig. 5.16 are uniformly poor, particularly so for lower values of a. In summary, from these results we can conclude that use of a suitably calibrated non-quadratic yield function, together with a suitably extracted and calibrated material hardening response are essential for reproducing the response and localization that precedes failure. The introduction of anisotropy through the Yld04-3D model generally improves the predicted results particularly so for the evolution of localization.

5.5 Simulation of the Corner Path Experiments

Scales et al. [2019] conducted two pairs of corner path loading experiments to explore the path-dependence of failure with α = 1.0 and 2.0. They consist of an experiment in which the specimen is preloaded in tension and then loaded to failure in shear $(\Sigma \rightarrow \mathcal{T})$, and a second one in which it is preloaded in shear and then loaded to failure in tension $(\mathcal{T} \rightarrow S)$. For the $(S \rightarrow \mathcal{T})$ paths, the specimen is first loaded axially in displacement control up to the nominal axial stress at which failure occurred in the corresponding radial path experiment. When the specified load is reached, it is maintained by switching the controller into load control. The specimen is then subjected to torsional loading under rotation control until failure. In the case of the $(\mathcal{T} \rightarrow S)$ paths the order is reversed: The specimen is first torqued until the nominal shear stress reaches the value at which failure

occurred in the corresponding radial path experiment, and from then on the specimen is loaded axially to failure under displacement control while the torque is maintained. The corresponding stress histories are shown in Fig. 5.17.

The $a = 1.0$ and 2.0 families of corner paths reported in Scales et al. [2019] were also simulated numerically and the predictions based on the Yld04-3D constitutive model are illustrated in Figs. 5.18-20. Figures 5.18 compare the calculated and measured shear-rotation and axial stress-elongation responses for the radial, $S \to T$ and $T \to S$ paths for $a = 1.0$. As reported earlier, the two calculated responses for the radial path reproduce the experimental trajectories but at somewhat lower stress levels. The predictions for the $S \to T$ compare very well with the experimental responses. For the $T \to S$ path the shear response is reproduced well but the axial response is underpredicted rather significantly. This may be related to the fact that the work contour of the calibrated Yld04-3D model corresponding to $s_{12} = 0.496 s_{22}^{w}$ (i.e., $a = 1.0$) undepredicted the experimental data point (see Fig. 4.5a) and this results in earlier yielding for this value of a. The equivalent strain-rotation results are compared to the measurements in Fig. 5.19a. Here the radial path trajectory is reasonably close to the measured one; the upswing of the $S \to T$ response occurs somewhat earlier than the experiment, while the trajectory for the $T \to S$ path is delayed compared to the experimental one.

Figure 5.20 compares the calculated and measured stress responses for the three $a = 2.0$ paths. The radial path predictions follow the measured responses very well for shear while for the axial stress the downturn occurs somewhat earlier. The equivalent strain trajectory in Fig. 5.19b matches the experimental one very well. Both of the $T \to S$ stress responses are reproduced with similar level of agreement to the radial results and so is the equivalent strain-rotation trajectory in Fig. 5.19b. For the $S \to T$ path the shear response traces a somewhat lower trajectory than the experimental one. The equivalent strain in Fig.

5.19b follows the trend of the measured results but the upswing occurs earlier. The predictions for the vM and H8 constitutive model were much worse and are not included here.

Overall the performance of the analysis in the corner paths is reasonably good but not as good as for the radial paths. The agreement with the measured results can be improved by including data from the corner paths in the calibration of the anisotropic yield function.

5.6 Summary and Conclusions

This chapter presented a numerical framework for predicting the set of tension-torsion responses reported in Scales et al. [2019] all of which exhibited limit load instabilities followed by extensive localized deformation that eventually resulted in failure. Motivated by the limited damage observed in Al-6061-T6 at high strains, the experiments are simulated using a customized constitutive model free of the "softening effects" of damage often used in failure predictions. The analysis incorporates a non-quadratic anisotropic yield function, a material hardening response extracted to large strains from a simple shear test, and appropriate finite element models.

The analysis successfully reproduced the measured biaxial stress-deformation responses starting from the onset of yielding; the stress levels in the extended branches that follows where the deformation in the test sections is homogeneous; the stress and deformation levels at which the load maxima occur; and the stress decaying branches associated with localized deformation. The analysis captured the geometry of the localization zones, the nearly exponential growth of strain in them and the associated sharp strain gradients to strain levels that correspond to the recorded failure strains. Most importantly, this level of success was achieved without the artificial introduction of any

softening features to the constitutive model adopted (for alternate approaches to the modeling of tension-torsion experiments see for example Xue et al. [2013], Papasidero et al. [2014, 2015]). Following are observations, comments and conclusions derived from this analysis effort.

- An essential aspect of this successful performance of the analysis is first the adoption of a non-quadratic yield function suitable for Al-alloys, coupled to an accurate representation of the anisotropy induced to the tubes used in the experiments by the extrusion process. This was achieved using the Yld04-3D yield function with exponent 8, calibrated using the radial path biaxial stress states of the tension-torsion experiments of Scales et al. [2019] together with the tension-pressure results presented in Appendix A of Scales et al. [2019].
- A second essential component of such analyses that is often difficult to adhere to, is a stress-strain response that captures the hardening of the material to the strain levels reached in the experiments simulated. Because of the high strains recorded in the experiments, the material hardening was established from a pure torsion test on a tubular specimen. This test produced a stress-strain response to a much higher strain level than, for example, the value obtained from the necked zone of a tensile test using an inverse method. It was further demonstrated that the extraction of the material hardening must be accomplished using the constitutive model adopted in the simulation of the structural responses, which in this study meant the Yld04-3D yield function. In the simple shear test used the material frame rotates, which must be accounted for in the extraction of the material hardening when using an anisotropic yield function.
- The test specimen design allows the state of stress and strain in the test section to remain essentially uniform up to the attainment of the load maxima—the small amount of radial deflection in the test section can be neglected. Thus, the onset of the load

maxima, important in structural design, can be evaluated from simple Considère-type considerations. The accuracy of such calculations is decisively dependent on the yield function adopted and the availability of an accurate representation of material hardening. This of course is equally applicable to the prediction of the load maxima by the numerical model.

- Localization is best modeled numerically using solid elements. Reproducing the high strain gradients that develop in the necked zones to the levels achieved in the experiments requires a very fine mesh in these zones.
- The aluminum alloy used in the experiments had very small initial porosity and very limited pore growth was observed outside the failure zone. Since the failure surfaces exhibited the dimpled relief associated with void growth, this must have occurred very close to the end of life of the material. This material characteristic is at least partly responsible for the successful reproduction of the local deformations to strain levels at which rupture occurred without the introduction of damage.
- The simulations reproduced the localized deformations that developed in the experiments at rupture. Termination of such analyses requires a failure criterion. A properly generated failure locus such as the one in Scales et al. [2019] can be fitted to one of several existing expressions for failure strain vs. triaxiality and Lode parameters. Such expressions can then be used in large-scale calculations of structures under extreme loadings to terminate the life of material points and follow the progression of failure in the structure. For example, the exponential relationship of failure strain to triaxility of Johnson-Cook [1985] or the Hosford-Coulomb expression in Mohr and Marcadet [2015] lend themselves for such calculations.

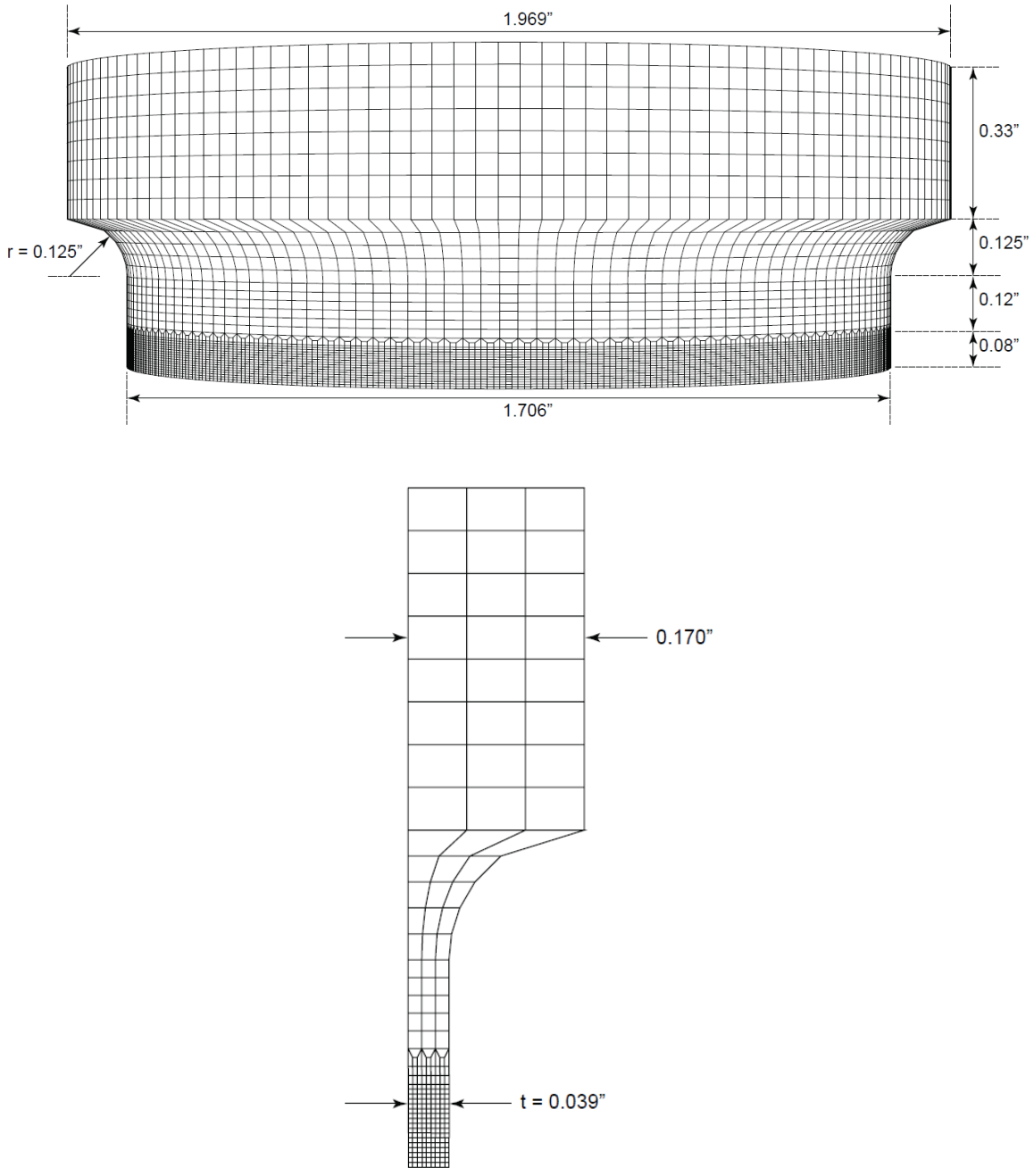

Fig. 5.1 Tension-torsion tubular specimen finite element mesh used to simulate the experiments

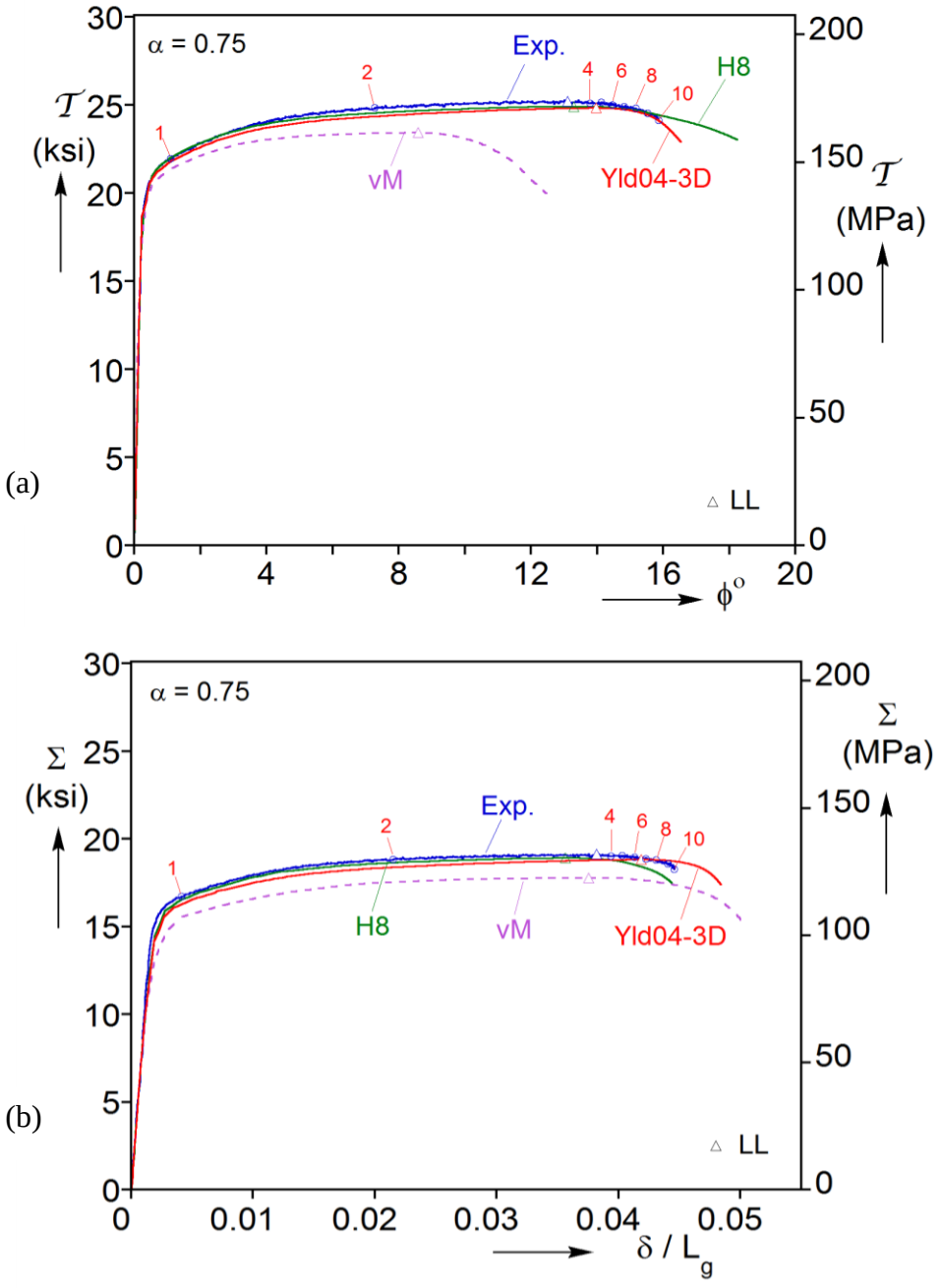

Fig. 5.2 Comparison of measured and predicted responses using three different constitutive models for $a = 0.75$. (a) Shear stress-rotation and (b) axial stress-elongation. The symbols "△" correspond to the nominal stress maxima or "limit loads."

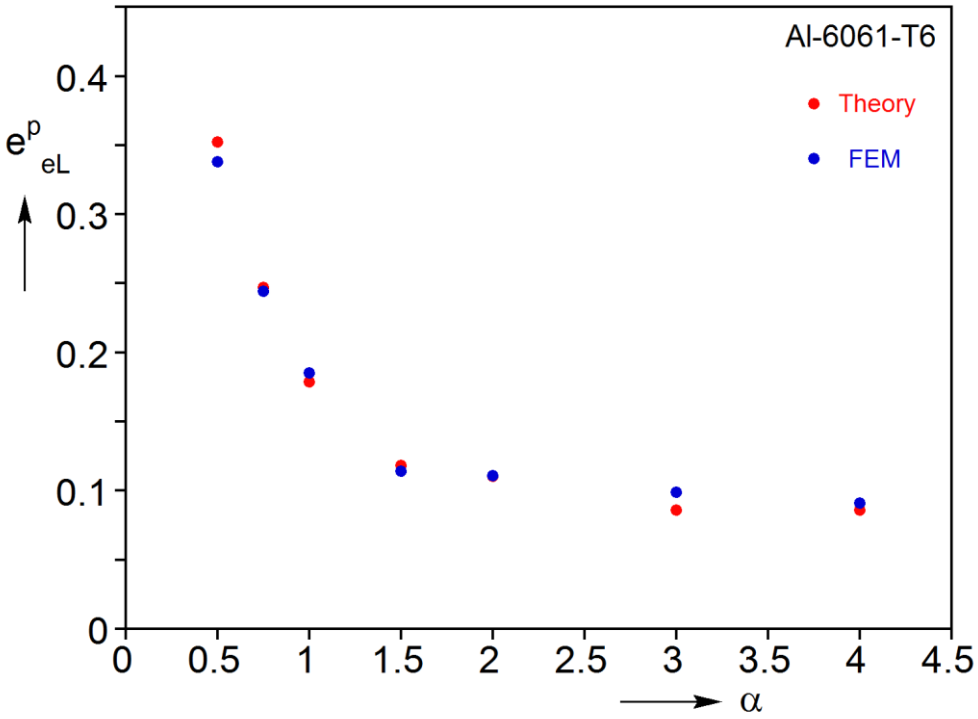

Fig. 5.3 Comparison of the tension-torsion instability strains from Considère analysis and 2D-FEM simulation, results based on von Mises model.

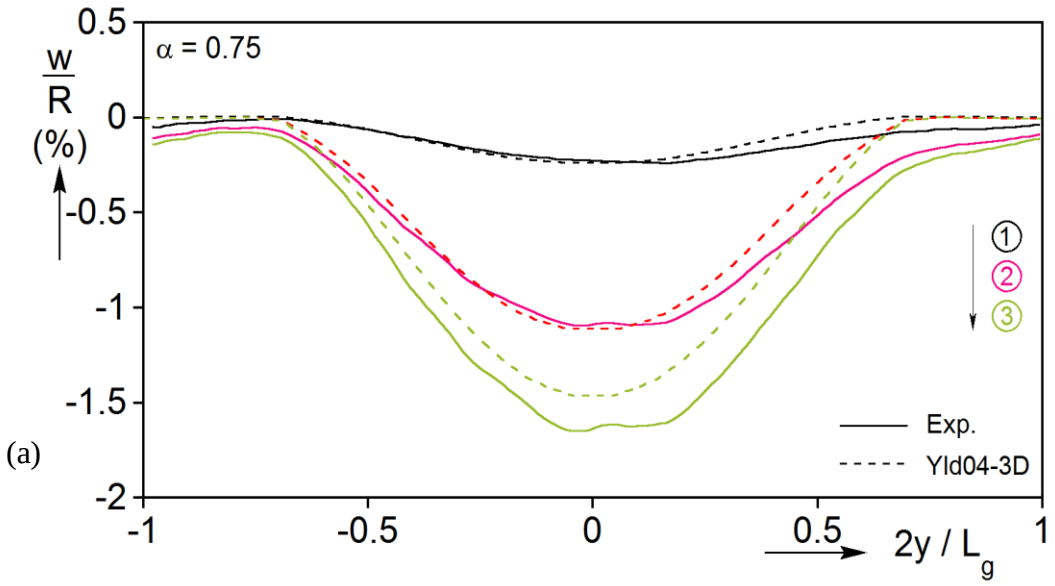

Fig. 5.4 (a) Comparison of measured and calculated radial displacement profiles across the length of the test section for $a = 0.75$, for the first three stations marked in Fig. 5.2.

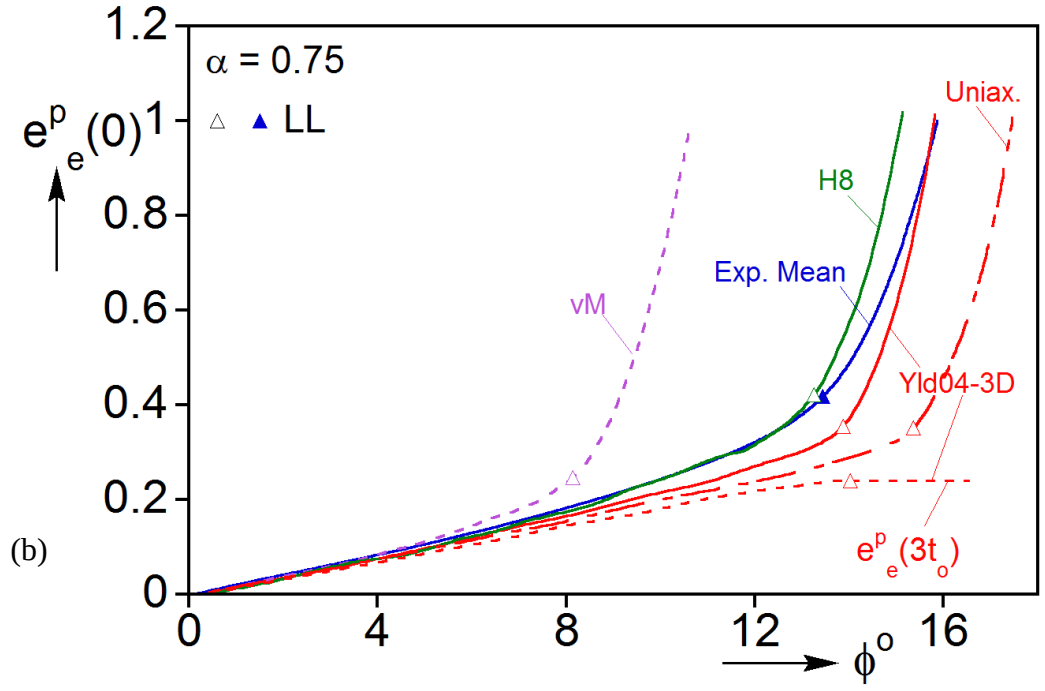

(b)

Fig. 5.4 (b) Measured *Mean* equivalent plastic strain in the localizing zone vs. rotation for $a = 0.75$, and corresponding ones calculated using the vM, H8 and Yld04-3D constitutive models. Included is the strain at $3t_o$ above the localizing zone. Shown also is the response produced using the stress-strain response from the uniaxial test (see Fig. 4.8a). The symbols "△" correspond to the nominal stress maxima or limit loads.

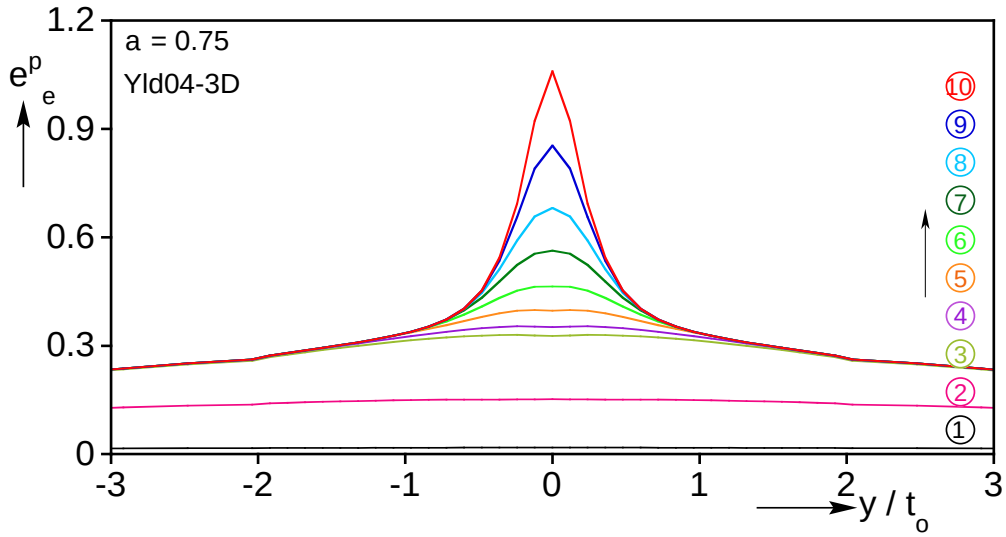

(a)

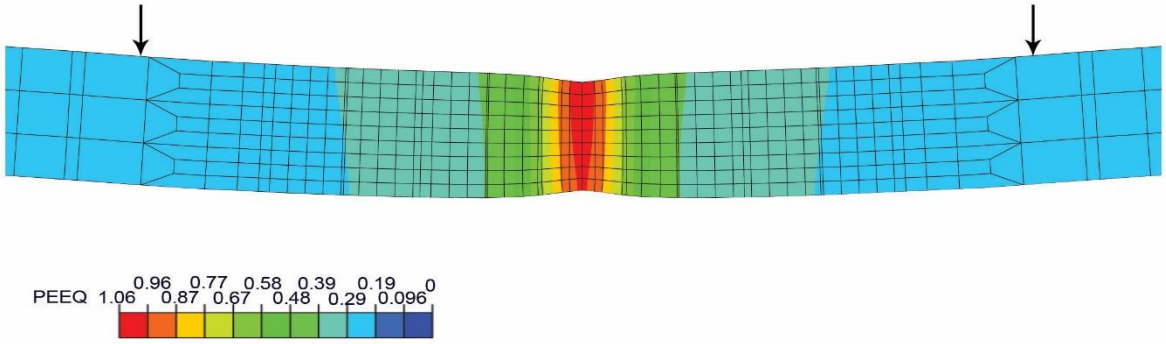

(b)

Fig. 5.5 (a) Calculated equivalent plastic strain profiles across the test section for $a = 0.75$, at rotations corresponding to those on the numbered stations in Fig. 5.2. (b) Through-thickness view of the plane of symmetry (mirrored) showing the necked region corresponding to station ⑩ in Figs. 5.2 and 5.5a––arrows are $6t_o$ apart.

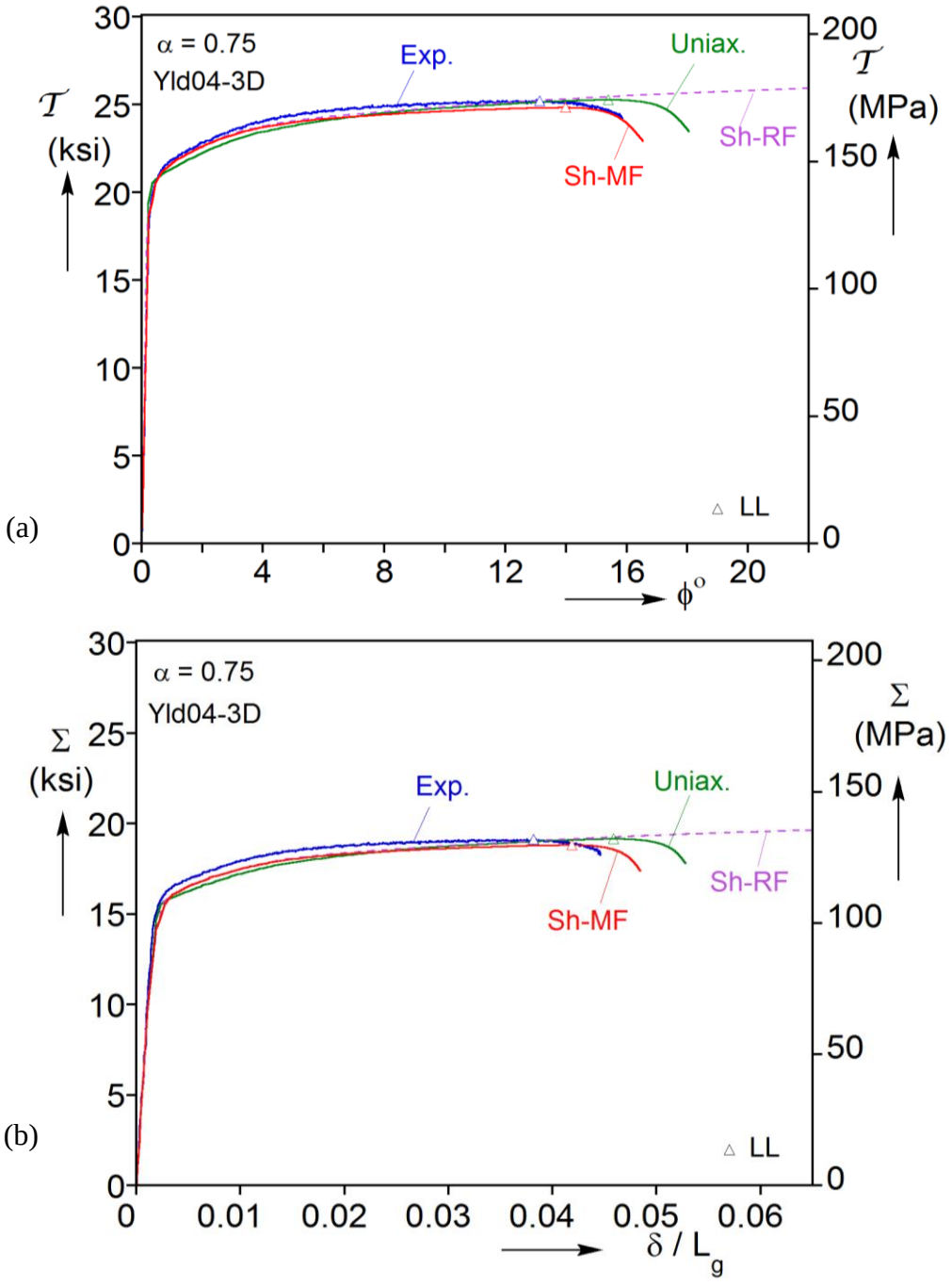

Fig. 5.6 Measured and predicted responses using the shear and uniaxial stress-strain responses for $a = 0.75$. (a) Shear stress-rotation and (b) axial stress-elongation.

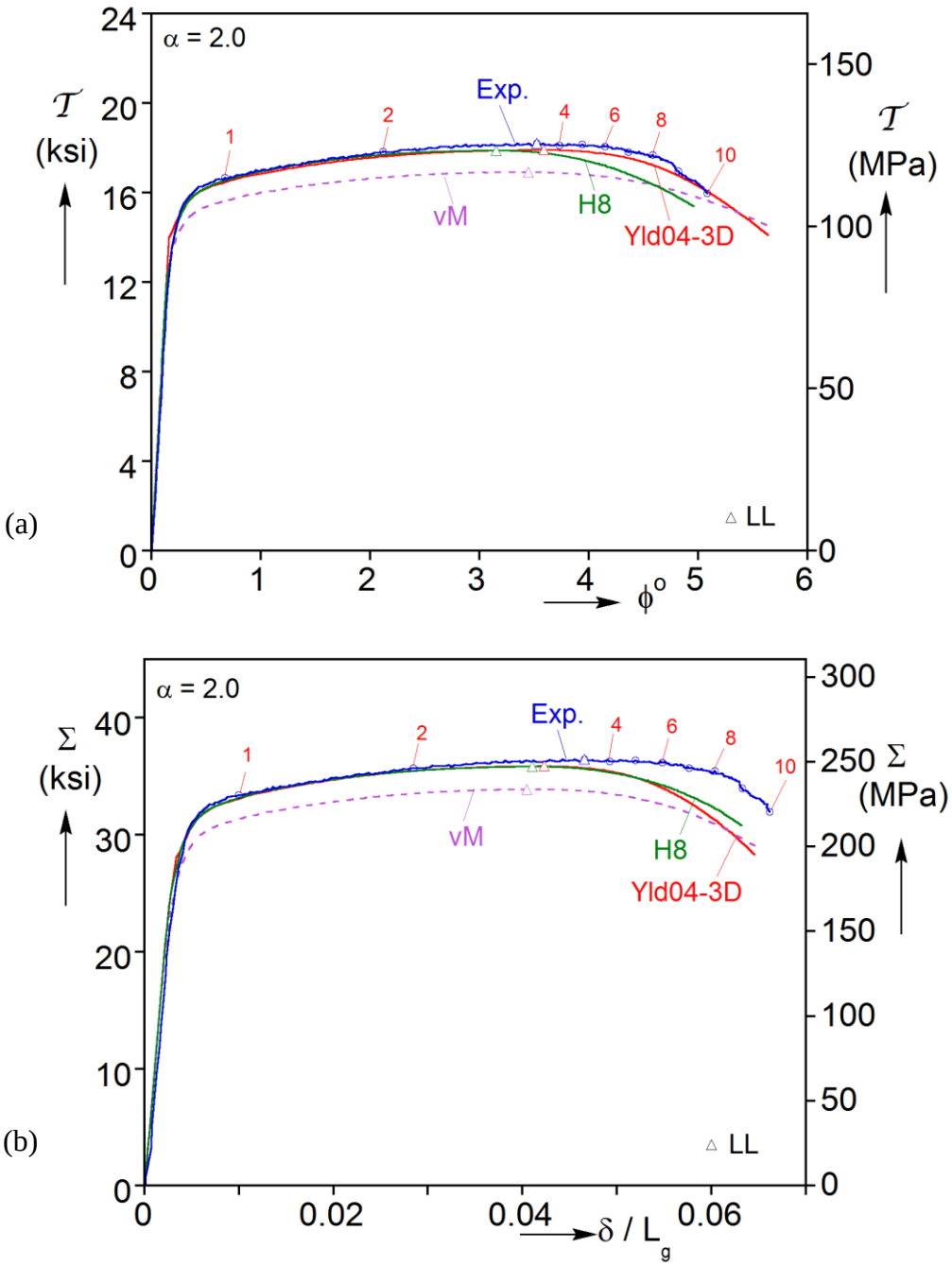

Fig. 5.7 Comparison of measured and predicted responses using three different constitutive models for $a = 2.0$. (a) Shear stress-rotation and (b) axial stress-elongation.

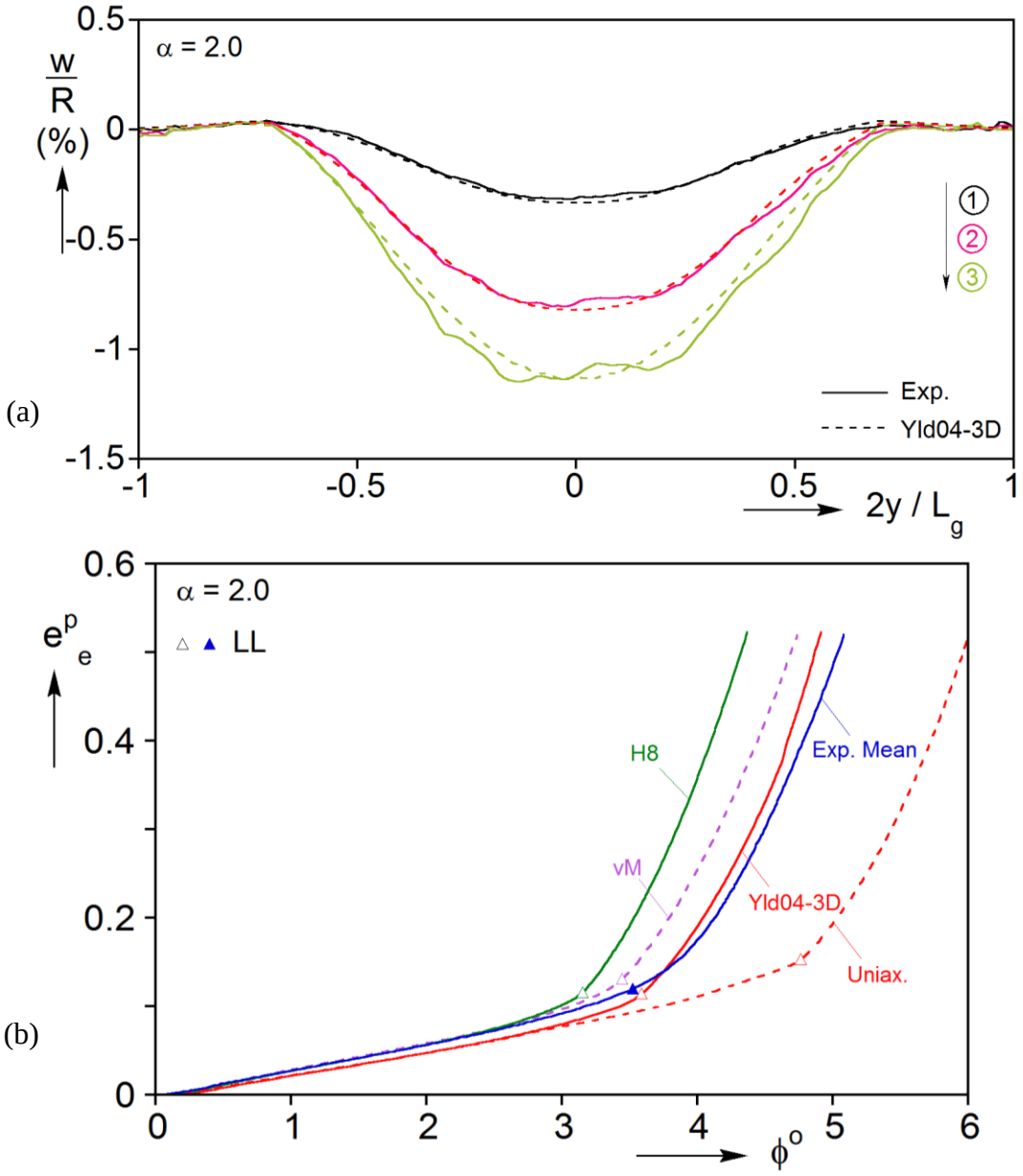

Fig. 5.8 (a) Comparison of measured and calculated radial displacement profiles across the length of the test section for $a = 2.0$, for the first three stations marked in Fig. 5.7. (b) Measured *Mean* equivalent plastic strain in the localizing zone vs. rotation for $a = 2.0$, and corresponding ones calculated using three different constitutive models. Included is the equivalent plastic strain predicted using the uniaxial stress-strain response.

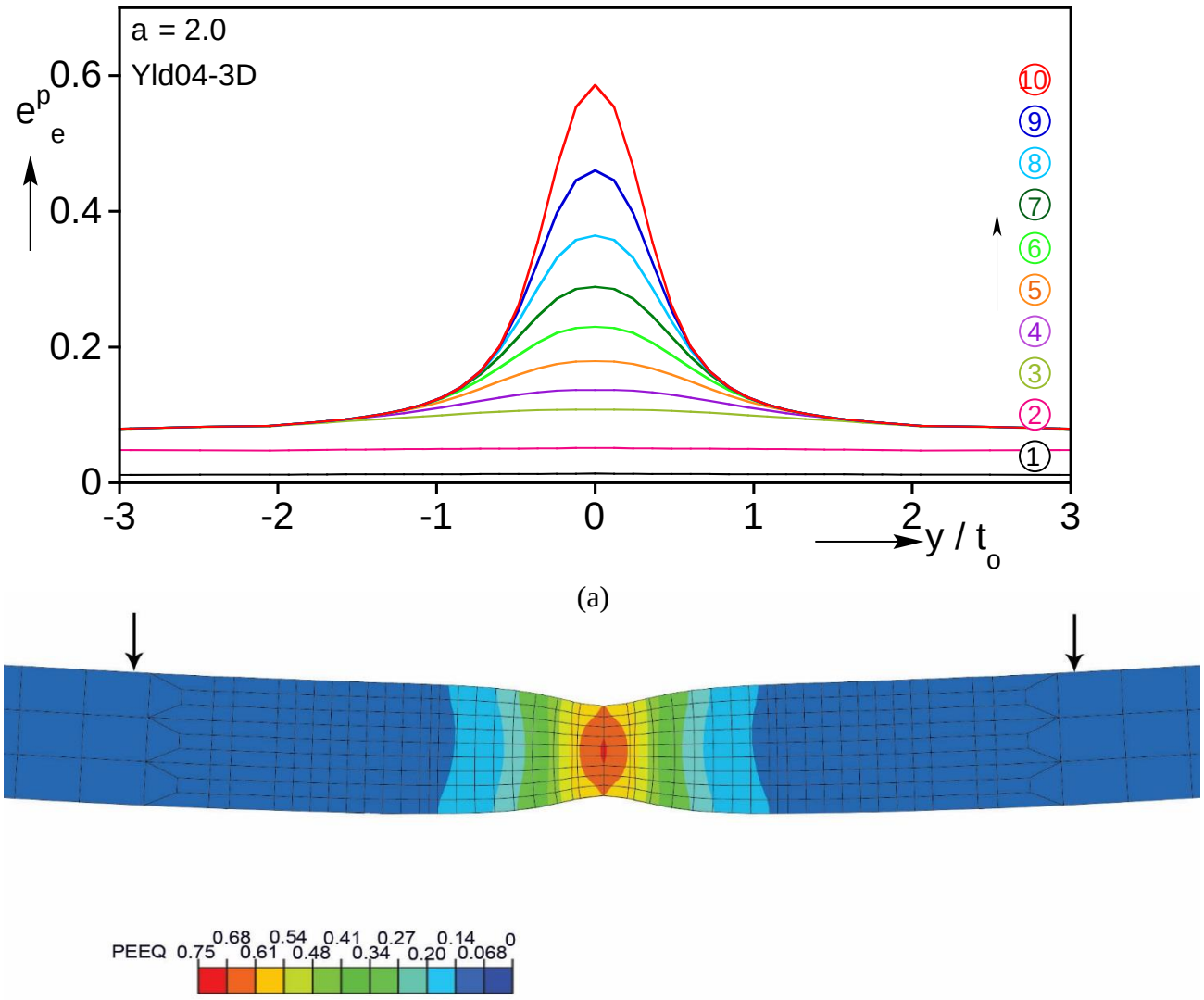

Fig. 5.9 (a) Calculated equivalent plastic strain profiles across the test section for $a = 2.0$, at rotations corresponding to those on the numbered stations in Fig. 5.7. (b) Through-thickness view of the plane of symmetry (mirrored) showing the necked region corresponding station ⑩ in Figs. 5.7 and 5.9a—arrows are $6t_o$ apart.

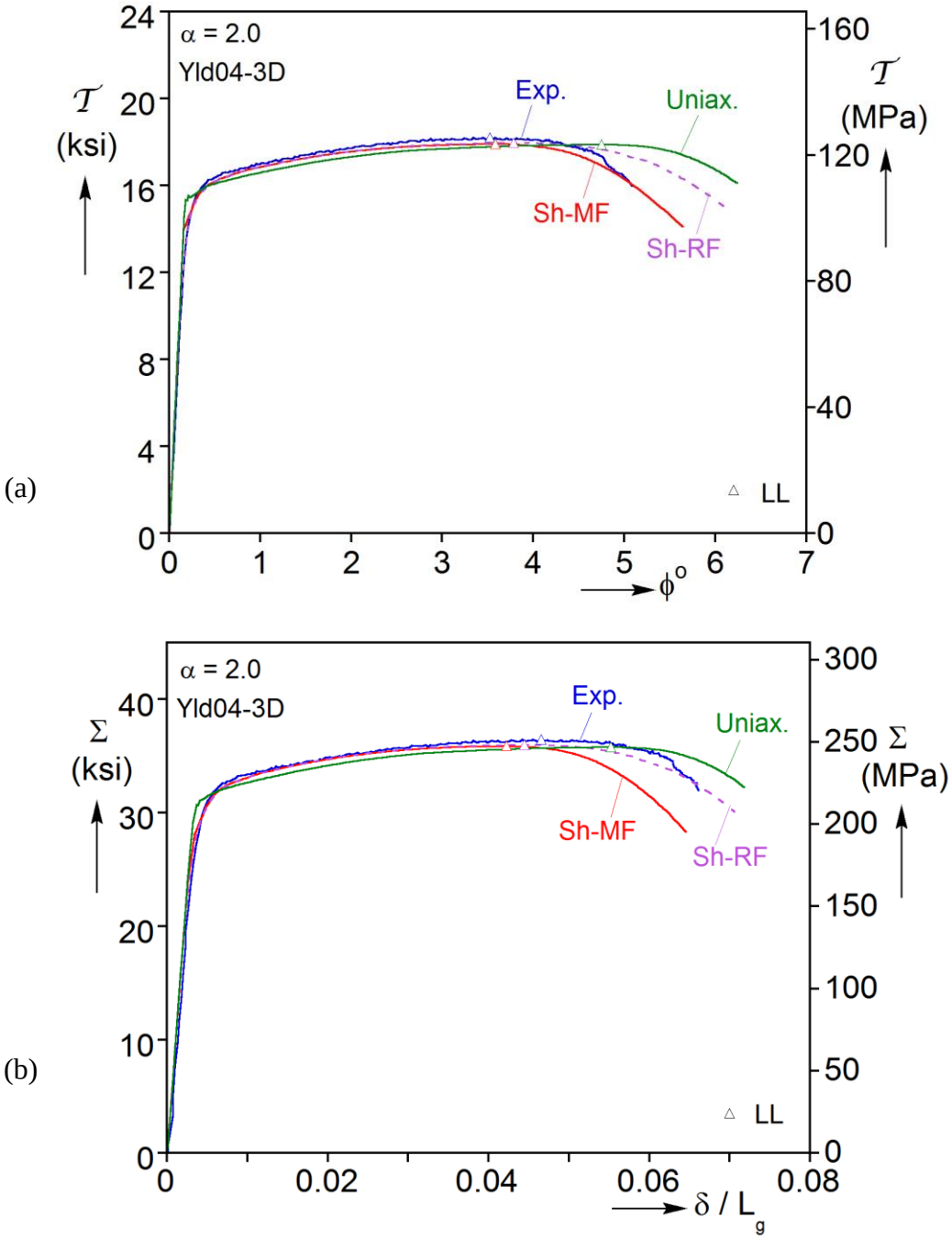

Fig. 5.10 Measured and predicted responses using the shear and uniaxial stress-strain responses for $a = 2.0$. (a) Shear stress-rotation and (b) axial stress-elongation.

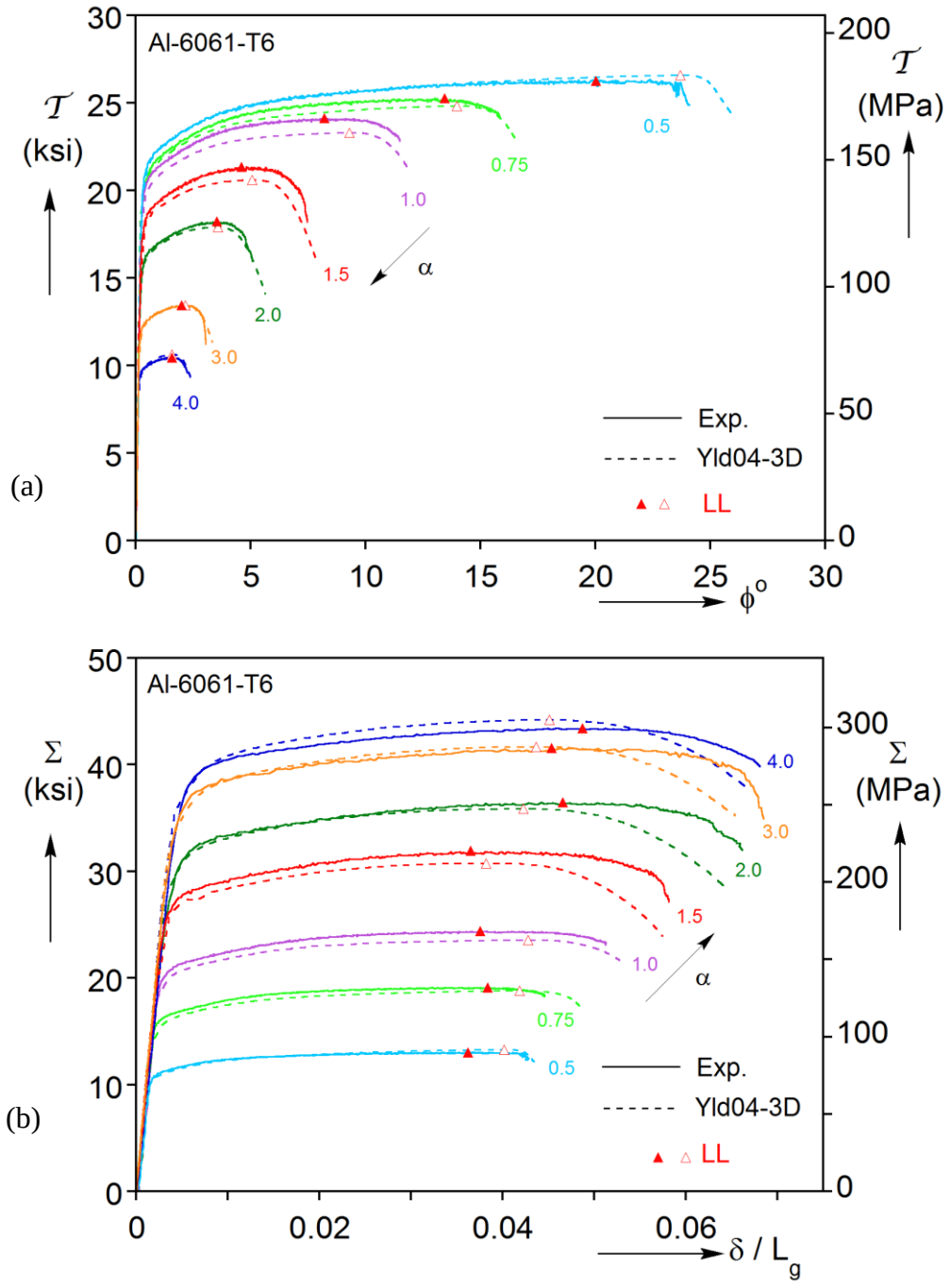

Fig. 5.11 Measured and predicted responses using the Yld04-3D constitutive model for the full set of radial path tension-torsion experiments performed. (a) Shear stress-rotation and (b) axial stress-elongation.

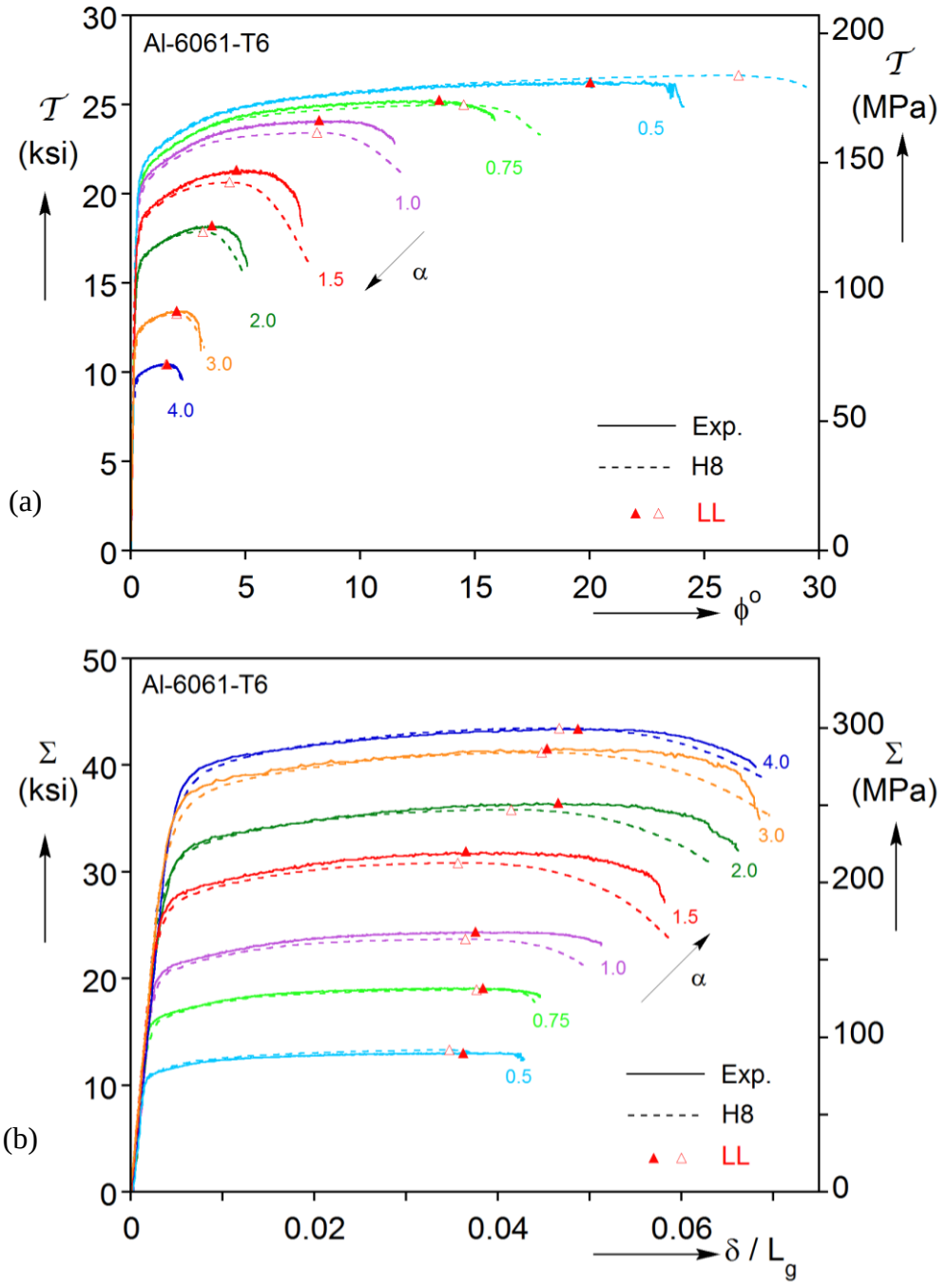

Fig. 5.12 Measured and predicted responses using the H8 constitutive model for the full set of radial path tension-torsion experiments performed. (a) Shear stress-rotation and (b) axial stress-elongation.

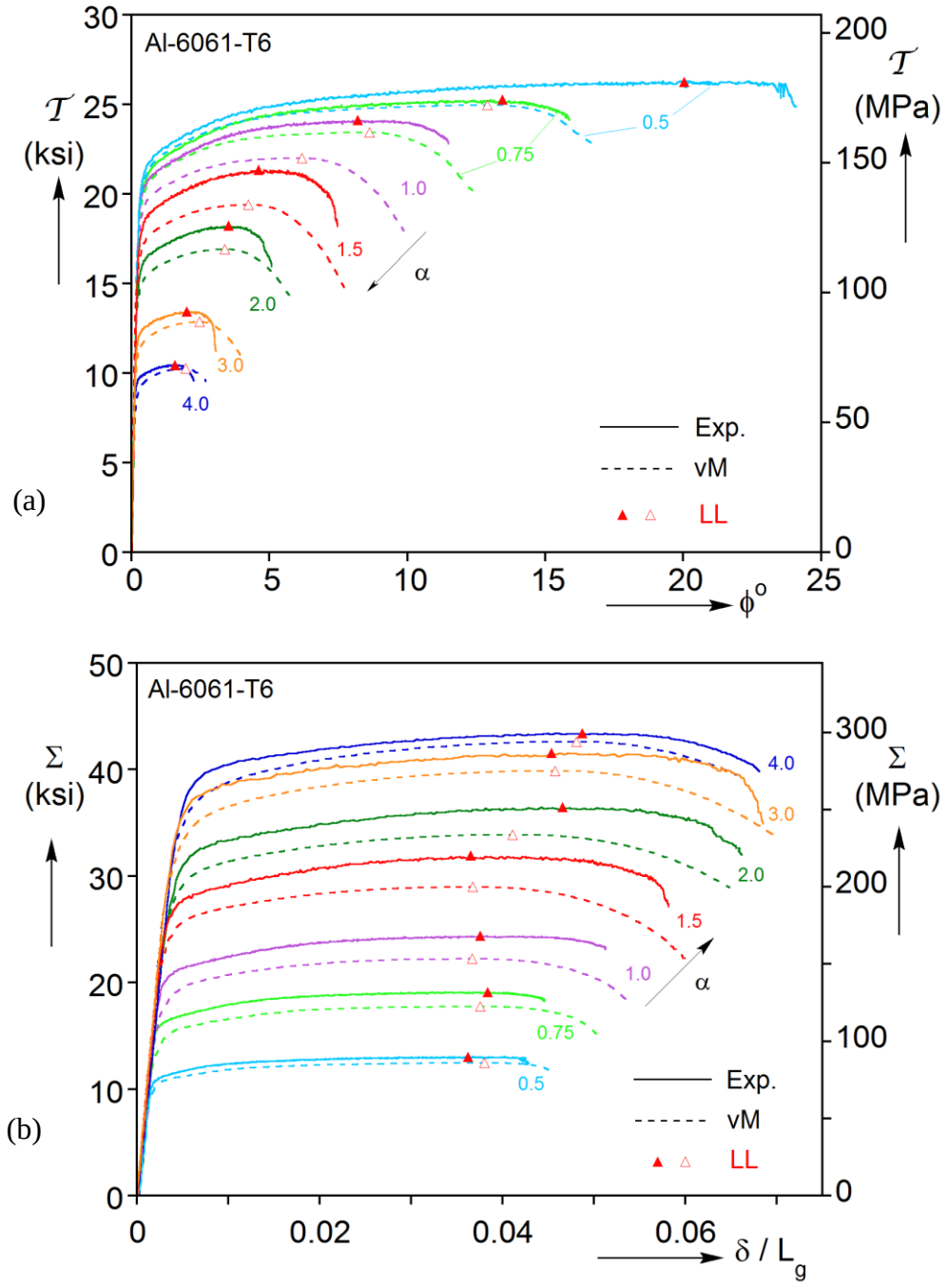

Fig. 5.13 Measured and predicted responses using the vM constitutive model for the full set of radial path tension-torsion experiments performed. (a) Shear stress-rotation and (b) axial stress-elongation.

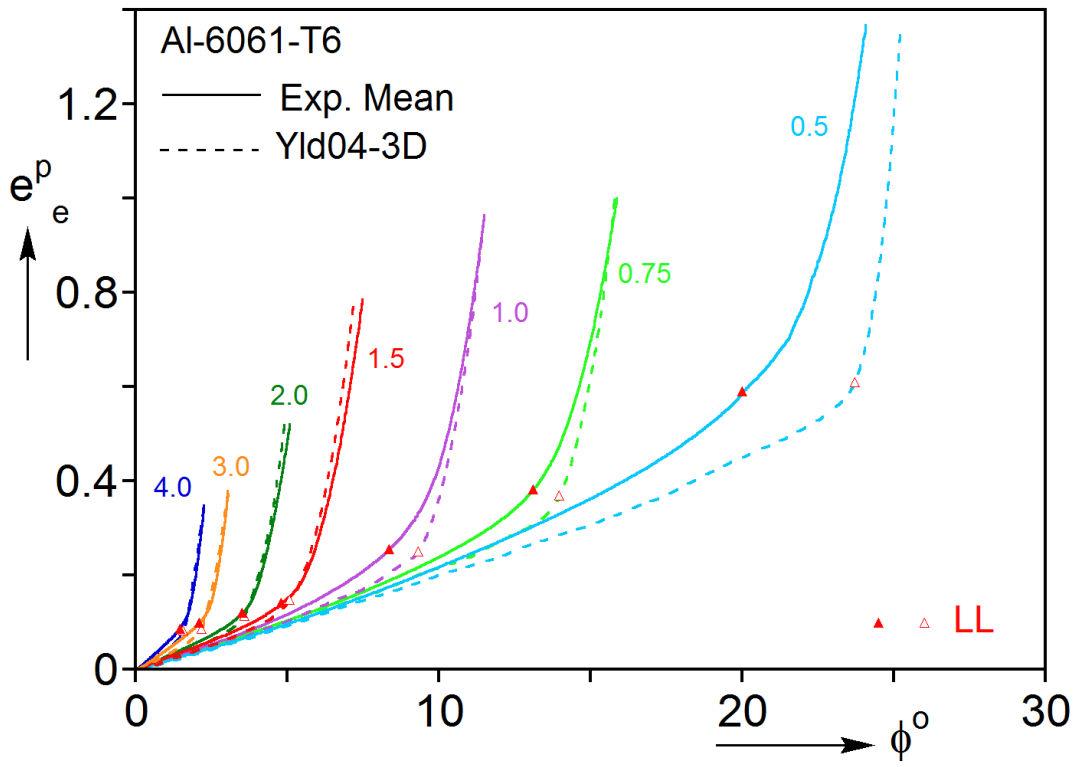

Fig. 5.14 Comparison of measured *Mean* equivalent plastic strain vs. rotation for full set of radial path experiments, and corresponding one calculated using Yld04-3D constitutive model.

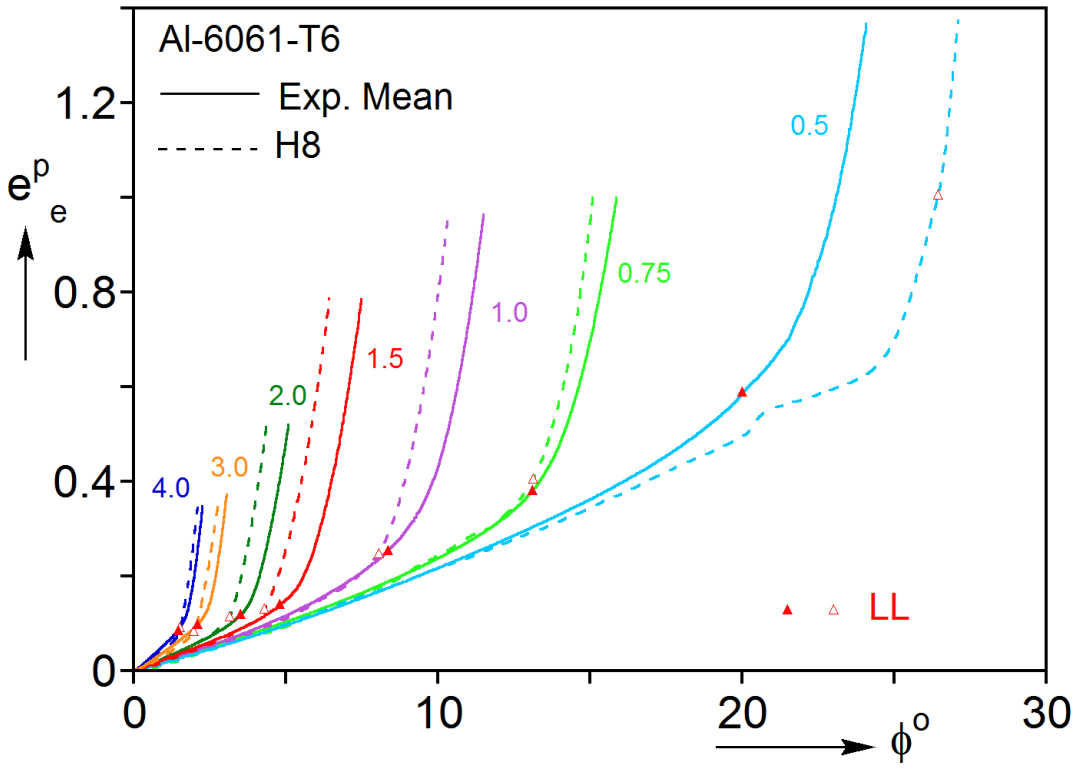

Fig. 5.15 Comparison of measured *Mean* equivalent plastic strain vs. rotation for full set of radial path experiments, and corresponding one calculated using H8 constitutive model.

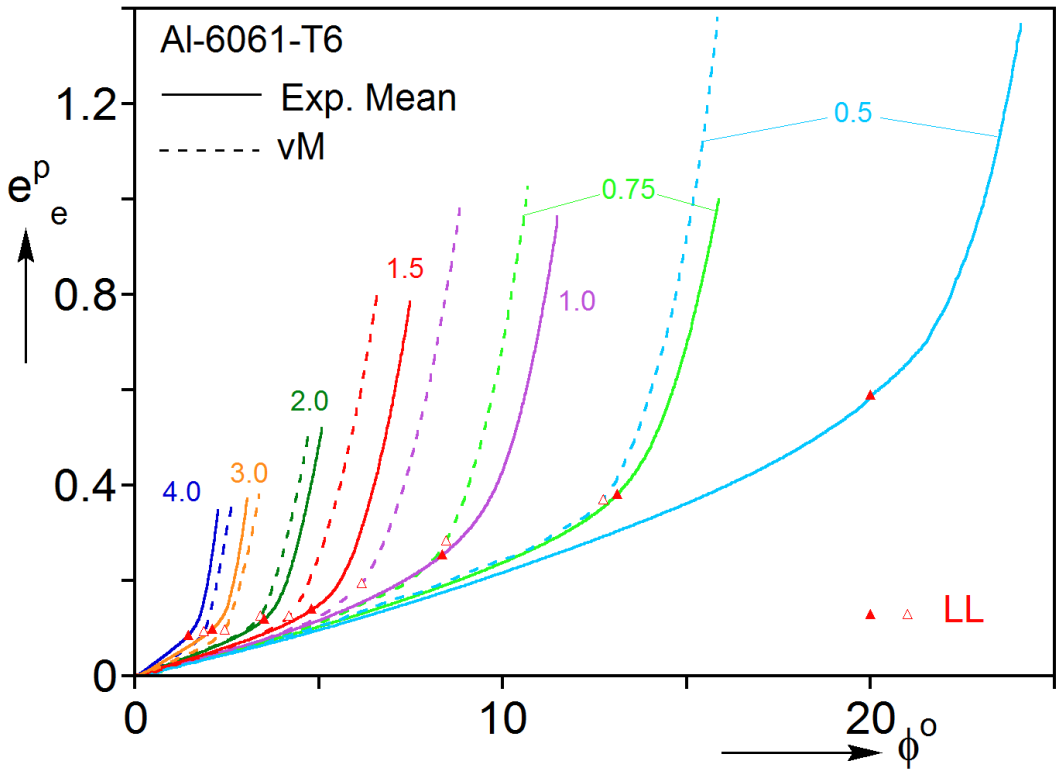

Fig. 5.16 Comparison of measured *Mean* equivalent plastic strain vs. rotation for full set of radial path experiments, and corresponding one calculated using vM constitutive model.

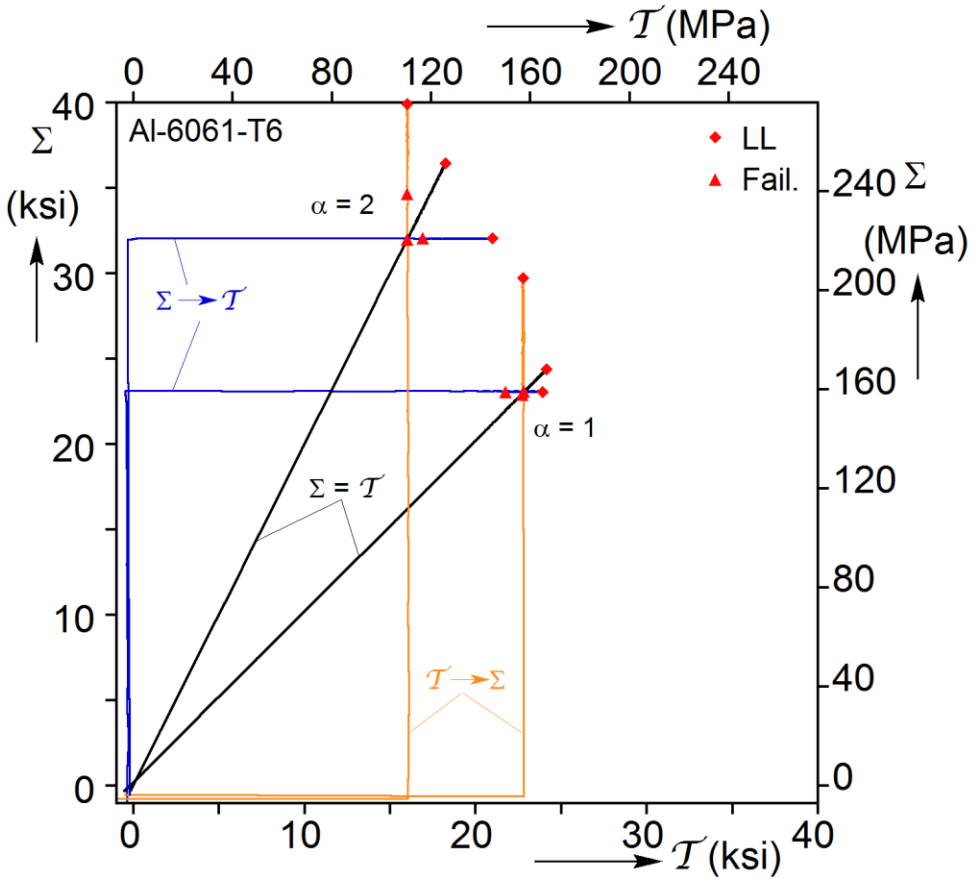

Fig. 5.17 Nominal axial-shear stress paths for the two sets of radial and corner path experiments with $a = 1.0$ and $a = 2$. The limit load is marked by ◆ and failure by ▲ (Scales et al. [2019]).

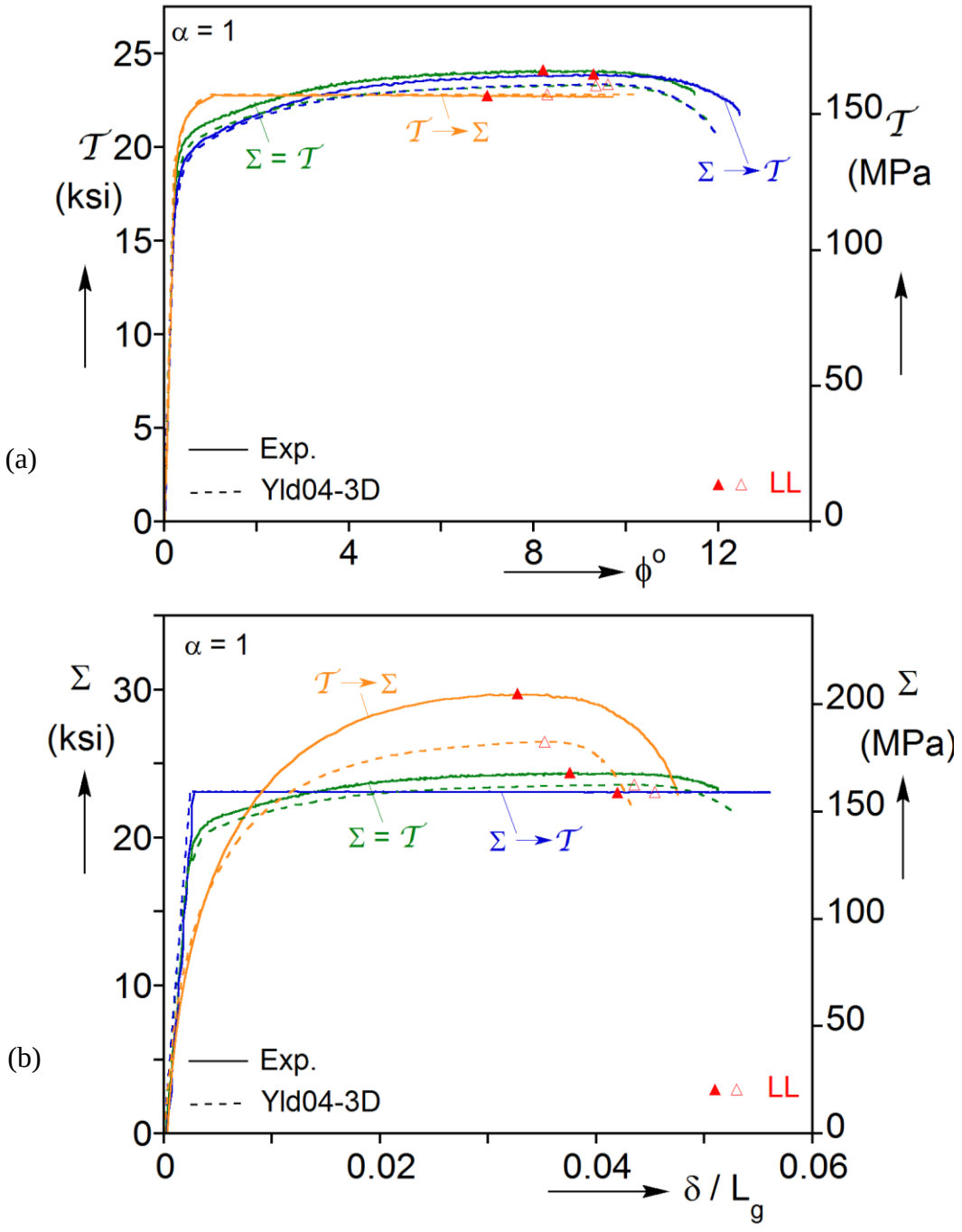

Fig. 5.18 Comparison of measured and calculated responses using Yld04-3D for the set of radial and corner path experiments with $a = 1.0$. (a) Shear stress-rotation and (b) axial stress-elongation.

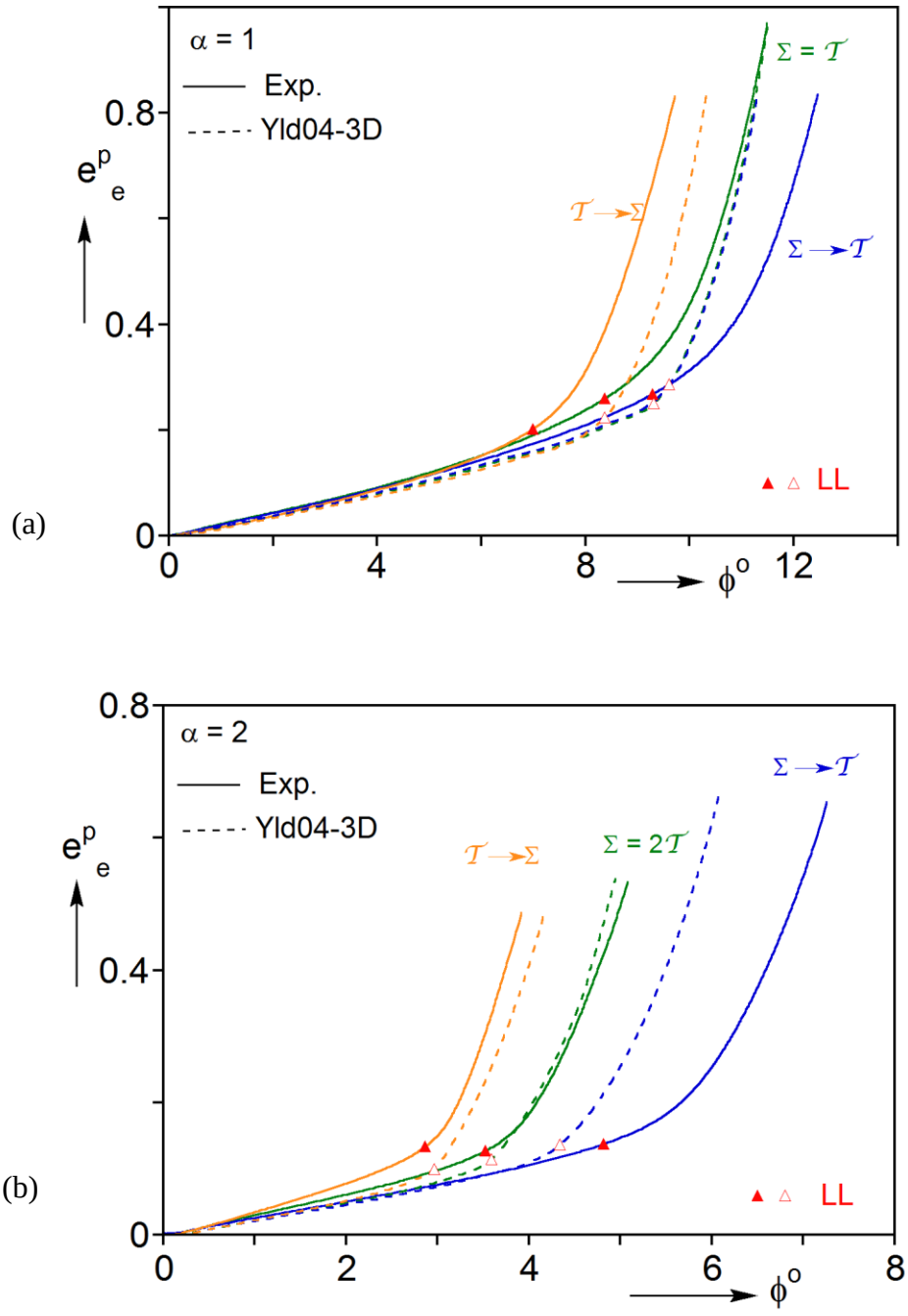

Fig. 5.19 Comparison of measured *Mean* equivalent plastic strain vs. rotation for the radial and corner paths and corresponding one calculated using Yld04-3D constitutive model. (a) $a = 1.0$ and (b) $a = 2.0$.

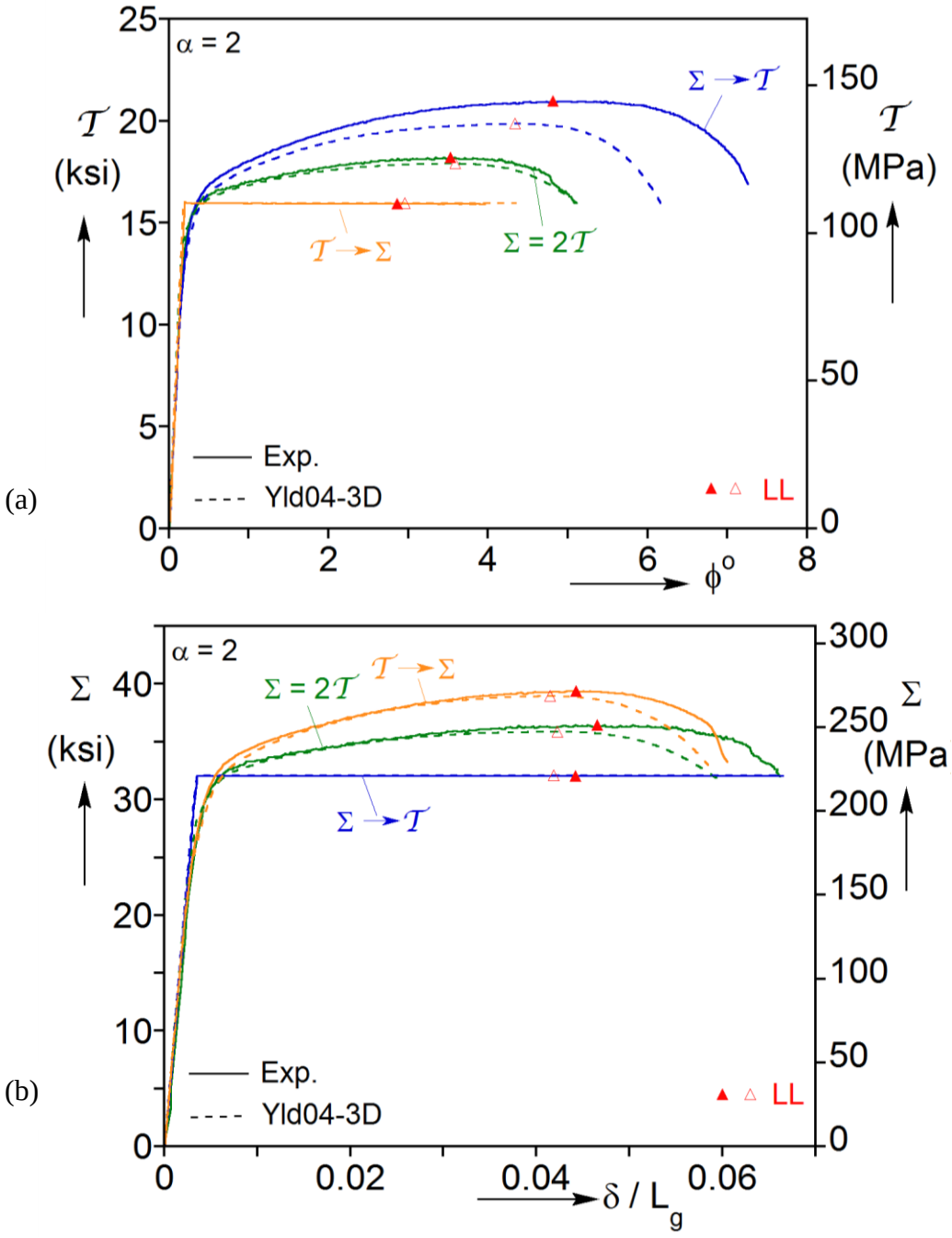

Fig. 5.20 Comparison of measured and calculated responses using Yld04-3D for the set of radial and corner path experiments with $a = 2.0$. (a) Shear stress-rotation and (b) axial stress elongation.

Chapter 6: Conclusions and Future Work

Despite progress achieved over the last 50 years, ductile failure in thin-walled structures using sheet metal or tubes, remains a challenge. The occurrence of localized deformation and its evolution that precede failure complicate the stress and strain analysis as failure approaches. Successful analysis of such large deformations requires careful constitutive modeling of sheet metals coupled to appropriate numerical schemes. This dissertation shows that important steps towards improving the prediction of failure in thin-walled structures are: (a) the adoption of advanced non-quadratic constitutive models capable of capturing the anisotropy of thin-walled Al-alloys; and (b) a reliable material hardening response to strains that are large enough to capture those measured at failure in experiments. This work has demonstrated the need of these innovations in two families of problems: the simulation of bulge tests in thin-walled Al-alloys sheets, and the analysis of a set of tension-torsion experiments on thin-walled tubes taken to failure. This Chapter presents the major findings and conclusions derived from each of the two parts of this work.

6.1 Hydraulic Bulge Tests

The hydraulic bulge test has long been used as an alternative to the uniaxial test for extracting the material hardening of sheet metal. The nearly equibiaxial state of stress at the bulge apex delays localization and with the strain remaining uniform up to a level that is much larger than that of a conventional uniaxial tension test. Furthermore, the bulge test is often used in the calibration of anisotropic yield functions by providing the yield stress and R-value under equibiaxial loading. However, successful extraction of the material hardening requires also accurate characterization of the anisotropy that typically exists in sheet metal.

Bulge tests were conducted using Al-2024-T3 and Al-6022-T43 sheets. The anisotropy in each sheet was established using a set of independent experiments used to calibrate the Yld-04-3D anisotropic yield function. The calibrated yield function was used to establish the material hardening. Each constitutive model and corresponding material hardening were incorporated in 3-D finite element models of the bulge tests and used to simulate the tests. The following are the main findings and conclusions drawn from these studies.

- Extraction of the stress state of an anisotropic material from the bulge apex depends on the yield function adopted. Nevertheless, the appropriate yield function that best describes the constitutive behavior of the material requires calibration with stress and strain state from the apex. Thus the calibration of material anisotropy and the extraction of material hardening are coupled.
- Without assuming an equibiaxial state of stress or strain a priori, an iterative scheme was proposed for calibrating the material anisotropy and extracting the material hardening simultaneously. The calibration used stress and strain data from seven uniaxial tension tests, three plain strain tension tests and the bulge test itself. The material hardening response was extracted for three yield functions: von Mises, Hosford (exponent 8) and Yld04-3D. The hardening response based on Yld04-3D, differs from those from the other two isotropic yield functions, even though the anisotropy of the materials tested was modest. The maximum equivalent strain extracted from each bulge test is about twice as large as the one from the uniaxial tension test.
- The commonly used Swift and Voce extrapolations based on uniaxial tension tests were compared with the ones extrapolated from the bulge tests. For both materials tested, Al-2024-T3 and Al-6022-T43, the Swift extrapolation overestimates the

hardening and the Voce one underestimates the hardening. The difference becomes more significant as the strain grows.

- The simulation of the bulge tests involved two models: a model in which the edge of the disk is fixed, and a more realistic model that better mimics the clamping process and allows for possible slipping over the draw-bead during the bulging process. The draw-bead model was found to match the measured pressure-height responses better than the fixed-end model. It was also shown that increasing the friction coefficient tends to decrease the maximum pressure and increase the corresponding limit strain at the apex.
- Overall, the pressure vs. volume and pressure vs. height responses before the pressure maxima were found not to be very sensitive to the yield function adopted. However, the localized deformation after the limit load and the ensuing burst pressure, especially when an imperfection band is present at the apex, significantly depends on the yield function adopted and the magnitude of the imperfection.
- Numerical simulation of the bulge test of the more ductile Al-6022-T43 reproduced the diffused localization behavior in bulge tests very well, where beyond the limit load the local equivalent strain away from the apex continues to grow but the growth rate decreases as the radial distance from the apex increases.

6.2 TENSION-TORSION OF THIN-WALLED TUBES

An experimental study on the ductile failure of Al-6061-T6 thin-walled tubes under combined tension and torsion, conducted in parallel with this work, has shown that significant localized deformation precedes rupture of the thin-walled test specimens. The strain level inside of the localization zone reached over 100% for low triaxiality cases. Despite such large strains, X-ray tomography and microscopic observations showed that

void growth was limited to the very end of material life. These observations prompted the second part of this study, which had as main goal to investigate the extent to which the structural response and evolution of localized large deformation could be reproduced within the framework of conventional, damage-free plasticity. The non-quadratic yield function Yld04-3D was adopted in numerical simulation of sets of radial and corner path tension-torsion experiments. For comparison purpose, the isotropic von Mises (vM) and Hosford with exponent of 8 (H8) were also used in the simulations. This work showed that successful modeling requires a thorough calibration of material anisotropy and a carefully extracted material hardening curve to large strains. Some key aspects of this effort and major conclusions are listed as follows:

- The anisotropic yield function Yld04-3D was calibrated using a uniaxial tension test, a pure shear test, seven radial path tension-torsion experiments and seven pressure-tension experiments. Stresses and strain ratios at plastic work of 1000 psi were used in the calibration, which involved minimization of an error function. The tension-torsion experiments showed that the test section developed a small amount of radial contraction. Including this contraction in an approximate manner was necessary for a more accurate calibration of the anisotropy.
- The material hardening response was extracted from a pure torsion test, where the maximum uniform equivalent strain reached 60%. To incorporate the calibrated anisotropy in the hardening extraction, it was found essential to account for the effect of material frame rotation and extract the hardening response in the material frame. For the Al-alloy tested, the hardening response in the material frame deviates from the reference frame beyond equivalent strain of about 10% and exhibits much smaller tangent modulus at larger strains. This difference in modulus was demonstrated to influence the onset of localization significantly.

- The corresponding material hardening curves for von Mises and Hosford-8 were also extracted from the pure torsion test. Because of the isotropic nature of the yield functions, their hardening responses are independent of material frame rotation. The two hardening responses exhibit higher hardening and trace lower stress levels than the response of Yld04-3D.
- The Yld04-3D hardening curve was also extracted from a uniaxial tension test using an inverse method. It was found to exhibit similar hardening as the one from the simple shear test but terminated at a strain of 35%.
- The Yld04-3D, von Mises and Hosford-8 yield functions together with the corresponding hardening curves were implemented in 3-D finite element models used to simulate the tension-torsion experiments. The Yld04-3D model was found to reproduce the experimental results much better than von Mises, and overall better than Hosford-8. This includes the overall structural responses, the radial contraction of the test section, and the evolution of localized deformation up to the point when rupture occurred in the experiments.
- Simulation of select experiments based on the reference frame simple shear hardening response was also performed. Localization was found to occur at significantly larger strain levels due to the stiffer hardening response.
- The onset of instability under combined tension and torsion was established analytically based on Considère type analysis. The results were found to be in good agreement with the limit loads established numerically. This success indicates that this type of analysis can be a useful tool in structural design. This level of performance again requires an accurate representation of material hardening appropriate for the yield function adopted.

6.3 FUTURE WORK

Several of the analyses and numerical schemes used in the calibration of anisotropy, the extraction of the material hardening, and the numerical simulation of structural responses that lead to failure can either be extended, improved or substituted with alternative schemes. Listed below are several issues that could be further developed in future investigations.

- An iterative scheme was proposed to extract the material hardening from circular hydraulic bulge tests. In the literature, elliptical bulge tests have also been used to extract material hardening responses from sheet metals. The proposed scheme can be extended to elliptical bulge tests, which could provide an alternative method of material hardening extraction and useful experimental data for anisotropy calibration.
- In the calibration of Yld04-3D yield function for Al-6061-T6 tubes, only data from radial path experiments were used in the calibration. As the numerical simulation shows, the corner path structural responses for $\alpha = 1.0$ is not as good as those for the radial paths. It is suggested the inclusion of corner path experiments in the calibration could make the calibration more robust and more representative.
- The parallel experimental study of the combined tension-torsion tests could only cover a triaxiality range of 0 to 0.577. To increase the span of triaxiality, hydraulic bulge tests or pressure-tension tests can be used to increase the maximum triaxiality to 0.667 for 2D state of stress. A higher triaxiality requires 3-D state of stress such as tension-torsion of notched thick-walled tubes, where numerical simulation must be used to determine the stress and strain states at failure.
- The numerical simulations of the tension-torsion experiments reproduced the structural responses and evolution of localized deformation well up to the rupture of specimens. Termination of the numerical analysis requires a failure criterion. The

experimental results from Scales et al. [2019] can be used directly to establish a failure criterion for this Al-alloy. Stress and strain histories of critical elements in the FE model can be extracted to establish the loading path to fracture for the elements. These results can be used to calibrate failure criteria such as the Johnson-Cook [1985] or the Hosford-Coulomb criteria (Mohr and Marcadet, 2015). The calibrated failure criterion can then be used in large-scale simulations of structures under extreme loading conditions to model material and structural failure.

Appendices

APPENDIX A: HILL'S BULGE INSTABILITY ANALYSIS

Hill's approximate but insightful analysis of a bulge test (Hill, 1950) is based on the assumption that it deforms into a spherical shape (see also Gleyzal [1948] for earlier approximate solution). It leads to the following relationship between the through thickness strain at the apex, e_t, the height of the bulge h and its polar radius ρ:

$$-e_t = \ln\left(\frac{t_o}{t}\right) = 2\ln\left(1+\frac{h^2}{R^2}\right), \tag{A.1a}$$

and

$$\frac{r}{R} = \left(1+\frac{h^2}{R^2}\right)\Big/\frac{2h}{R}. \tag{A.1b}$$

The equibiaxial state of stress at the apex relates the stress, t, to the instantaneous values of the variables through

$$\frac{2t}{r} = \frac{P}{t} \tag{A.2}$$

At $P_{\max}$

$$\frac{dt}{t} + \frac{dt}{t} - \frac{dr}{r} = 0 \tag{A.3}$$

For von Mises yielding,

$$t_e = t \text{ and } de_e = 2de = -\frac{dt}{t}. \tag{A.4}$$

Then from (A.3)

$$\frac{1}{t_e}\frac{dt_e}{de_e} = 1 + \frac{1}{r}\frac{dr}{de_e} \tag{A.5}$$

Using (A.1) in (A.5)

$$\frac{1}{t_e}\frac{dt_e}{de_e} = \frac{3}{2} - \frac{r}{2h} \tag{A.6}$$

Expanding r/h in terms of e_e, leads to the following approximate expression for the critical state

$$\frac{1}{\tau_e}\frac{d\tau_e}{de_e} \approx \frac{11}{8} - \frac{1}{2e_e} \tag{A.7}$$

Using the material response of Al-6022-T43 extracted from the bulge test as shown in Fig. 2.12b, equation (A.7) results in a critical strain of 0.44, which compares with 0.528 measured in the experiment. This value compares with the limit strain of 0.54 produced by the complete bulge numerical analysis. This difference is of course caused by the approximate nature of Hill's closed form solution.

For completeness, the Swift and Voce extrapolations of the measured uniaxial response of Al-6022-T43 were implemented in (A.7) in conjunction with the von Mises yield criterion. The calculated critical strains are 0.54 for Swift and 0.40 for Voce. The critical strains are marked on the corresponding stress-strain responses with sold bullets in Fig. 2.12b. As expected they deviate significantly from the measured value.

APPENDIX B: EFFECT OF SLIPPING

Figure B.1 shows a failed bulge test specimen that experienced slipping at the draw bead during the initial development of our bulge test facility. The slipping is unsymmetric and is much more pronounced at the lower end where wrinkles developed.

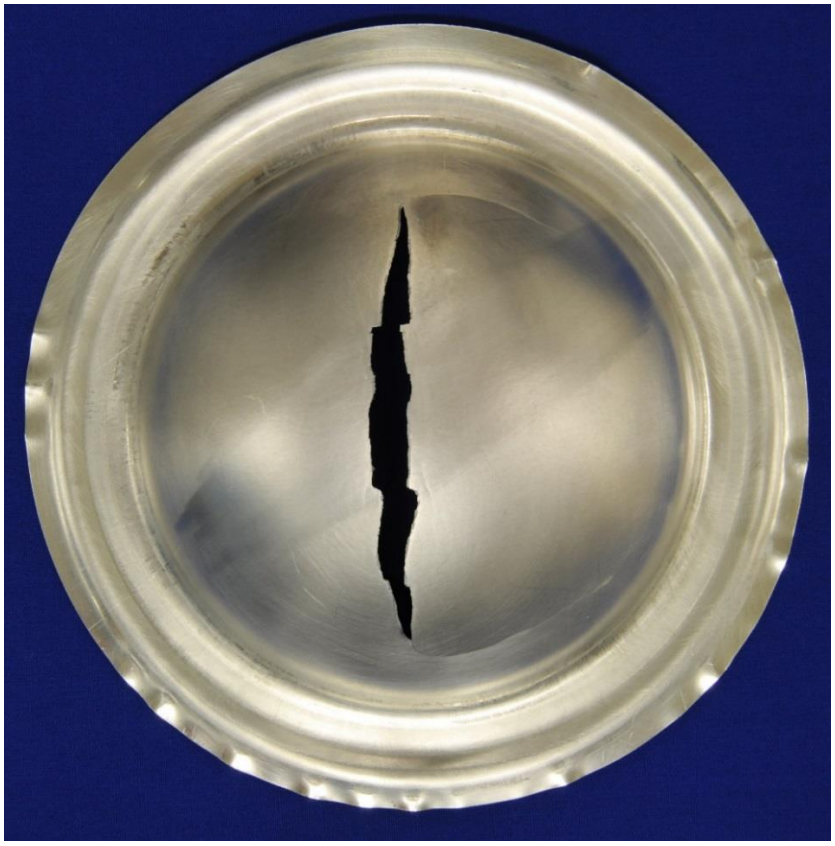

Fig. B.1 A bulge test specimen that experienced asymmetric slipping.

APPENDIX C: ESTIMATION OF HOOP STRESSES

In the tension-torsion radial path experiments, the test section develops a small amount of curvature that depends on the level of tension applied (e.g., see Fig. 8 in Scales et al. [2019]), or the ratio a, which complicates the stress and strain state in the test section. The hoop stress is assumed to be proportional to the axial stress through

$$s_{11} = bs_{22}. \tag{C.1}$$

For values of $a \le 1.5$, the curvature developed in the axial direction is quite small. Thus b is estimated using Hosford's isotropic yield function (4.1) in the flow rule to determine the following strain ratio:

$$R = \frac{d\varepsilon_{11}^p}{d\varepsilon_{22}^p} = \frac{\partial \Phi_{H8} / \partial \sigma_{11}}{\partial \Phi_{H8} / \partial \sigma_{22}} = f(\alpha, \beta). \tag{C.2}$$

$f(a,b)$ is assigned the hoop-axial strain ratio measured in the experiment in the crest of the axial curvature at the stress levels associated with $W^p = 1000$ psi. Since a is known, b is evaluated from (C.2) numerically.

For $a > 1.5$, the axial curvature that develops is more significant. Let r_2 and r_1 be the measured radii of curvature in the axial and hoop direction respectively at the test section mid-height. We assume that this part of the test section is in membrane state of stress, which then satisfies the membrane equilibrium equation

$$\frac{s_{11}}{r_1} - \frac{s_{22}}{r_2} = 0. \tag{C.3}$$

Eq. (C.3) readily yields

$$b = \frac{s_{11}}{s_{22}} = \frac{r_1}{r_2}. \tag{C.4}$$

The estimated values of b for the seven tension-torsion radial paths and the "plane-strain" experiments are listed in Table C1.

Table C1 Estimated values of the hoop-axial stress ratio, β for various values of α

a	0.5	0.75	1.0	1.5	2.0	3.0	4.0	∞
b	0.60	0.47	0.39	0.32	0.25	0.23	0.21	0.19

APPENDIX D: MATERIAL HARDENING EXTRACTION FROM SIMPLE SHEAR TESTS USING THE HILL48 MODEL

It has been well-established that the material hardening response is influenced by the constitutive model adopted (e.g., see Tardif and Kyriakides, 2012; Chen et al., 2018a; Kang et al., 2008). In Chapter 4, eight shear-tension tests of varying stress ratios and seven pressure-tension tests were used to quantify the anisotropy of Al-6061-T6 using the non-quadratic Yld04-3D model (Barlat et al., 2005) with an exponent of 8. The material hardening response was extracted from a pure torsion experiment. In such a test, the material axes rotation was found to play a crucial role in determining the hardening responses of anisotropic materials. In order to facilitate a simple study of the sensitivity of the extracted hardening response to the anisotropy parameters, the quadratic Hill-1948 (H-48, see Hill [1948]) anisotropic yield function is adopted to extract the hardening response from the same pure torsion experiment described in Scales et al. [2019]. In particular, the measured shear stress-plastic strain response for the Al-6061-T6 tubes analyzed, as shown in Fig. 4.7, is used in the hardening extraction with H-48 yield function.

For the present stress state H-48 can be written as:

$$\sigma_e = \left[\sigma_{11}^2 - \left(1 + \frac{1}{S_2^2} - \frac{1}{S_3^2} \right) \sigma_{11}\sigma_{22} + \frac{1}{S_2^2}\sigma_{22}^2 + \frac{3}{S_{12}^2}\sigma_{12}^2 \right]^{1/2} \tag{D.1a}$$

where S_{ij} are the ratios of the following yield stresses:

$$S_2 = \sigma_{2o} / \sigma_{1o},\ S_3 = \sigma_{3o} / \sigma_{1o},\ S_{12} = \sqrt{3}\sigma_{12o} / \sigma_{1o}. \tag{D.1b}$$

For the narrow purposes of the present study, the same experimental data used in the calibration of Yld04-3D, i.e., the yield stresses and R-values of a uniaxial tension test, a simple shear test, seven tension-torsion tests and seven pressure-tension tests at plastic work of 1000 psi (6.897 MPa) as described in Section 4.2.1, are used to also calibrate the

quadratic H-48 anisotropic yield function. S_{ij} were determined by minimizing the sum of set of weighted error functions as in Eq. (4.29) for all experiments. The process produced the following values for the anisotropy parameters

$$S_2 = 1.01,\ S_3 = 0.97,\ S_{12} = 0.93$$

As expected, the calibration of aluminum alloys with quadratic yield functions is not ideal, but the parameters above are adequate for demonstrating the effect of material frame rotation on the extracted material response. For simple shear test, the incremental spin tensor can be obtained from deformation gradient tensor as:

$$d\boldsymbol{\omega} = skewsym(d\boldsymbol{F}\boldsymbol{F}^{-1}) = \begin{bmatrix} 0 & d\gamma/2 & 0 \\ -d\gamma/2 & 0 & 0 \\ 0 & 0 & 0 \end{bmatrix}, \tag{D.2a}$$

which integrates to

$$\boldsymbol{\omega} = \begin{bmatrix} 0 & \gamma/2 & 0 \\ -\gamma/2 & 0 & 0 \\ 0 & 0 & 0 \end{bmatrix}. \tag{D.2b}$$

Thus, the transformation tensor for the material frame becomes

$$\boldsymbol{A} = \begin{bmatrix} \cos\gamma/2 & -\sin\gamma/2 & 0 \\ \sin\gamma/2 & \cos\gamma/2 & 0 \\ 0 & 0 & 1 \end{bmatrix}. \tag{D.3}$$

The stress, when expressed in the material frame, is then:

$$\boldsymbol{\sigma}' = \boldsymbol{A}\sigma\boldsymbol{A}^T = \tau \begin{bmatrix} -\sin\gamma & \cos\gamma & 0 \\ \cos\gamma & \sin\gamma & 0 \\ 0 & 0 & 1 \end{bmatrix}. \tag{D.4}$$

For the anisotropic material in Eq. (D.1), the equivalent stress in the material frame then becomes

$$s_e = s_e(s_{ij}, S_2, S_3, S_{12}), \tag{D.5a}$$

or
$$\sigma_e = \tau \left[\frac{3}{S_{12}^2} + \left(2 + \frac{2}{S_2^2} - \frac{1}{S_3^2} - \frac{3}{S_{12}^2} \right) \sin^2 2\theta \right]^{1/2}. \tag{D.5b}$$

This is used to evaluate the work compatible plastic equivalent strain increment from

$$d\varepsilon_e^p = \frac{\tau \, d\gamma^p}{\sigma_e}, \tag{D.6a}$$

which in the material frame becomes

$$d\varepsilon_e^p = \frac{d\gamma^p}{\left[\frac{3}{S_{12}^2} + \left(2 + \frac{2}{S_2^2} - \frac{1}{S_3^2} - \frac{3}{S_{12}^2} \right) \sin^2 2\theta^p \right]^{1/2}}, \tag{D.6b}$$

(the elastic component of γ is neglected). This integrates as an elliptic integral of the first kind. In the reference frame, on the other hand,

$$d\varepsilon_e^p = \frac{S_{12}}{\sqrt{3}} d\gamma^p, \tag{D.6c}$$

which integrates directly. If the material yields isotropically, (D.1) reduces to von Mises (vM), which is invariant to transformation and

$$\sigma_e\big|_{\text{vM}} = \sqrt{3}\,\tau, \tag{D.7a}$$

$$d\varepsilon_e^p\Big|_{\text{vM}} = \frac{d\gamma^p}{\sqrt{3}}, \tag{D.7b}$$

which also integrates directly. To facilitate a comparison with the quadratic yield functions, we include the equivalent stress for the isotropic Hosford yield function (Hosford, 1972) with exponent 8 (H8) which is given by

$$\sigma_e\big|_{\text{H8}} = (2^7 + 1)^{1/8} \tau, \tag{D.8a}$$

$$d\varepsilon_e^p\Big|_{\text{H8}} = \frac{d\gamma^p}{(2^7 + 1)^{1/8}}. \tag{D.8b}$$

The anisotropy parameters and the measured shear stress and strain values were used in Eqs. (D.5) and (D.6) to generate incrementally the equivalent stress-equivalent

plastic strain response of the material. It is referred to as the Material Frame (MF) response and is plotted in Fig. D.1. Included is the corresponding response when the rotation of the material frame is not accounted for—referred to as Reference Frame response (RF). Clearly, this particular anisotropy leads to progressive reduction in tangent modulus for equivalent strains larger than about 0.15. Such changes in modulus can have significant influence on the prediction of localization and other instabilities and the onset of failure.

Figure D.2 shows the equivalent stress-equivalent plastic strain responses corresponding to the isotropic von Mises and Hosford yield functions. Included is the reference frame response based on the Hill-48 anisotropic yield function. The three responses exhibit similar hardening, but trace different stress levels. The difference in stress level between vM and H-48 is caused by the anisotropy, whereas the difference between vM and H8 is due to the different exponent of the two yield functions.

We now conduct a limited parametric study to illustrate the effect of the anisotropy parameters, S_{ij}, on the extracted material response. The plastic tangent modulus of the Material Frame response is given by:

$$\left.\frac{d\sigma_e}{d\varepsilon_e^p}\right|_{\text{MF}} = \frac{d\tau}{d\gamma}\left[\frac{3}{S_{12}^2} + \left(2 + \frac{2}{S_2^2} - \frac{1}{S_3^2} - \frac{3}{S_{12}^2}\right)\sin^2\gamma\right] + \frac{\tau}{2}\left(2 + \frac{2}{S_2^2} - \frac{1}{S_3^2} - \frac{3}{S_{12}^2}\right)\sin 2\gamma \quad \text{(D.9a)}$$

By contrast in the Reference Frame tangent modulus is

$$\left.\frac{d\sigma_e}{d\varepsilon_e^p}\right|_{\text{RF}} = \frac{d\tau}{d\gamma}\frac{3}{S_{12}^2}. \quad \text{(D.9b)}$$

Comparing Eq. (D.9a) and (D.9b), it can be concluded that the term in the round brackets of (D.9a), which depends only on material anisotropic parameters, plays a crucial role in adjusting the hardening modulus in the Material Frame.

The measured τ - γ response is used together with Eqs. (D.1-D.6) to evaluate the Material and Reference Frame responses for various combinations of the three anisotropy

parameters. Figure D.3 shows results where each of anisotropy parameters is varied with the other two kept at 1.0. In Fig. D.3a S_{12} is assigned values of 0.95, 1.0 and 1.05. For $S_{12}=1.0$, the material is isotropic and the response coincides with that of vM in Eqs. (D.7). For $S_{12}=0.95$, both the RF and MF responses are higher than the isotropic one, but this value causes the tangent modulus of the MF response to be increasingly lower than that of the RF response. When $S_{12}=1.05$, both responses are lower than the isotropic one, but here the tangent modulus of the MF response becomes increasingly higher than that of the RF response.

In Fig. D.3b S_2 is assigned values of 0.95, 1.0 and 1.05. Making this parameter larger that 1.0 lowers the tangent modulus of the MF response and making it smaller increases it. In this case the RF response is the isotropic one. In Fig. D.3c S_3 is varied in a similar manner. This parameter has the opposite effect on the RF response: $S_3>1.0$ increases the MF tangent modulus while for $S_3<1.0$ decreases it. Here again the RF response is the isotropic one. It is worth noting that when the anisotropy term in the round brackets in Eq. (11a) is larger than zero the MF response tangent modulus is larger than that of the RF tangent modulus and when it is less than zero the opposite is true.

Figure D.4 shows additional comparisons of MF and RF responses for three more representative combinations of S_{ij} parameters for the same simple shear test. It is clearly demonstrated that the material frame rotation alters the response and must be accounted for. The decisive role of the anisotropy term in the round brackets in Eq. (D.9a) on the hardening modulus is demonstrated here too.

This Appendix demonstrated that as a consequence of the measured anisotropy in Al-6061-T6, the axes rotation progressively reduces the material tangent modulus as the strain increases. The simplicity of the H-48 yield function enabled evaluation of the sensitivity of the induced changes of the extracted response to the anisotropy parameters.

It is established that the material frame rotation that takes place in simple shear tests can influence the extracted response significantly when material anisotropy is accounted for, and consequently must be included in the analysis of such experiments. This conclusion also holds for alternate methods of characterizing the material anisotropy such as non-quadratic yield functions (e.g., Barlat et al. [2005]). It is worth pointing out that the results of the analysis presented are consistent with ABAQUS' incremental treatment of the material frame rotation (ABAQUS, 2016).

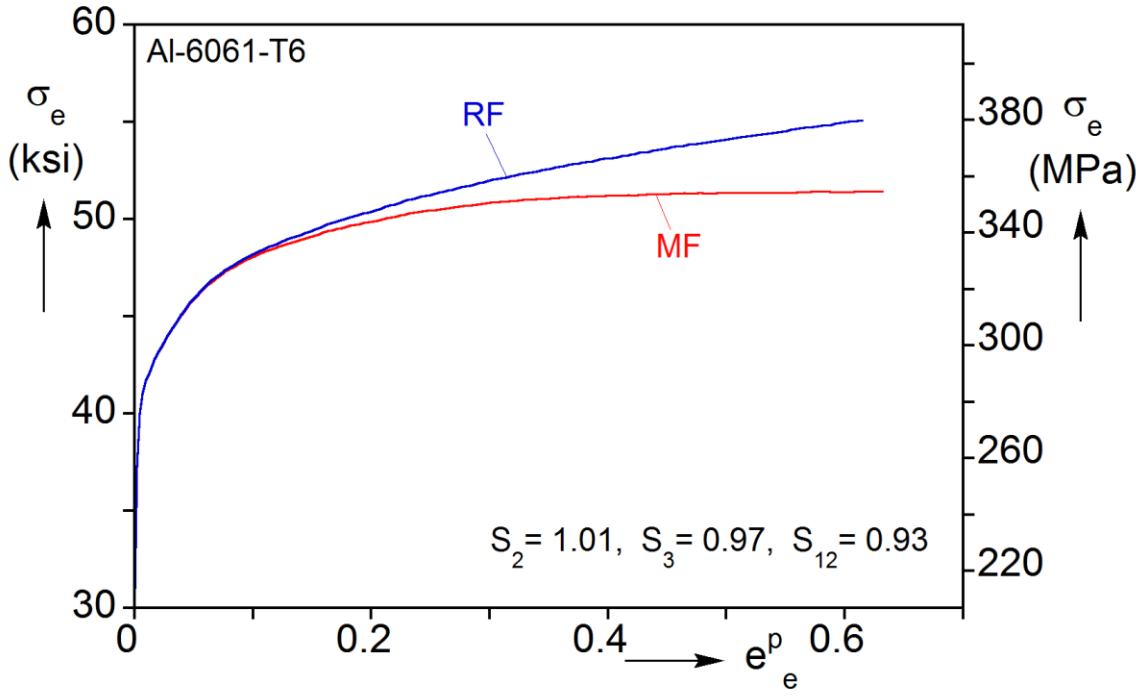

Fig. D.1 The Material and Reference Frame equivalent stress-equivalent plastic strain responses extracted from the measured t - g^p response. Included are the calibrated Hill-48 anisotropy constants.

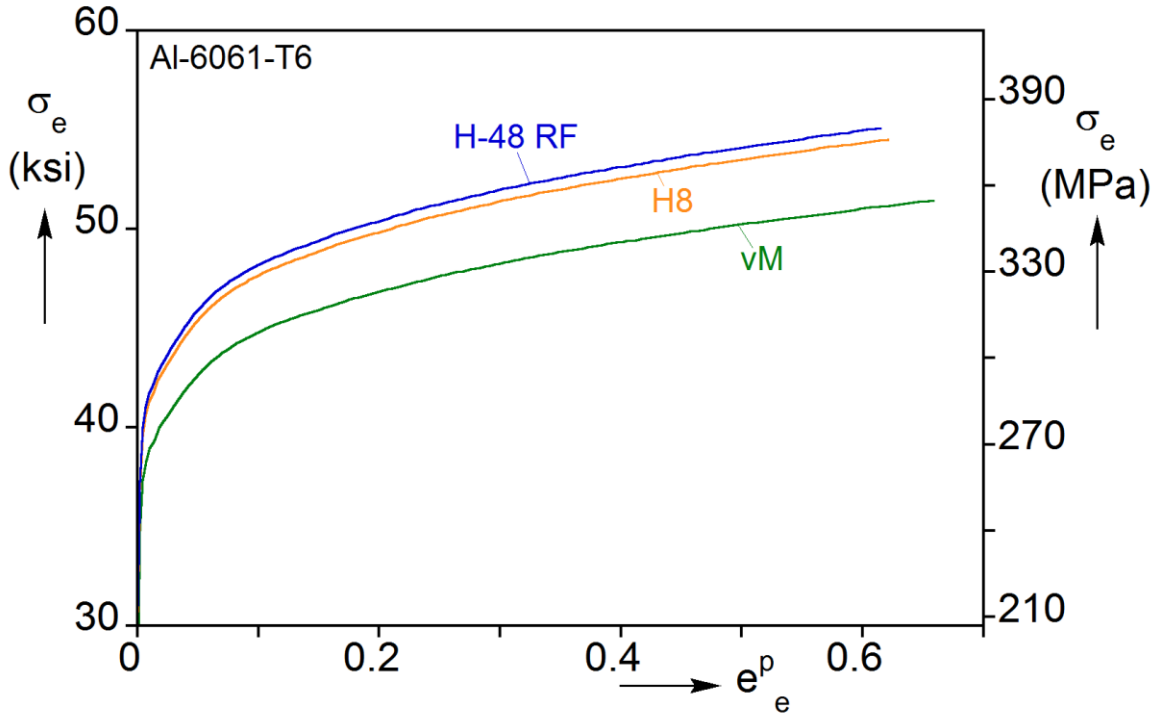

Fig. D.2 Comparison of the Reference Frame equivalent stress-equivalent plastic strain response with the von Mises and Hosford responses when the anisotropy is neglected.

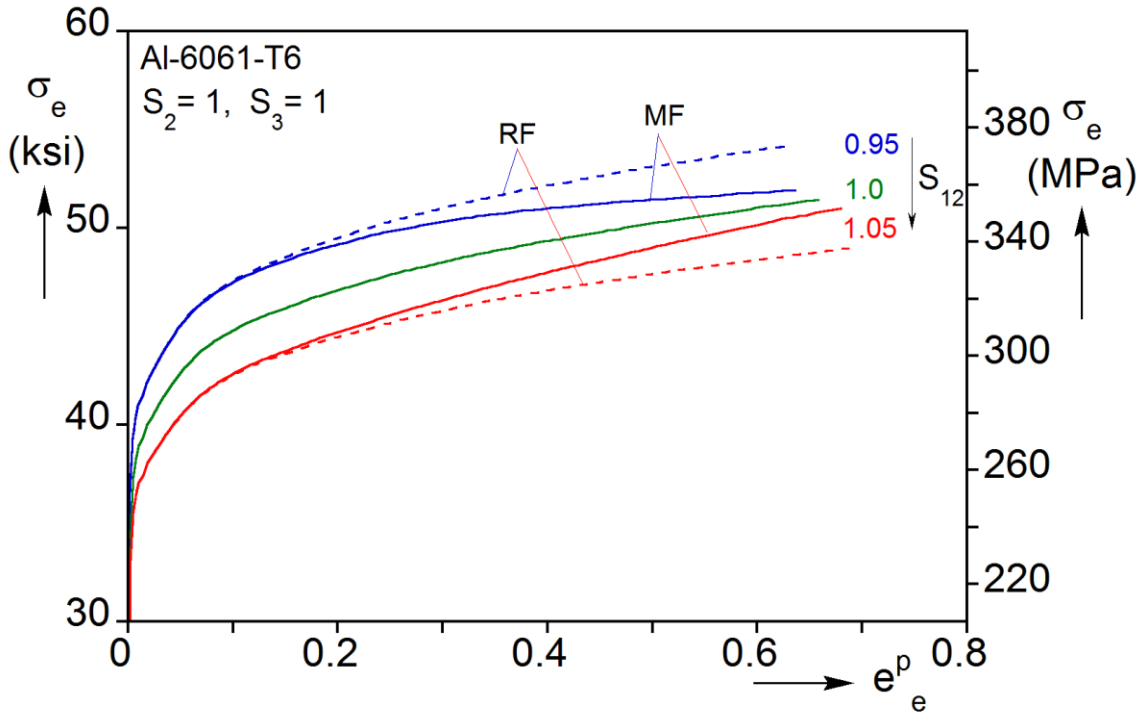

Fig. D.3a Effect of anisotropy constants on the Material and Reference Frame equivalent stress-equivalent plastic strain responses by varying S_{12}.

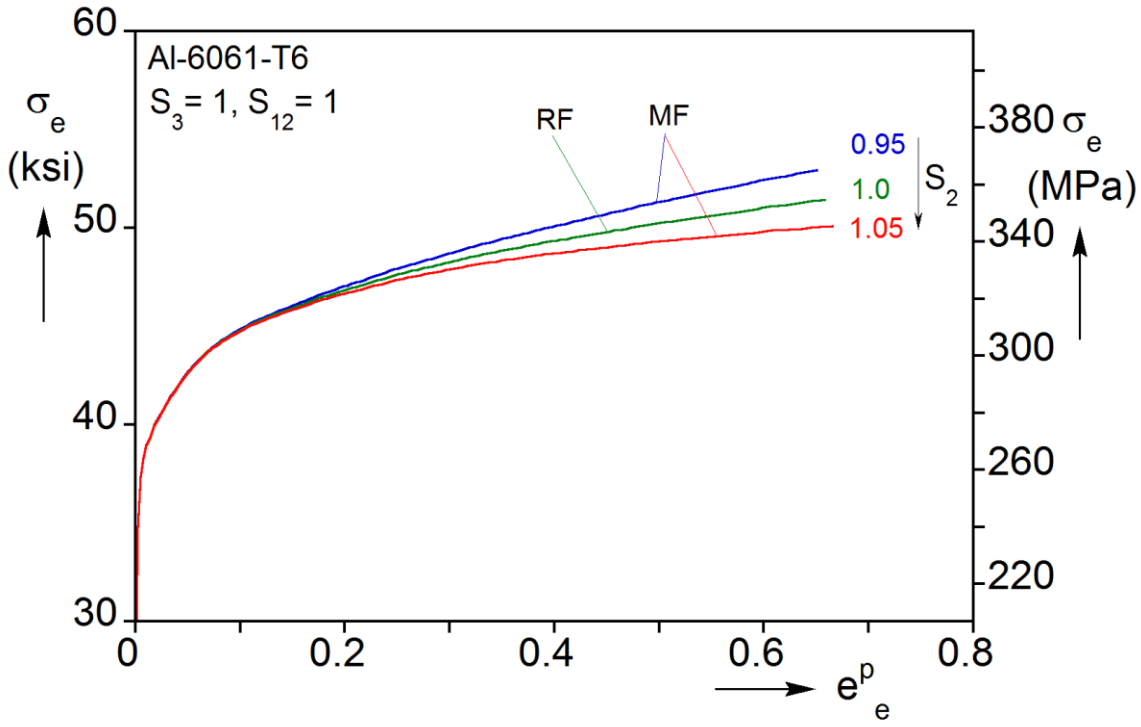

Fig. D.3b Effect of anisotropy constants on the Material and Reference Frame equivalent stress-equivalent plastic strain responses by varying S_2.

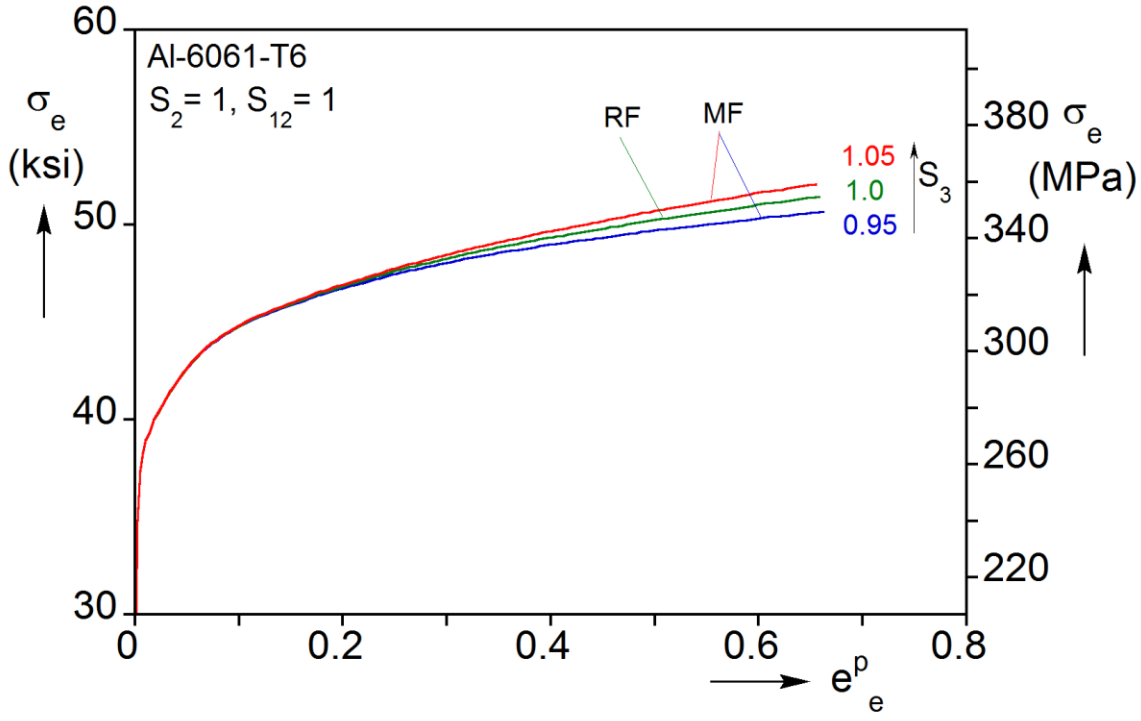

Fig. D.3c Effect of anisotropy constants on the Material and Reference Frame equivalent stress-equivalent plastic strain responses by varying S_3.

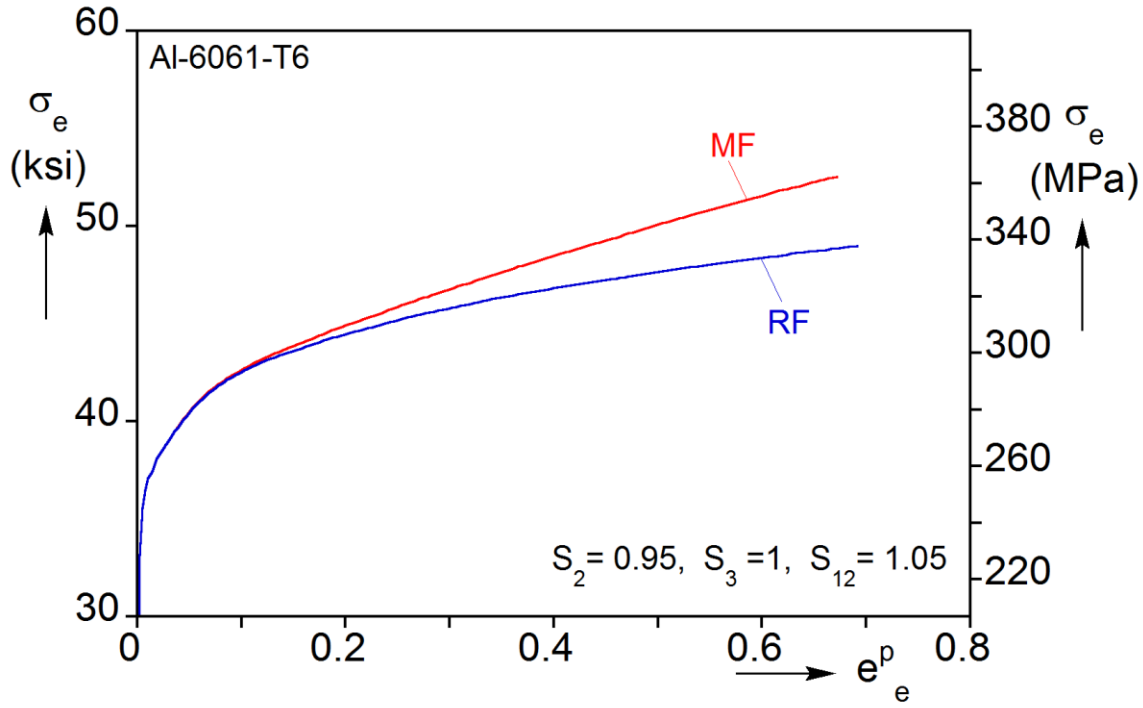

Fig. D.4a Effect of anisotropy constants on the Material and Reference Frame equivalent stress-equivalent plastic strain responses for $S_{12} > S_3 > S_2$.

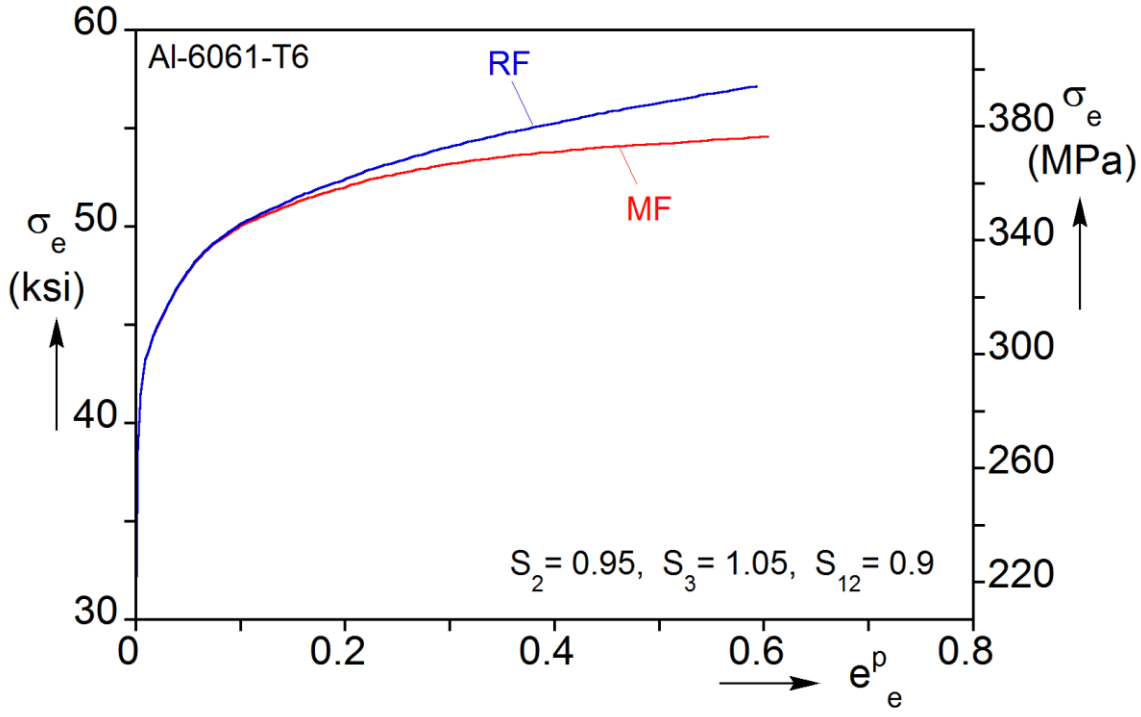

Fig. D.4b Effect of anisotropy constants on the Material and Reference Frame equivalent stress-equivalent plastic strain responses for $S_3 > S_2 > S_{12}$.

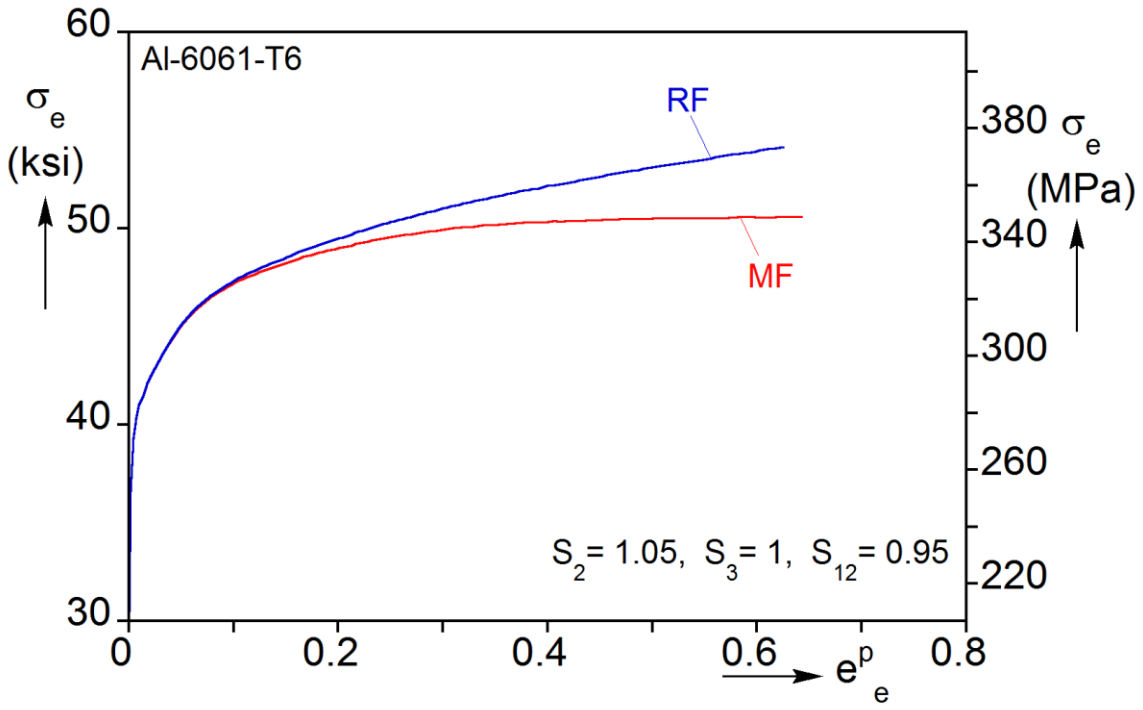

Fig. D.4c Effect of anisotropy constants on the Material and Reference Frame equivalent stress-equivalent plastic strain responses for $S_2 > S_3 > S_{12}$.

APPENDIX E: ONSET OF INSTABILITY UNDER COMBINED TENSION AND TORSION BASED ON H8 MODEL

In Section 5.2.1, the condition for the onset of instability under tension-torsion for any isotropic yield functions is derived. For H8 yield function, the more algebraically intensive derivation is given below.

From Eq. (5.5) the general condition for the onset of instability:

$$\left.\frac{d\sigma_e}{d\varepsilon_e}\right|_c = \sigma_e \left.\frac{\partial \Phi}{\partial \sigma_{22}}\right|_c \tag{E.1}$$

For 2D state of stress, the H8 yield function can be written as:

$$\Phi = \left(\frac{1}{2}((\sigma_1-\sigma_2)^8+\sigma_2^8+\sigma_1^8)\right)^{\frac{1}{8}} \tag{E.2}$$

where σ_1 and σ_2 are the *in-plane* principal stresses, which is related to the in-plane stress components as follows:

$$\sigma_1 = \frac{\sigma_{11}+\sigma_{22}}{2} + \sqrt{\left(\frac{\sigma_{11}-\sigma_{22}}{2}\right)^2+\sigma_{12}^2} \tag{E.3a}$$

$$\sigma_2 = \frac{\sigma_{11}+\sigma_{22}}{2} - \sqrt{\left(\frac{\sigma_{11}-\sigma_{22}}{2}\right)^2+\sigma_{12}^2} \tag{E.3b}$$

Let $\sigma_{11}=\beta\sigma_{22}, \sigma_{22}=\alpha\sigma_{12}$. The partial derivative of the principal stresses with respect to σ_{22} are:

$$\frac{\partial\sigma_1}{\partial\sigma_{22}} = \frac{1}{2} + \frac{1-\beta}{4\sqrt{\left(\frac{1-\beta}{2}\right)^2+\frac{1}{\alpha^2}}} \tag{E.4a}$$

$$\frac{\partial\sigma_2}{\partial\sigma_{22}} = \frac{1}{2} - \frac{1-\beta}{4\sqrt{\left(\frac{1-\beta}{2}\right)^2+\frac{1}{\alpha^2}}} \tag{E.4b}$$

Define $\sigma_2 = C\sigma_1$. Then

$$\frac{\partial \Phi}{\partial \sigma_1} = \frac{1}{2^{1/8}} \frac{1+(1-C)^7}{\left(1+C^8+(1-C)^8\right)^{7/8}} \tag{E.5a}$$

and

$$\frac{\partial \Phi}{\partial \sigma_2} = \frac{1}{2^{1/8}} \frac{1-(1-C)^7}{\left(1+C^8+(1-C)^8\right)^{7/8}} \tag{E.5b}$$

Finally, using chain rule:

$$\frac{\partial \Phi}{\partial \sigma_{22}} = \frac{\partial \Phi}{\partial \sigma_1}\frac{\partial \sigma_1}{\partial \sigma_{22}} + \frac{\partial \Phi}{\partial \sigma_2}\frac{\partial \sigma_2}{\partial \sigma_{22}} \tag{E.6a}$$

Substituting (E.4) and (E.5) into (E.6a), we have:

$$\frac{\partial \Phi}{\partial \sigma_{22}} = \frac{1}{2^{1/8}} \frac{1}{\left(1+C^8+(1-C)^8\right)^{7/8}} \left(1+2(1-C)^7 \frac{1-\beta}{4\sqrt{\left(\frac{1-\beta}{2}\right)^2+\frac{1}{\alpha^2}}} \right) \tag{E.6b}$$

For each radial path α, the corresponding hoop-axial stress ratio β can be obtained by requiring the hoop strain to be zero, i.e., $\frac{\partial \Phi}{\partial \sigma_{11}} = 0$. This condition implies:

$$2(1-C)^7 \frac{1-\beta}{4\sqrt{\left(\frac{1-\beta}{2}\right)^2+\frac{1}{\alpha^2}}} = 1 \tag{E.7}$$

For a given α, stress ratio β can be solved numerically for (E.7). Then, the equivalent strain at the onset of tension-torsion instability for H8 model can be evaluated from (E.1), using the hardening response for H8 extracted from the simple shear test as shown in Fig. 4.8b.

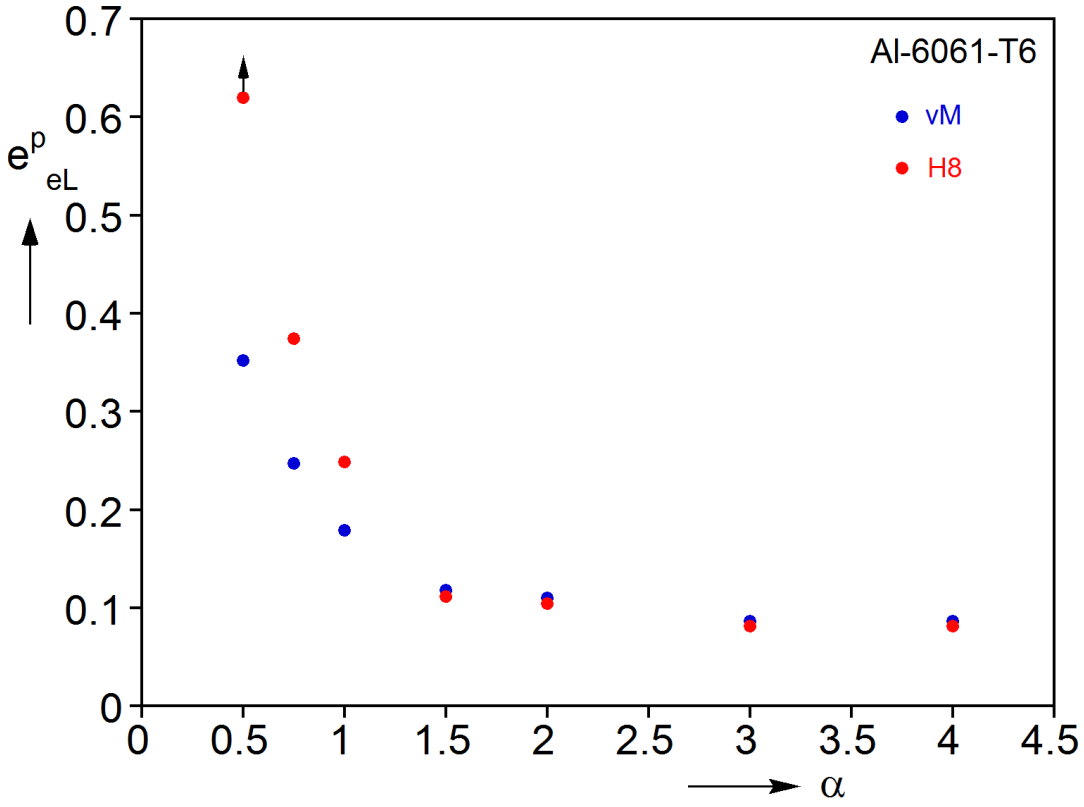

Fig. E.1 Comparison of the tension-torsion instability strains from Considère analysis based on von Mises and H8 models.

References

ABAQUS Theory Guide (2016), Section 1.4.3

ABAQUS (2010), User's Manual, version 6.10. Dassault Systèmes Simulia Corp., Providence, RI, USA.

Aretz, H., Keller, S. (2011). On the non-balanced biaxial stress state in bulge-testing. *Steel Research Int'l*, pp. 738-743., Special Edition.

ASTM B831 (2014). Standard test method for shear testing of thin Aluminum alloy products. *ASTM Int'l.*

Atkinson, M. (1997). Accurate determination of biaxial stress-strains relationships from hydraulic bulging tests of sheet metals. *Int'l. J. Mech. Sci*. 39, 761-769.

Banabic, D., Balan, T., Comsa, D.S., (2001). Closed-form solution for bulging through elliptical dies, *J. Mater. Proc. Tech.* **115**, 83-86.

Barlat, F., Brem, J. C., Yoon, J. W., Chung, K., Dick, R. E., Lege, D. J., Pourboghrat, F., Choi, S.-H., Chu, E. (2003). Plane stress yield function for aluminum alloy sheets—part 1: theory. *Int'l J. Plasticity* **19**, 1297-1319.

Barlat, F., Aretz, H., Yoon, J.W., Karabin, M.E., Brem, J.C., Dick, R.E. (2005). Linear transformation-based anisotropic yield functions. *Int'l J. Plasticity* **21**, 1009-1039.

Bai, Y., Wierzbicki, T. (2008). A new model of metal plasticity and fracture with pressure and Lode dependence. *Int'l J. Plasticity* **24**, 1071-1096.

Bai, Y., Wierzbicki, T. (2010). Application of extended Mohr-Coulomb criterion to ductile fracture. *Int'l J. Fract.* **161**, 1-20

Bao, Y., Wierzbicki, T. (2004). On fracture locus in the equivalent strain and stress triaxiality space. *Int'l J. Mech. Sci.* **46**, 81-98.

Barsoum, I., Faleskog, J. (2007a). Rupture mechanisms in combined tension and shear–Experiments. *Int'l J. Solids Struct.* **44**, 1768-1786.

Barsoum, I., Faleskog, J. (2007b). Rupture mechanisms in combined tension and shear–Micromechanics. *Int'l J. Solids Struct.* **44**, 5481-5498.

Beese, A. M., Luo, M., Li, Y., Bai, Y., Wierzbicki, T. (2010). Partially coupled anisotropic fracture model for aluminum sheets. *Eng. Fract. Mech.* **77**, 1128-1152.

Benedyk, J. C. (2010). Aluminum alloys for lightweight automotive structures. In Materials, design and manufacturing for lightweight vehicles, 79-113, Woodhead Publishing.

Benzerga, A. A., Besson, J. (2001). Plastic potentials for anisotropic porous solids. *Eur. J. Mech. A/Solids* **20**, 397-434.

Benzerga, A. A., Leblond, J. B. (2010). Ductile fracture by void growth to coalescence. *Adv. Appl. Mech.* **44**, 169-305.

Bramley, A.N., Mellor, P.B. (1966). Plastic flow in stabilized sheet steel. *Int'l J. Mech. Sci.* **8**, 101-114.

Bridgman, P.W. (1944). The stress distribution at the neck of a tension specimen. *Trans. Am. Soc. Met.* **32**, 553–574.

Bridgman, P. W. (1947). The effect of hydrostatic pressure on the fracture of brittle substances. *J. Appl. Phys*. **18**, 246-258.

Bridgman, P. W. (1952). Studies in Large Plastic Flow and Fracture with Special Emphasis on the Effects of Hydrostatic Pressure, McGraw-Hill, New York.

Brünig, M., Chyra, O., Albrecht, D., Driemeier, L., Alves, M. (2008). A ductile damage criterion at various stress triaxialities. *Int'l J. Plasticity* **24**, 1731-1755.

Chakrabarty, J., Alexander, J.M. (1970). Hydrostatic bulging of circular diaphragms. *J. Strain Anal. Eng.* **5**, 155-161.

Chen, K., Kyriakides, S., Scales, M. (2018b). Effect of material frame rotation on the hardening of an anisotropic material in simple shear tests. *ASME J. Applied Mech.* **85**, 124501: 1-5.

Chen, K., Scales, M., Kyriakides, S. (2018a). Material hardening of a high ductility aluminum alloy from a bulge test. *Int'l J. Mech. Sci.* **138-139**, 476-488.

Chen, K**.,** Scales, M., Kyriakides, S. (2019). Material response, localization and failure of an Aluminum alloy under combined shear and tension: Part II Analysis. *Int'l J. Plasticity* **120**, 361-379.

Chen, K., Scales, M., Kyriakides, S., Corona, E. (2016). Effects of anisotropy on material hardening and burst in the bulge test. *Int'l J. Solids Struct.* **82**, 70-84.

Chu, C.C., Needleman, A., (1980). Void nucleation effects in biaxially stretched sheets. *J. Eng. Mater. Technol. ASME* **102**, 249–256.

Cole, G. S., Sherman, A. M. (1995). Light weight materials for automotive applications. *Materials characterization* **35**, 3-9.

Dick, R. E., Yoon, J. W. (2018). Plastic anisotropy and failure in thin metal: Material characterization and fracture prediction with an advanced constitutive model and polar EPS (effective plastic strain) fracture diagram for AA 3014-H19. *Int'l J. Solids Struct.* **151**, 195-213.

DIN EN ISO 16808:2014(E) (2014). Metallic materials–sheet and strip– Determination of the biaxial stress-strain curve by means of a bulge test with optical measuring systems.

Dunand, M., Maertens, A. P., Luo, M., Mohr, D. (2012). Experiments and modeling of anisotropic aluminum extrusions under multi-axial loading–Part I: Plasticity. *Int'l J. Plasticity* **36**, 34-49.

Dunand, M., Mohr, D. (2010). Hybrid experimental-numerical analysis of basic ductile fracture experiments for sheet metals. *Int'l J. Solids Struct.* **47**, 1130-1143.

Dunand, M., Mohr, D. (2011). Optimized butterfly specimen for the fracture testing of sheet materials under combined normal and shear loading. *Eng. Fract. Mech.* **78**, 2919-2934.

Dziallach, S., Bleck, W., Blumbach, M., Hallfeldt, T. (2007). Sheet metal testing and flow curve determination under multiaxial conditions. *Adv. Eng. Mater.* **9**, 987-994.

Faleskog, J., Barsoum, I. (2013). Tension-torsion fracture experiments-Part I: Experiments and a procedure to evaluate the equivalent plastic strain. *Int'l J. Solids Struct.* **50**, 4241-4257.

Friebe, H., Klein, M., Heinle, I., Lipp, A. (2013). Optimized yield curve determination using bulge test combined with optical measurement and material thickness compensation. *Key Eng. Mat.* **549**, 389-396.

Gao, X., Zhang, T., Hayden, M., Roe, C. (2009). Effects of the stress state on plasticity and ductile failure of an aluminum 5083 alloy. *Int'l J. Plasticity* **25**, 2366-2382.

Ghahremaninezhad, A., Ravi-Chandar, K. (2012). Ductile failure behavior of polycrystalline Al 6061-T6. *Int'l J. Fract.* **174**, 177-202.

Ghahremaninezhad, A., Ravi-Chandar, K. (2013). Ductile behavior in polycrystalline aluminum alloy Al 6061-T6 under shear dominant loading. *Int'l J. Fract.* **180**, 23-39.

Giagmouris, T., Kyriakides, S., Korkolis, Y.P., Lee, L.-H. (2010). On the localization and failure in aluminum shells due to crushing induced bending and tension. *Int'l J. Solids Struct.* **47**, 2680-2692.

Gleyzal, A. (1948). Plastic deformation of a circular diaphragm under pressure. *Transactions of the ASME* **70**, 288-296.

Gologanu, M., Leblond, J. B., Perrin, G., Devaux, J. (2001). Theoretical models for void coalescence in porous ductile solids. I. Coalescence "in layers". *Int'l J. Solids Struct*. **38**, 5581-5594.

Gorji, M. B., Mohr, D. (2018). Predicting shear fracture of aluminum 6016-T4 during deep drawing: Combining Yld-2000 plasticity with Hosford–Coulomb fracture model. *Int'l J. Mech. Sci.* **137**, 105-120.

Graham, S. M., Zhang, T., Gao, X., Hayden, M. (2012). Development of a combined tension–torsion experiment for calibration of ductile fracture models under conditions of low triaxiality. *Int'l J. Mech. Sci.* **54**, 172-181.

Gross, A. J., Ravi-Chandar, K. (2014). Prediction of ductile failure using a local strain-to-failure criterion. *Int'l J. Fract.* **186**, 69-91.

Gross, A. J., Ravi-Chandar, K. (2015). On the extraction of elastic–plastic constitutive properties from three-dimensional deformation measurements. *ASME J. Applied Mech.* **82**, 071013.

Gurson, A.L. (1977). Continuum theory of ductile rupture by void nucleation and growth: Part I– Yield criteria and flow rules for porous ductile media. *J. Eng. Mat. Tech.* **99**, 2–15.

Gutscher, G., Wu, H. C., Ngaile, G., Altan, T. (2004). Determination of flow stress for sheet metal forming using the viscous pressure bulge (VPB) test. *J. Mater. Proc. Techn.* **146**, 1-7.

Ha, J., Baral, M., Korkolis, Y. P. (2018). Plastic anisotropy and ductile fracture of bake-hardened AA6013 aluminum sheet. *Int'l J. Solids Struct.* **155**, 123-139.

Haltom, S.S., Kyriakides, S., Ravi-Chandar, K. (2013). Ductile failure under combined shear and tension. *Int'l J. Solids Struct.* **50,** 1507-1522.

Hancock, J.W., McKenzie, A.C., (1976). On the mechanisms of ductile failure in high-strength steels subjected to multi-axial stress-states. *J. Mech. Phys. Solids* **24**, 147-169.

Hill, R. (1950). A theory of plastic bulging of a metal diaphragm by lateral pressure. *Philos. Mag.* **7**, 1133-1142.

Hill, R. (1950). The Mathematical Theory of Plasticity, Clarendon Press, Oxford.

Hosford, W.F. (1972). A generalized isotropic yield criterion. *ASME J. Applied Mech.* **39**, 607-609.

Johnson, G.R., Cook, W.H. (1985). Fracture characteristics of three metals subjected to various strains, strain rates, temperatures and pressures. *Eng. Fract. Mech.* **21**, 31-48.

Kang, J., Wilkinson, D. S., Wu, P. D., Bruhis, M., Jain, M., Embury, J. D., Mishra, R. K. (2008). Constitutive behavior of AA5754 sheet materials at large strains. *J. Eng. Mat. Techn.* **130**, 031004:1-5.

Khan, A. S., Liu, H. (2012). A new approach for ductile fracture prediction on Al 2024-T351 alloy. *Int'l J. Plasticity* **35**, 1-12.

Koç, M., Billur, E., Cora, O.N. (2011). An experimental study on the comparative assessment of hydraulic bulge test analysis methods. *Mater. Design* **32**, 272-281.

Kohar, C. P., Brahme, A., Imbert, J., Mishra, R. K., Inal, K. (2017). Effects of coupling anisotropic yield functions with the optimization process of extruded aluminum front rail geometries in crashworthiness. *Int'l J. Solids Struct*. **128**, 174-198.

Korkolis, Y.P., Kyriakides, S. (2008a). Inflation and burst of anisotropic tubes for hydroforming applications. *Int'l J. Plasticity* **24**, 509-543.

Korkolis, Y.P., Kyriakides, S. (2008b). Inflation and burst of aluminum tubes part II: An advanced yield function including deformation-induced anisotropy. *Int'l J. Plasticity* **24**, 1625-1637.

Korkolis, Y.P., Kyriakides, S. (2009). Path-dependent failure of inflated aluminum tubes. *Int'l J. Plasticity* **25**, 2059-2080.

Korkolis, Y.P., Kyriakides, S., Giagmouris, T., Lee, L.-H. (2010). Constitutive modeling and rupture predictions of Al-6061-T6 tubes under biaxial loading paths. *ASME J. Applied Mech.* **77**:5, 064501, 1-5.

Lăzărescu, L., Comsa, D. S., Nicodim, I., Ciobanu, I., Banabic, D. (2012). Characterization of plastic behaviour of sheet metals by hydraulic bulge test. *Transactions of Nonferrous Metals Society of China* **22**, 275-279.

Lăzărescu, L., Nicodim, I., Ciobanu, I., Comșa, D. S., Banabic, D. (2013). Determination of material parameters of sheet metals using the hydraulic bulge test. *Acta Metallurgica Slovaca* **19,** 4-12.

Lee, J.-Y., Lee, K.J, Kuwabara, T., Barlat, F. (2018). Numerical modeling for accurate prediction of strain localization in hole expansion of a steel sheet. *Int'l J. Solids Struct.* **156-157**, 107-118.

Lemoine, X., Iancu, A., Ferron, G. (2011). Flow curve determination at large plastic strain levels: Limitations of the membrane theory in the analysis of the hydraulic bulge test. *Proc. 14th ESAFORM Conf. on Material Forming*, Belfast, UK, pp. 1411-1416.

Lemaitre, J. (1985). A continuous damage mechanics model for ductile fracture. *J. Eng. Mat. Tech.* **107**, 83-89.

Lemaitre, J., Chaboche, J. L. (1994). Mechanics of solid mechanics. Cambridge University Press.

Lewandowski, J. J., Lowhaphandu, P. (1998). Effects of hydrostatic pressure on mechanical behaviour and deformation processing of materials. *Int'l Mater. Rev.* **43**, 145-187.

Lode, W. (1926). Versuche über den Einfuss der mittleren Hauptspannung auf das Fliessen der Metalle Eisen Kupfer und Nickel. *Zeitung Phys*. **36**, 913–939.

Logan, R.W. and Hosford, W.F., 1980. Upper-bound anisotropic yield locus calculations assuming <111>-pencil glide. *Int'l J. Mech. Sci.* **22**, 419-430.

Lou, Y., Chen, L., Clausmeyer, T., Tekkaya, A. E., Yoon, J. W. (2017). Modeling of ductile fracture from shear to balanced biaxial tension for sheet metals. *Int'l J. Solids Struct*. **112**, 169-184.

Lou, Y., Huh, H., Lim, S., Pack, K. (2012). New ductile fracture criterion for prediction of fracture forming limit diagrams of sheet metals. *Int'l J. Solids Struct*. **49**, 3605-3615.

Lou, Y., Yoon, J. W. (2017). Anisotropic ductile fracture criterion based on linear transformation. *Int'l J. Plasticity* **93**, 3-25.

Lou, Y., Yoon, J. W. (2018). Anisotropic yield function based on stress invariants for BCC and FCC metals and its extension to ductile fracture criterion. *Int'l J. Plasticity* **101**, 125-155.

Lou, Y., Yoon, J. W. (2019). Alternative approach to model ductile fracture by incorporating anisotropic yield function. *Int'l J. Solids Struct*. **164**, 12-24.

Lou, Y., Yoon, J. W., Huh, H. (2014). Modeling of shear ductile fracture considering a changeable cut-off value for stress triaxiality. *Int'l J. Plasticity* **54**, 56-80.

Luo, M., Dunand, M., Mohr, D. (2012). Experiments and modeling of anisotropic aluminum extrusions under multi-axial loading: Part II Ductile fracture. *Int'l J. Plasticity* **32**, 36-58.

Marandi, F. A., Jabbari, A. H., Sedighi, M., Hashemi, R. (2017). An Experimental, analytical, and numerical investigation of hydraulic bulge test in two-layer Al–Cu Sheets. *ASME J. Manuf. Sci. Eng.* **139**, 031005.

McClintock, F.A., (1968). A criterion for ductile fracture by the growth of holes. *ASME J. Applied Mech.* **35**, 363-371.

Mellor, P. B. (1956). Stretch forming under fluid pressure. *J. Mech. Phys. Solids* **5**, 41-56.

Miyauchi, K., (1984). A proposal of a planar simple shear test in sheet metals. *Sci. Papers Institute Physical Chem. Research* (of Japan) **87**, pp. 27-40.

Mohamed, M. S., Foster, A. D., Lin, J., Balint, D. S., Dean, T. A. (2012). Investigation of deformation and failure features in hot stamping of AA6082: Experimentation and modelling. *Int'l J. of Mach. Tool. Manu.* **53**, 27-38.

Mohr, D., Henn, S. (2007). Calibration of stress-triaxiality dependent crack formation criteria: a new hybrid experimental–numerical method. *Exp. Mech.* **47**, 805-820.

Mohr, D., Marcadet, S.J. (2015). Micromechanically-motivated phenomenological Hosford–Coulomb model for predicting ductile fracture initiation at low stress triaxialities. *Int'l J. Solids Struct.* **67**, 40-55.

Mulder, J., Vegter, H., Aretz, H., Keller, S., van den Boogaard, A.H. (2015). Accurate determination of flow curves using the bulge test with optical measuring systems. *J. Mater. Proc. Techn.* **226**, 169-187

Nahshon, K., Hutchinson, J.W. (2008). Modification of the Gurson model for shear failure. *Eur. J. Mech. A/Solids* **27**, 1-17.

Needleman, A. (1987). A continuum model for void nucleation by inclusion debonding. *ASME J. Applied Mech.* **54**, 525-531.

Pack, K., Tancogne-Dejean, T., Gorji, M. B., Mohr, D. (2018). Hosford-Coulomb ductile failure model for shell elements: Experimental identification and validation for DP980 steel and aluminum 6016-T4. *Int'l J. Solids Struct*. **151**, 214-232.

Papasidero, J., Doquet, V., Mohr, D. (2014). Determination of the effect of stress state on the onset of ductile fracture through tension-torsion experiments. *Exp. Mech.* **54,** 137-151.

Papasidero, J., Doquet, V., Mohr, D. (2015). Ductile fracture of aluminum 2014-T351 under proportional and non-proportional multi-axial loading: Bao-Wierzbicki results revisited. *Int'l J. Solids Struct.* **69-70**, 459-474.

Pardoen, T., Hutchinson, J. W. (2000). An extended model for void growth and coalescence. *J. Mech. Phys. Solids*, **48**, 2467-2512.

Rana, R., Singh, S.B., Bleck, W., Mohanty, O.N. (2010). Biaxial stretching behavior of a copper-alloyed interstitial-free steel by bulge test. *Metall. Mater. Trans. A* **41**, 1483-1492.

Ranta-Eskola, A.J. (1979). Use of the hydraulic bulge test in biaxial tensile testing. *Int'l J. Mech. Sci.* **21**, 457-465.

Rees, D. W. A. (1995). Plastic flow in the elliptical bulge test. *Int'l J. Mech. Sci.* **37**, 373-389

Reis, L.C., Parates, P.A., Oliveira, M.C., Santos, A.D., Fernandes, J.V. (2017). Anisotropy and plastic flow in a circular bulge test. *Int'l J. Mech. Sci.* **128-129**, 70-93

Rice, J.R., Tracey, D.M. (1969). On the ductile enlargement of voids in triaxial stress fields. *J. Mech. Phys. Solids* **17**, 201-217.

Saito M. (2001). Development of aluminum bodies for fuel efficient vehicles. *Materials Today* **4**, 30-34.

Santos, A.D., Teixeira, P., Barata da Rocha, A., Barlat, F. (2010). On the determination of flow stress using bulge test and mechanical measurements. *Proc. 10th Int'l Conf. NUMIFORM 2010*, June 13-17, Pohang, Korea, pp. 845-852.

Scales, M. (2019) Localization and failure of Aluminum 6061-T6 under biaxial loading (Doctoral Dissertation). The University of Texas at Austin.

Scales, M., Chen, K., Kyriakides, S. (2019). Material response, localization, and failure of an Aluminum alloy under combined shear and tension: Part I Experiments. *Int'l J. Plasticity* **120**, 340-360.

Scales, M., Tardif, N., Kyriakides, S. (2016). Ductile failure of aluminum alloy tubes under combined torsion and tension. *Int'l J. Solids Struct*. **97–98**, 116–128.

Swift, H. W. (1952). Plastic instability under plane stress. *J. Mech. Phys. Solids* **1**, 1-18.

Tardif, N., Kyriakides, S. (2012). Determination of anisotropy and material hardening for aluminum sheet metal. *Int'l J. Solids Struct.* **49**, 3496-3506.

Tian, H., Brownell, B., Baral, M., Korkolis, Y. P. (2017). Earing in cup-drawing of anisotropic Al-6022-T4 sheets. *Int'l J. Mater. Form.* **10**, 329-343.

Tvergaard, V. (1990). Material failure by void growth to coalescence. *Adv. Appl. Mech.* **27**, 83-151.

Tvergaard, V. (1998). Interaction of very small voids with larger voids. *Int'l J. Solids Struct*. **35**, 3989-4000.

Tvergaard, V., Needleman, A. (1984). Analysis of the cup-cone fracture in a round tensile bar. *Acta Metall.* **32**, 157–169.

Voce, E. (1948). The relationship between stress and strain for homogeneous deformation. *J. Inst. Met.* **74**, 537–562.

Vucetic, M., Bouguecha, A., Peshekhodov, I., Gotze, T., Huinink, T., Friebe, H., Moller, T., Behrens, B.-A. (2011). Numerical validation of analytical biaxial true stress-true strain curves from the bulge test. *Proc. 8th Int'l Conf. NUMISHEET 2011*, August 21-26, Seoul, Korea, 107-114.

Xue, L. (2007). Damage accumulation and fracture initiation in uncracked ductile solids subject to triaxial loading. *Int'l J. Solids Struct*. **44**, 5163-5181.

Xue, Z., Faleskog, J., Hutchinson, J.W. (2013). Tension-torsion fracture experiments-Part II: Simulation with the extended Gurson model and a ductile fracture criterion based on plastic strain. *Int'l J. Solids Struct.* **50**, 4258-4269.

Yanaga, D., Kuwabara, T., Uema, N., Asano, M. (2012). Material modeling of 6000 series aluminum alloy sheets with different density cube textures and effect on the accuracy of finite element simulation. *Int'l J. Solids Struct.* **49**, 3488-3495.

Yin, Q., Zillmann, B., Suttner, S., Gerstein, G., Biasutti, M., Tekkaya, A. E., Wagner, M. F. X., Merklein, M., Schaper, M., Halle, T., Brosius, A. (2014). An experimental and numerical investigation of different shear test configurations for sheet metal characterization, *Int'l J. Solids Struct.* **51**, 1066-1074.

Yoon, J.W., Barlat, F., Dick, R.E., Karabin, M.E. (2006). Prediction of six or eight ears in a drawn cup based on a new anisotropic yield function. *Int'l J. Plasticity* **22**, 174-193.

Yoon, J.W. (2009, 2011). Personal communications.

Young, R.F., Bird, J.E., Duncan, J.L. (1981). An automated hydraulic bulge tester. *J. Appl. Metal Working* **2**, 11-18.

Yousif, M.I., Duncan, J.L., Johnson, W. (1970). Plastic deformation and failure of thin elliptical diaphragms. *Int'l J. Mech. Sci.* **12**, 959-972.

Vita

Kelin Chen obtained his Bachelor's degree in Engineering Mechanics from Sichuan University in 2009 with top rank in his major. He then entered Tsinghua University and earned his Master's degree in Engineering Mechanics in 2012. In August 2012, he entered the Graduate School at The University of Texas at Austin to pursue a Ph.D. degree in Engineering Mechanics.

Permanent email: kelinchen@utexas.edu

This dissertation was typed by the author.